

DOTTORATO DI RICERCA  
IN FISICA

Ciclo XXI

Settore scientifico di afferenza: FIS03

**Low-dimensional carbon allotropes:  
an electron microscopy investigation.**

Presentata da Luca Ortolani

Coordinatore Dottorato:  
**Fabio Ortolani**

Relatori:  
**Prof. Giuseppe Morandi**  
**Dott. Giorgio Lulli**

Correlatore:  
**Dott. Marc Monthieux**



# Contents

<b>Introduction</b>	<b>vii</b>
<b>1 Low-dimensional carbon allotropes</b>	<b>1</b>
1.1 It's all about carbon . . . . .	2
1.1.1 Carbon atoms . . . . .	3
1.1.2 $sp$ hybridization . . . . .	4
1.1.3 $sp^2$ hybridization . . . . .	5
1.1.4 $sp^3$ hybridization . . . . .	5
1.2 Graphene . . . . .	6
1.2.1 Atomic structure . . . . .	8
1.2.2 Electronic structure and potential applications . . . . .	13
1.2.3 Synthesis of graphene sheets . . . . .	17
1.3 Single Wall Carbon Nanotubes . . . . .	21
1.3.1 Atomic structure . . . . .	22
1.3.2 Electronic structure . . . . .	23
1.3.3 Engineering the properties of SWCNTs . . . . .	26
<b>2 TEM characterization of graphene and SWCNTs</b>	<b>29</b>
2.1 Transmission Electron Microscopy . . . . .	30
2.1.1 Looking into the <i>nanoworld</i> . . . . .	30
2.1.2 TEM imaging . . . . .	33
2.2 Electron Diffraction from honeycomb lattices . . . . .	37
2.2.1 Basic electron diffraction . . . . .	37
2.2.2 Diffraction from plain honeycomb lattice . . . . .	40
2.2.3 Diffraction from rolled honeycomb lattice . . . . .	48
2.3 High-Resolution TEM of graphene membranes and SWCNT . . . . .	51
2.3.1 High-resolution TEM principles . . . . .	51

---

2.3.2	Electron beam damage . . . . .	58
2.3.3	Low-voltage aberration corrected HREM experimental investigation . . . . .	60
2.4	Conclusions . . . . .	67
<b>3</b>	<b>Electron holography of graphene membranes and SWCNTs</b>	<b>69</b>
3.1	Electron holography . . . . .	71
3.1.1	Electron waves and the missing phase . . . . .	71
3.1.2	Acquisition and reconstruction of electron holograms in the TEM . . . . .	76
3.1.3	Phase and nanoscopic electromagnetic fields . . . . .	80
3.2	Experimental results . . . . .	81
3.2.1	Holography of carbon-based materials . . . . .	81
3.2.2	Electron holography of SWCNTs . . . . .	83
3.2.3	Electron holography of graphene membranes . . . . .	87
3.3	Discussion . . . . .	92
3.3.1	Mean electrostatic potential of graphene lattices . . . . .	92
3.3.2	Curvature induced electric dipole effect in CNT . . . . .	94
3.3.3	The effect of valence charges distribution on the phase shift	96
<b>4</b>	<b>3D Reconstruction at the Nanoscale</b>	<b>99</b>
4.1	Introduction . . . . .	100
4.2	Mapping geometric distortions . . . . .	101
4.2.1	Mapping 3D waviness of 2D membranes . . . . .	101
4.2.2	Geometric phase analysis of HREM images . . . . .	103
4.3	Experimental results . . . . .	107
4.3.1	Experimental set-up and sample preparation . . . . .	107
4.3.2	HREM imaging . . . . .	107
4.3.3	GPA deformation reconstruction . . . . .	112
4.4	3D reconstruction . . . . .	117
4.4.1	Modeling deformations . . . . .	117
4.4.2	Structure simulation . . . . .	119
4.4.3	Discussion of the results . . . . .	121
<b>5</b>	<b>Graphene membranes as nanoscopic tangential sieves</b>	<b>125</b>
5.1	Alignment of SWCNT over FLG . . . . .	127
5.1.1	Samples preparation . . . . .	127
5.1.2	Electron diffraction investigation . . . . .	130

---

5.1.3	HREM imaging . . . . .	134
5.2	FGCs acting as tangential nano-sieves for SWCNTs . . . . .	138
5.2.1	Nanoscopic tangential sieves . . . . .	138
5.2.2	Graphene nano-tribology . . . . .	138
	<b>Conclusions</b>	<b>143</b>
	<b>Bibliography</b>	<b>145</b>
	<b>List of publications</b>	<b>153</b>



Names and attributes must be accommodated to the essence of things, and not the essence to the names, since things come first and names afterwards.

*(Galileo Galilei)*

I dedicate this manuscript to you, Giorgio. Hey, did you see? In the end I made it! Thanks to you. I know you always believed it of me, even before I did. I did my best. The result would surely deserve your reproaches and I really yearn for them.

*In memory of Pier Giorgio Merli  
December 23, 1942 - February 23, 2008*

# **Introduction**

Carbon offers the extraordinary opportunity to investigate a material in all possible dimensions. Indeed it can form 0-dimensional structures like fullerenes, *1-dimensional* carbon nanotubes (CNTs) and carbynes, *2-dimensional* graphene sheets and finally *3-dimensional* graphite and diamond. In the age of nanotechnology, carbon can thus be seen as an “old but new” material.

Among low-dimensional carbon allotropes, the experimental evidence of graphene (a single monoatomic layer of graphite), and of Few Graphenes Crystal (FGC) (a pile of few stacked graphenes), in 2004 has opened up a completely new research field on two-dimensional crystals, whose existence was for long time doubted [1, 2]. Graphene can be considered as the *mother* of all other carbon based nanostructures, like fullerenes and CNTs, as all these can be seen as curved and rolled-up pieces of a graphene sheet. For this reason, even if it can be considered a really *new material*, nonetheless, researchers did not suffer from a *cold start*, as they exploited the large experience acquired with two decades of intensive study on the *kins* of this material: the carbon nanotubes [3–5].

Graphene, and FGCs, gathered the interests of a large part of the scientific community; in particular, their exceptional electronic properties suggest that graphene might be the key-material in the next-generation of high-performance electronic devices [6]. Nevertheless, many issues need to be addressed to demonstrate the feasibility of a "graphene-based technology".

The production of graphene is one of the most challenging issues for the actual exploitation of this material. FGC were discovered using conventional optical microscopy, among the millions of micron-sized debris left on a SiO<sub>2</sub> substrate after mechanical exfoliation of graphite by standard scotch tape[1, 7]. Since graphene discovery, this "*scotch tape method*" remains the most effective way to produce high quality several micron large graphene single layers crystals, which are successively integrated in the final device. A different approach is the controlled growth of graphene crystals in the desired configuration, over the final integrated device.

The crystal and electronic structure of graphene were extensively studied, from a theoretical point of view, already few decades before graphene was discovered [8–10]. The atomic structure of this lattice determines its unique electronic properties. In fact, due to the hexagonal symmetry in the lattice the energy dispersion relationship for carriers in graphene is linear in the momentum, close to the points where valence and conduction bands touch [8–10]. This is at the origin of the extraordinary electronic properties of this material, as, for example, carrier mobility, two orders

of magnitude higher than in silicon [11, 12].

When the lateral dimension of the crystal is reduced down to the nanometer scale, the crystallographic orientation of the edges determines the electronic properties of the resulting graphene nano-ribbon, deciding whether it will be metallic or semiconducting [13]. However, graphene crystals are not expected to be perfectly flat sheets, instead they should present continuous surface undulations [14, 15]. This waviness is expected to locally modulate its electronic and magnetic properties, affecting charge transport [16–18]. For these reasons, a structural characterization, down to the atomic level, is mandatory.

The research reported in this manuscript concerns the structural characterization of FGC membranes and single-walled CNTs (SWCNTs). The experimental investigation has been performed using a wide range of transmission electron microscopy (TEM) techniques, from conventional imaging and diffraction, to advanced interferometric methods, like electron holography and Geometric Phase Analysis (GPA). The structural and electronic properties of graphene and SWCNTs are similar. While graphene is a relatively new material, SWCNTs rely on almost 20 year of extensive research on their structural and physical properties. In this scenario SWCNTs are the perfect workbench to tune the experimental methodology required for the characterization of FGCs.

Chapter 1 is a general introduction to FGCs and SWCNTs, to their structural and physical properties, and to the methods used to prepare the experimental samples investigated in this work.

Chapter 2 presents the results of the morphological and atomic-scale structural investigation, performed on FGCs and SWCNTs, using standard TEM electron diffraction techniques and state-of-the-art aberrations-corrected high-resolution TEM (HREM), with a low-voltage optical set-up, to reduce beam damage in the samples.

Chap. 3 shows the results of the holographic characterization of FGCs and SWCNTs. The local lattice charge distribution has been probed, achieving the measure of the mean electrostatic potential of an individual graphene layer. The comparative study of planar graphene lattice and SWCNTs, allows to measure the valence-charge redistribution, induced by the curvature of SWCNTs.

Chap. 4 presents a novel method for the three-dimensional reconstruction of FGCs waviness using HREM images. Differently from other approaches, such as electron tomography, the proposed method requires to process a single HREM micrograph of a crystal flake. The geometrical distortions in the image are mapped

using GPA, and used to recover 3D information.

The last Chapter reports the investigation of the adhesion of SWCNTs over graphene surface. The combined methods of electron diffraction and aberrations-corrected HREM imaging shows that graphene membranes act as tangential nano-sieves, grafting preferentially achiral tubes to their surface. This effect can be exploited to solve the important technological issue of selecting SWCNTs chirality.

# **LOW-DIMENSIONAL CARBON ALLOTROPES**

All truths are easy to understand  
once they are discovered; the point  
is to discover them.

*(Galileo Galilei)*

## Introduction

Carbon is known from mankind since its early times, in the form of charcoal. Maybe the first encounter with this element was in the form of wood chars, remaining after trees being hit by light-bolts. From archeological documents it is known that already Egyptians and Sumerians used charcoal to reduce copper, zinc and other ores in the manufacturing of bronze.

Carbon reached its most glorious moment in 18th century where it stemmed industrial revolution as the fuel for steam engines. Carbon glory times continue up to now as it is a key element in the production of steel and further diamonds are appreciated not only by jewelers but are also as indispensable ingredients for high performances cutting tools.

In the age of nanotechnology, carbon can thus be seen as an “old but new” material. The discovery of carbon nanotubes [3] (successively “rediscovered [4]” by Iijima in 1991 [19]), fullerenes [20] and graphene [1] revamped the interest of material scientists community. Among all other elements, carbon provides the materials scientist the opportunity to investigate nano-structures of all possible dimensionality arrangement: 1D, 2D and 3D. These low-dimensional allotropes provide unique transport properties along with high degree of mechanical stiffness.

The secret for such a long history of successes relies on the ability of carbon atoms to adapt to form different bonding with their neighbors. Atomic orbitals of this element can easily hybridize to form covalent bonds with different spatial configurations.

The aim of this chapter is to introduce to the two low-dimensional carbon allotropes, CNTs and graphene, which will be the subject of the structural and physical characterization performed through transmission electron microscopy. I will first briefly describe the different ways carbon can form covalent bonds using hybrid molecular orbitals. Graphene, and its honeycomb arrangement of carbon atoms, will then be introduced and its structure and transport properties reviewed. As rolled-up graphene sheets single-walled CNTs will then be discussed.

Let's the carbon story begin!

### 1.1 It's all about carbon

Carbon offers the extraordinary opportunity to investigate a material in all possible dimensions. Indeed it can form 0-dimensional structures like fullerenes, 1-

dimensional carbon nanotubes and carbynes, 2-dimensional graphene sheets and finally 3-dimensional graphite and diamond. A graphical representation of these materials is shown in Figure 1.1. All these materials share the same chemical formula: C, since they are made only of carbon atoms. The large differences in their chemistry and physical properties resides in the different ways carbon atoms bond together in these solids.

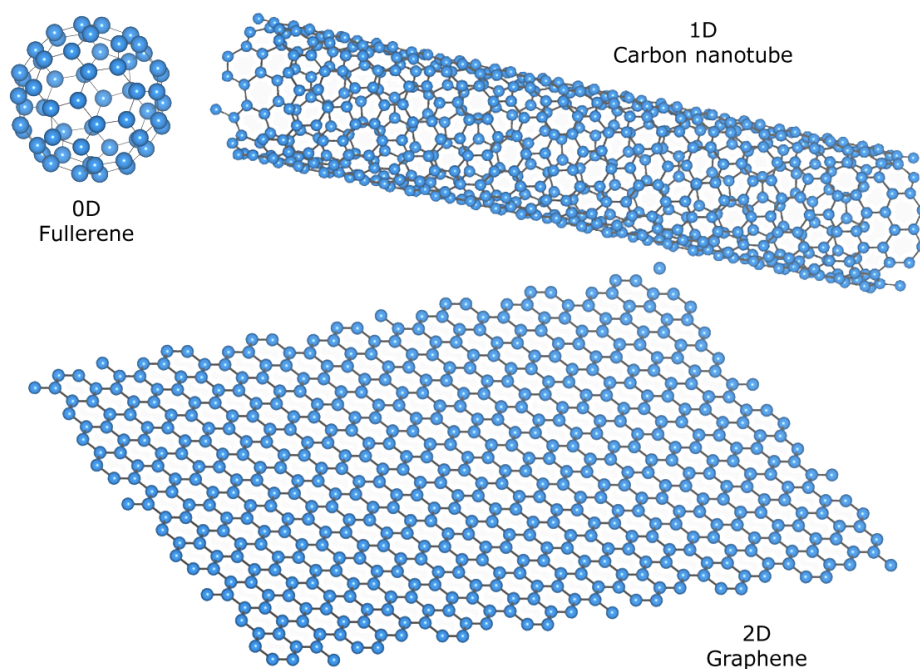


**Figure 1.1:** Graphical representation of the atomic structure of the low-dimensional carbon allotropic forms. From left to right: “0D”  $C_{60}$  Fullerene, “1D” Single Walled Carbon Nanotube, and “2D” Graphene.

### 1.1.1 Carbon atoms

Carbon is the sixth element of the periodic table of elements and it is listed at the top of the column IV. Each neutral carbon atom has six protons and six electrons which occupy the  $1s$ ,  $2s$  and  $2p$  atomic orbitals. The  $1s$  orbital contains two strongly bounded electrons which will be called *core* electrons. The remaining four electrons partially fill the  $2s^2 2p^2$  orbitals, weakly bound to the nucleus and called *valence* electrons.

The second electronic shell  $s$ -orbital has an energy of  $-19.20$  eV, while  $p$ -orbital has an energy of  $-11.79$  eV. If compared with  $1s$  energy of  $-308.18$  eV, the energies

of the second shell are really close each others. Electrons can thus move easily, jumping from one orbital to another and the wavefunctions of these electrons can readily mix up. This mixing of  $2s$  and  $2p$  atomic orbitals is called *hybridization* and when one  $2s$  electron will mix with  $n$   $2p$  electrons the resulting state will be called  $sp^n$  hybrid molecular orbital. The final orbital ends up in a completely different spatial configuration accounting for the variety of bonding geometries achieved by carbon atoms.

### 1.1.2 $sp$ hybridization

In  $sp$  hybridization only one  $2p$  orbital joins the  $2s$  orbital making a hybrid orbital perpendicular to the remaining, let's say,  $p_x$  and  $p_z$  components. Figure 1.2 shows a schematic representation of the electronic charge in carbon valence orbitals. The  $sp$  hybrid generates a covalent bond with another carbon in the same configuration giving rise to a linear chain of  $\sigma$  bonds (orange ones in the Figure). The remaining  $p$  orbitals bond to nearby  $p_x$  and  $p_y$  into double  $\pi$  bonds. This is then the case of a triple bond between each carbon, giving rise to a polymerized carbon chain with the strongest ever bond. This is the case of *carbyne*, an unstable allotropic form, which promises to be the mechanically strongest material ever. Unfortunately it has not been isolated yet.

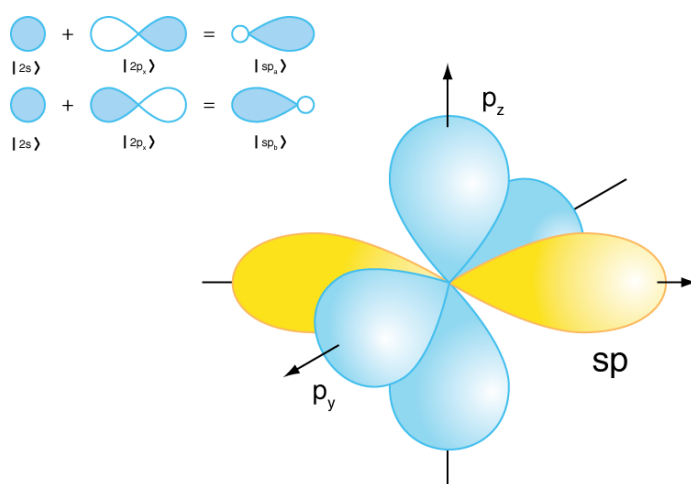


**Figure 1.2:** Graphical representation of  $sp$  hybrid orbitals.

### 1.1.3 $sp^2$ hybridization

In  $sp^2$  only two  $2p$  orbitals blend with the  $2s$  orbital to form a energy level with  $-14.26$  eV. The resulting geometry is trigonal planar, with let's say  $p_x$  and  $p_y$  hybridized with  $2s$  over  $xy$ -plane and the remaining  $p_z$  orbital out of plane. In this configuration carbon is generally trivalent and covalent bonding is formed over the plane with other nearby three carbon atoms, making a binding  $\sigma$  bond. The Figure 1.3 shows a representation of the  $sp^2$  hybrid orbitals. The three orange  $\sigma$  orbitals lays on the same plane forming an angle of  $120^\circ$  between each other. The hybrid  $sp^2$  is the case of graphene and graphite, where strong  $\sigma$  bonds in the plane make a honeycomb lattice structure and usually the available  $p_z$  orbitals blends together in a completely delocalized  $\pi$  state above and below  $xy$ -plane. In graphite 2D honeycomb graphene planes are stacked together one over each other with a weak Wan Der Waals interlayer interaction to keep the solid together, making them nearly free to glide. The delocalized  $\pi$  state all over each hexagon ring contributes strongly to charge transport along the plane, while prevent significant conduction between layers.

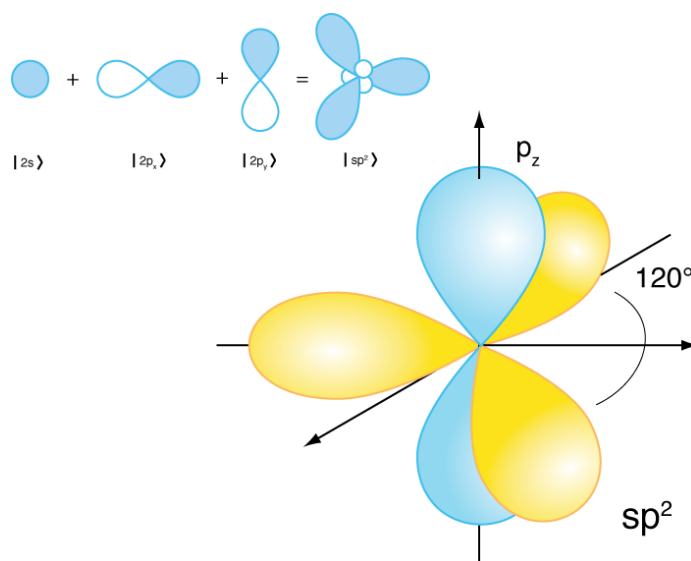


**Figure 1.3:** Graphical representation of  $sp^2$  hybrid orbitals.

### 1.1.4 $sp^3$ hybridization

In  $sp^3$  hybridization the  $2s$  orbital blends with the three  $2p$  orbitals in a single energy level with  $-13.64$  eV. Figure 1.4 shows a schematics of the resulting charge density. The symmetry of the orbitals is tetrahedral, with elongated lobes each one forming an

angle of  $109.5^\circ$  with each other.  $sp^3$  hybridization is characteristic of diamond, where carbon is tetravalent and is connected to other four carbon atoms sharing electrons in  $sp^3$  hybrids in a fully covalent bond. The resulting structure is a cubic lattice with zincblende structure.

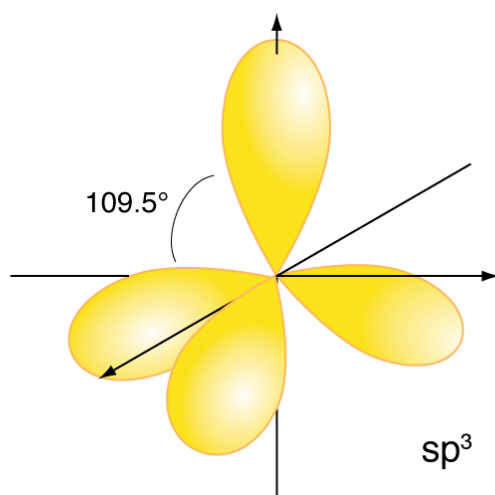


**Figure 1.4:** Graphical representation of  $sp^3$  hybrid orbitals.

Fullerenes, carbon nanotubes and graphite can all be seen as derived using the same building block: the 2D sheet of graphene. In this perspective fullerenes are portions of graphene flakes folded-up to form a spherical carbon balls. Carbon nanotubes are cut out from a graphene sheet along a particular direction and rolled over itself. Graphite, at last, is just a pile of graphene sheets stacked perpendicularly to their planes. For this reason, and because I focused my electron microscopy investigation on them, I will describe more in detail in the next section the structure and properties of graphene and their “kin” carbon nanotubes (from now on simply CNTs).

## 1.2 Graphene

Graphene is a single layer of  $sp^2$  hybridized carbon atoms arranged in a 2D honeycomb lattice. It is one of the most theoretically studied material, since it is the building block of graphite and the “mother” of most carbon allotropic forms. A graphical representation of a graphene flake is shown in Figure 1.5.

Experimental evidence for such a material has been a chimera for decades, and it was even considered conceptually impossible [21]. In a time where cutting-edge

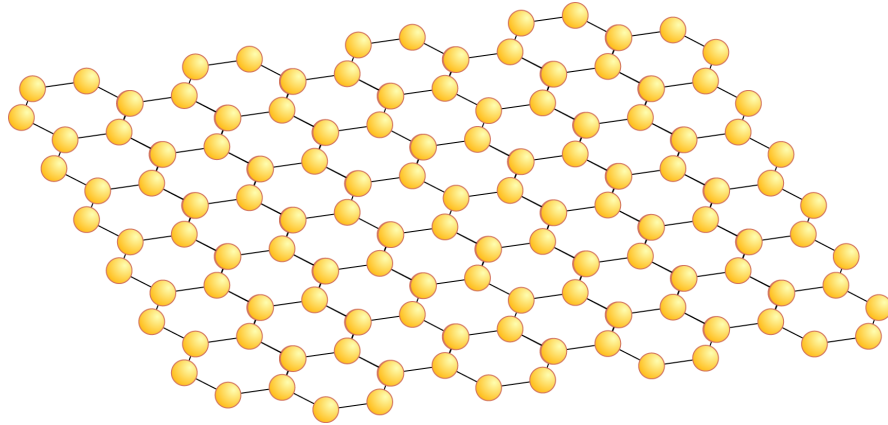


**Figure 1.5:** Graphical representation of a single graphene: a 2D crystal of carbon atoms arranged in a honeycomb lattice.

scientific research is expensive and complex, it seems funny that a break-through in physics could be achieved with simple adhesive tape. In 2004, Andre Geim, Kostya Novoselov and co-workers at the University of Manchester in the UK did that. By mechanically cleaving the edge of an oriented graphite crystal they were able to peel off a single graphene using common adhesive tape and standard  $\text{SiO}_2$  covered silicon wafers [1]. The first experimental AFM image of a graphene flake, obtained using the original Geim's method is shown in Figure 1.6

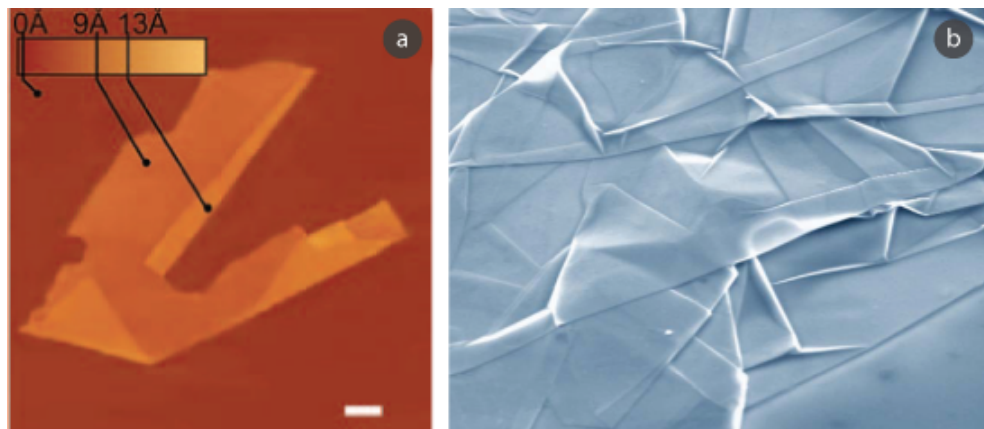


**Figure 1.6:** (a) First evidence of a graphene flake. AFM image shows a single layer flake of graphene, partially folded at the borders. Scale bar is  $1\ \mu\text{m}$ . [Image adapted from [1]] (b) Graphene flakes deposited over  $\text{SiO}_2$  substrate, as they appear in SEM imaging. [Image adapted from [22]]

### 1.2.1 Atomic structure

In graphene carbon atoms are arranged in a honeycomb lattice as shown in Figure 1.7, with an inter-atomic length  $d_{CC} = 0.142 \text{ nm}$ . We can see this atomic arrangement as a combination of benzene rings with a center-to-center distance of  $0.246 \text{ nm}$ .

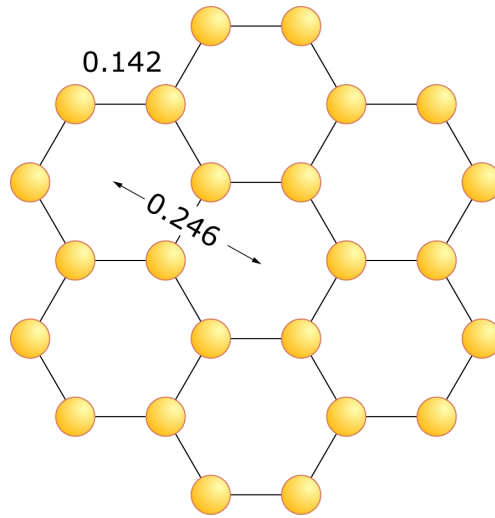


**Figure 1.7:** The honeycomb atomic lattice structure. Each carbon atom has three bonds with other carbons, with a bond length of  $0.142 \text{ nm}$ . Benzene-like hexagons have a center-to-center distance of  $0.246 \text{ nm}$ .

The honeycomb lattice is not a Bravais' lattice, like the hexagonal lattice, instead it can be seen as two interpenetrating hexagonal lattices (highlighted using different colors in Figure 1.8). Since the concepts introduced herein will be the basis for many further discussion in this text, I will spend few more words trying to better clarify the features of this atomic arrangement. To describe the honeycomb lattice from a crystallographic point of view we will need a Bravais' lattice, the hexagonal lattice, and the unit cell will contain two atoms, marked as  $C_1$  and  $C_2$ , as can be seen in Figure 1.8,

The hexagonal Bravais lattice considered has two base vectors  $\mathbf{a}$  and  $\mathbf{b}$ , with  $|\mathbf{a}| = |\mathbf{b}| = \sqrt{3}d_{CC}$  with an angle of  $120^\circ$  between them. The basis of carbon atoms is the couple  $C_1 = (0, 0)$  and  $C_2 = (\frac{1}{3}, \frac{2}{3})$ , expressed using fractions of the unit vectors.

The *reciprocal lattice* is spanned by the reciprocal vectors  $\mathbf{a}^*$  and  $\mathbf{b}^*$ , defined

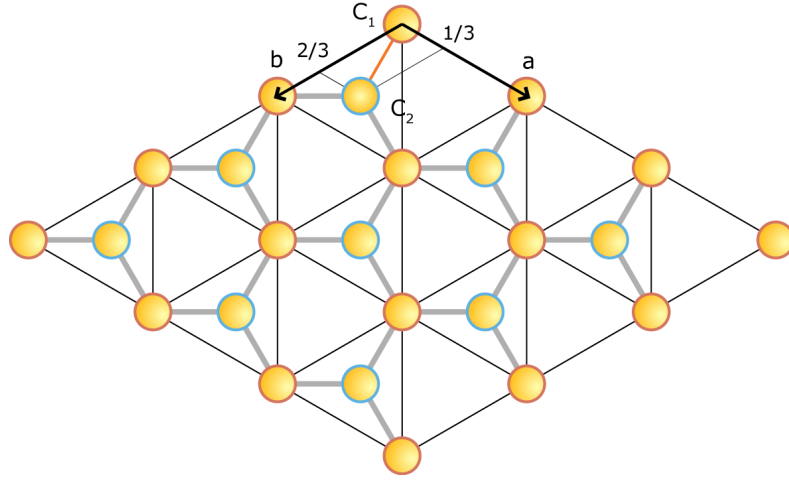


**Figure 1.8:** The honeycomb lattice as an hexagonal lattice, with basic cell vectors  $\mathbf{a}$  and  $\mathbf{b}$ , plus a basis of two atoms  $C_1$  and  $C_2$ .

according to standard relations:

$$\mathbf{a}^* \cdot \mathbf{b} = 0 \quad (1.1)$$

$$\mathbf{b}^* \cdot \mathbf{a} = 0 \quad (1.2)$$

$$\mathbf{a}^* \cdot \mathbf{a} = 1 \quad (1.3)$$

$$\mathbf{b}^* \cdot \mathbf{b} = 1 \quad (1.4)$$

The resulting vectors, satisfying above relations, are depicted in Figure 1.9, and their moduli  $a^*$  and  $b^*$  are related to the intensity of the real space vectors  $a = |\mathbf{a}|$  and  $b = |\mathbf{b}|$  by the relations:

$$a^* = \frac{2}{\sqrt{3}} \frac{1}{a} \quad (1.5)$$

$$b^* = \frac{2}{\sqrt{3}} \frac{1}{b} \quad (1.6)$$

Any linear combination of the vectors  $\mathbf{a}^*$  and  $\mathbf{b}^*$  generates all the points in the reciprocal lattice.

To index reflections in 3D reciprocal lattices and to indicate the families of equally spaced planes in real lattice it is common to use Miller index notation  $hkl$ . In this notation the family of planes parallel to the plane intersecting the unit vectors in segments of lengths (expressed in units of the base vectors)  $1/h$ ,  $1/k$  and  $1/l$ , will be identified by  $(hkl)$ . The inter-plane distance  $d_{hkl}$  will be equal to the normal distance between the surface of this plane and the origin. In reciprocal space the family of

planes  $(hkl)$ , will corresponds to the vector  $\mathbf{t}_{hkl} = (h, k, l)$ , which is perpendicular to the family of planes, and its modulus  $t$  is inversely proportional to the inter-plane distance  $d$  according to the relation:

$$t_{hkl} = \frac{1}{d_{hkl}} \quad (1.7)$$

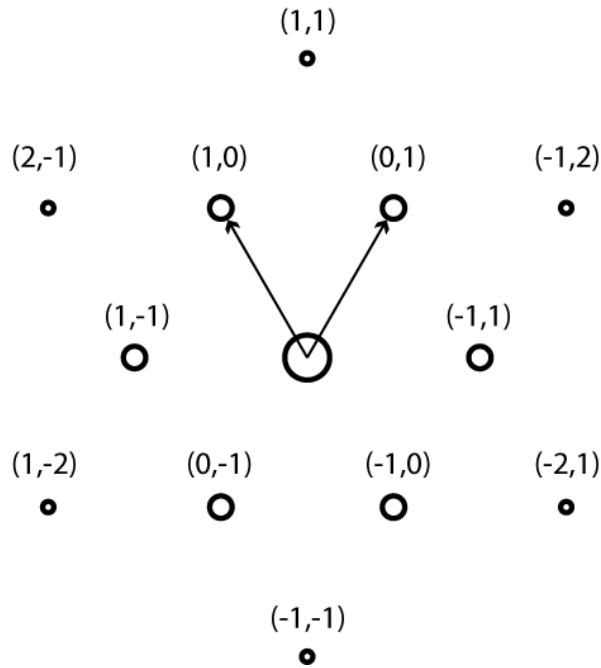


**Figure 1.9:** Reciprocal lattice for the hexagonal honeycomb lattice. The first hexagon of reflections refers to a inter-plane distance of 2.13 Å. The outer hexagon corresponds to 1.23 Å.

Unfortunately this quite simple notation for the description of the honeycomb lattice is not the common one used in crystallography books and articles. Instead of the standard three-index notation, for the special case of hexagonal lattices, to make three-fold symmetries more evident, it is common to introduce a different basis for the Bravais' lattice made of four base-vectors [23]. The new four base-vectors (three in our 2D case), are shown in the Figure 1.10. The new vectors  $\mathbf{a}$ ,  $\mathbf{b}$  and  $\mathbf{c}$  are, of course, linearly dependent since  $\mathbf{c} = -(\mathbf{a} + \mathbf{b})$ .

The additional vector will reflect in an additional index using Miller's notation. A plane in the direct space will then be indicated by  $(hkil)$ , while a direction in the reciprocal space will be noted by  $(h, k, i, l)$ , and of course the indexes must satisfy:  $i = -(h + k)$ . The three base vectors  $\mathbf{a}$ ,  $\mathbf{b}$  and  $\mathbf{c}$  describing our 2D honeycomb

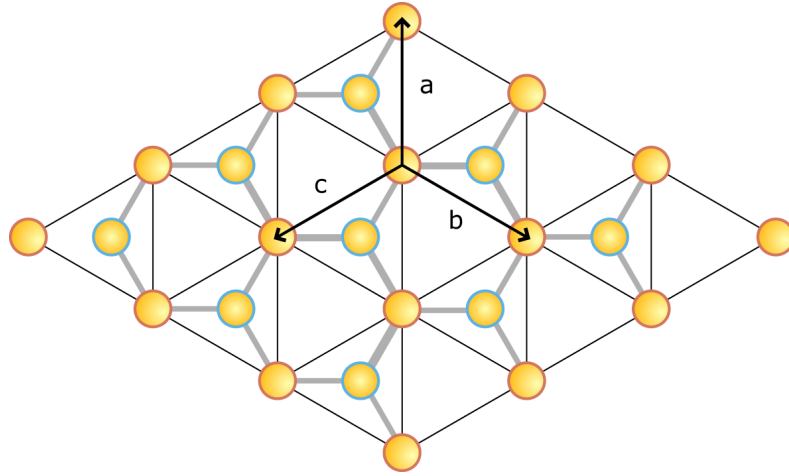


**Figure 1.10:** The three-vectors system for the honeycomb lattice.

lattice, will transform in the reciprocal space into the reciprocal vectors  $\mathbf{a}^*$ ,  $\mathbf{b}^*$  and  $\mathbf{c}^*$  following standard relations analogous to (1.1), but in this case not all the points spanned by these vectors will be part of the reciprocal lattice, since the originating vectors are linearly dependent.

The reciprocal space spanned is, in this case three times more dense than it should and we must eliminate all the points whose indexes do not satisfy:  $i = -(h+k)$ . The reciprocal space and reciprocal vectors are shown in Figure 1.11 and the reciprocal lattice points are only the highlighted ones. Even if non-intuitive, this new notation clearly express the three-fold symmetry of the lattice directly in the index notation.

As mentioned earlier graphene puzzled materials science physicists for decades. It is the building block of graphite which was indeed very easy to discover and synthesize. Nonetheless any attempt to isolate a single graphene flake resulted in nothing. As a consolation, physicists believed that the existence of perfect two-dimensional crystals is indeed prohibited by thermodynamical considerations [21, 24]. During synthesis of 2D crystals, any nucleation site for graphene, would have a large perimeter-to-surface ratio, thus promoting collapse into closed allotrope forms like fullerenes and nanotubes. All these calculations only refer to perfectly flat and ordered crystals. After graphene discovery in 2004 [1] further transmission electron microscopy studies showed that the three-dimensional structure of freely suspended graphene flakes, in fact, was claimed to be continuously undulated [14, 25]. These ripples, bends and undulations, with typical length of  $10\text{ nm}$  and height up to  $1\text{ nm}$ , provide a gain in elastic energy, but strongly damp thermal vibrations, thus minimizing total free energy [15].

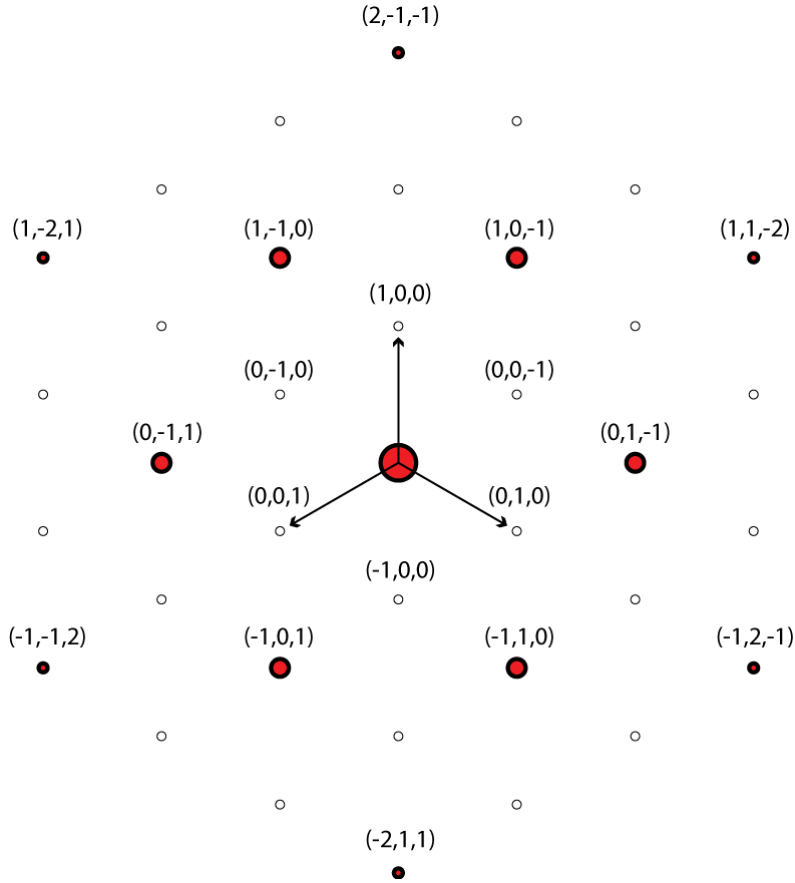


**Figure 1.11:** Reciprocal lattice for the hexagonal honeycomb lattice using a three-vectors basis and  $hki$ -notation. Unfilled points must be canceled since they do not satisfy:  $i = -(h + k)$ .

Single graphenes crystals continue to be quite the exception during synthesis, and the vast majority of flakes results to be multilayered. Even if semantically incorrect, from the point of view of their physical properties it is common in the literature but confusing to refer to these crystals as “graphene” too, to differentiate them from relatively thick graphite samples. In this case we will more correctly call them few-graphene crystals (FGC). The idea is to distinguish these materials from bulk graphite based on their different physical or chemical properties, which are still under investigation. The limit in the number of layers to correctly speak of FGC is not clear, and various attempts result in arbitrary given numbers.

FGC are stacked graphene layers, and in most cases they possess the same stacking order of bulk graphite: ABAB. AA stacking order is not present in any  $sp^2$

carbon based material but we found evidence of mixed AA and ABAB stacking in folded sample of FGC membranes and it was recently confirmed by other researchers [26]. These results will be discussed more in detail in the next Chapter, along with other experimental results obtained using high-resolution transmission electron microscopy.

### 1.2.2 Electronic structure and potential applications

The honeycomb lattice arrangement of carbon atoms determine unique electronic properties for graphene membranes. Graphene is a young material, being isolated experimentally only in 2004. Even if theoretically studied and characterized for decades, experimental results confirming expected chemical and physical properties are performed continuously every day. It is therefore impossible to give a comprehensive description of graphene electronic properties, and in this section I will give a brief outlook of its basic electronic structure. I will focus on that transport and magneto-transport properties which make this material unique, and envisage its usage as the next generation material for post-silicon technology.

#### Electronic structure

If we recall the construction of the reciprocal space of the honeycomb lattice, it is easy to see that the first Brillouin zone is a hexagon whose sides are  $1/3d_{CC}$  from the center [8]. Apart from the electrons in the  $1s$  state, the in-plane  $\sigma$  state electrons bonds to other nearby carbon atoms and are not available for the conduction process. On the other side, the  $\pi$  electron, almost completely delocalized, is free to move and participate to conduction. The  $\pi$  state originates two energy bands, and the peculiar symmetry of the hexagonal lattice makes these bands degenerate at the vertex of the hexagonal Brillouin zone where they touch [9]. For this reason graphene is a two-dimensional zero-gap semiconductor.

A representation of the energy bands in graphene is shown in Figure 1.12. The vertex of the Brillouin zone are six points denoted as  $K$  and  $K'$ , and the degeneracy of the bands makes the Fermi surface to reduce to only these six points. A specific feature of the hexagonal structure of graphene is that nearby the connecting points the energy dispersion is nearly linear in the momentum. Since the conduction properties are ruled by electrons in the vicinity of the Fermi level, in the case of graphene carriers will have an energy directly proportional to their momentum [8–10]. This is completely different from other crystalline solids where the energy dispersion nearby

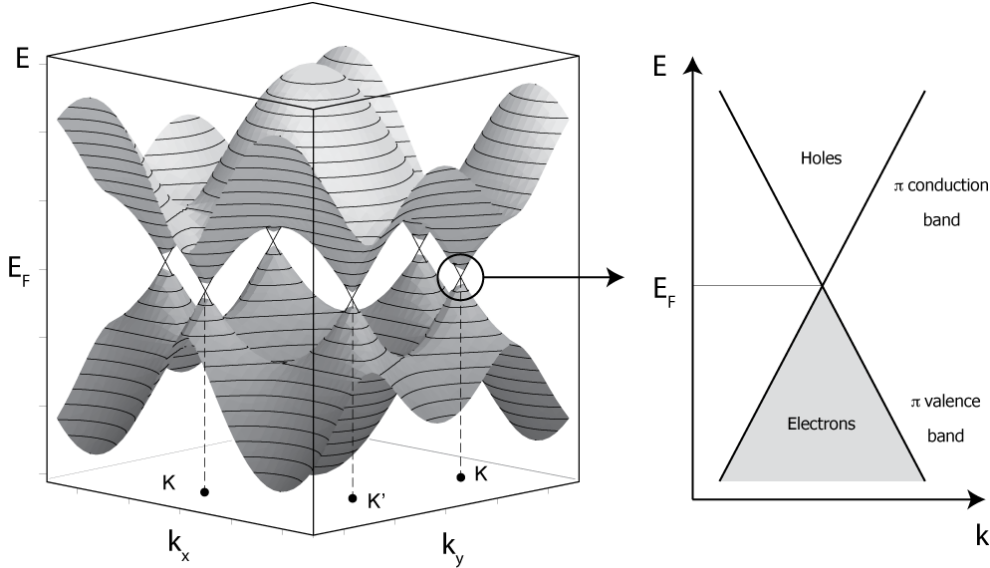


**Figure 1.12:** Band structure for graphene. Fermi surface reduces to six points  $K$  and  $K'$  where the upper and lower  $\pi$  bands join. Nearby the Fermi energy the energy dispersion has a conical shape, linear in momentum. Carriers moving at an energy close to Fermi energy will then be considered as massless particles.

Fermi level is generally a complex curve that can be well approximated by a second-order polynomial. This linear dependence is the key feature to understand the most of the specific properties of graphene [27].

In a crystal, rather than real electrons, we deal with Bloch's waves interacting with the crystalline potential. The effective mass, or *band mass*, of the quasi-particle associated to a Bloch's wave in a crystal is directly proportional to the curvature of the energy band on which it is moving [28]. In the case of graphene, since the curvature of the linear band nearby Fermi energy is zero, electrons and holes behave as if they were almost completely massless. In this crystal carriers behave like massless photons traveling at the speed of light in a medium. In graphene the speed of light in the crystal, the Fermi velocity, is just  $10^6 \text{ ms}^{-1}$ , and for all these reasons graphene carriers are a unique case in condensed matter physics and are called "*relativistic massless Dirac fermions*" [29].

Another specific feature of graphene 2D crystals, is that electrons and holes behave profoundly differently than in common metals or semiconductors. To describe these quasiparticles in the honeycomb lattice, we need to introduce two separate contributions to their wavefunctions coming from the two different hexagonal sub-

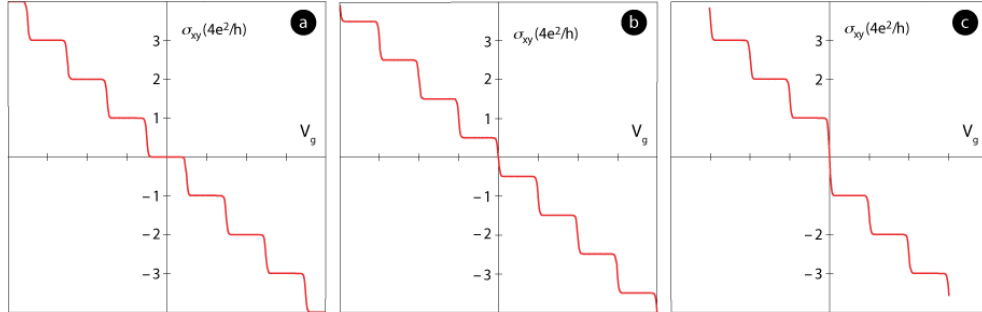


**Figure 1.13:** Quantum Hall effect for: a) conventional metal; b) graphene and c) double layer graphite. In the graph is plotted Hall conductivity as a function of the applied gate voltage. (Adapted from [30])

lattices the honeycomb lattice can be divided into. This two-component description is really similar in its treatment to the concept of spinor wavefunction and suggested to introduce the concept of “pseudo-spin” for graphene holes and electron quasi-particles, indicating in this case the belonging to each sub-lattice.

The result is that both electrons and holes wavefunctions are deeply interconnected, exhibiting analogous charge-conjugation symmetry to quantum-electrodynamics. Moreover, since the wave-function is a two-component spinor, it has to change its sign when electrons move on a closed contour, gaining an additional  $\pi$  phase called the *Berry's phase*. These considerations led to expect an anomalous quantum Hall effect (QHE) for the 2D electron gas in graphene. In conventional 2D electron gases, the QH resistivity at a temperature close to absolute zero, becomes quantized and can assume only fractional values of  $h/e^2$ , where  $h$  is the Planck constant and  $e$  is the electron charge. The precision of the measured values are currently used to define the metrology standard of resistivity.

In graphene, the additional Berry's phase, produces an anomalous QHE, since Hall resistivity can assume only odd integer values [31] (see Fig. 1.13). The discovery of graphene remained questioned, and the real proof that the isolated material was indeed graphene was the observation of this anomalous quantum Hall effect one year after its discovery [11, 32]. The hallmark of the anomalous QHE, as depicted in Figure 1.13, is indeed specific of true graphene, since already a double layer provides standard QHE [32]. Interestingly the anomalous QHE in graphene is visible even at room-temperature [12], since the magnetic energy of electrons in graphene is 1000 times greater than in other metals [33]. A third type of anomalous QHE is presented by two-layer graphite, where the zero level of quantized Hall conductivity is absent [30].

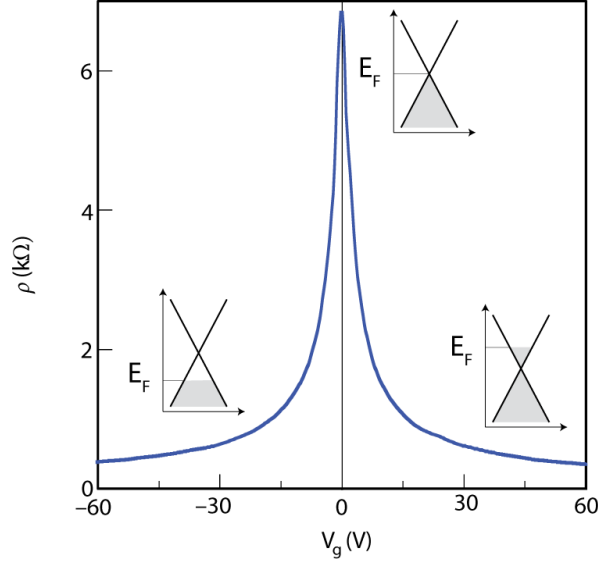


**Figure 1.14:** Electric Field Effect for graphene for the temperature  $T = 1 K$ . The insets show the conical energy dispersion  $E(k)$  and the change in the Fermi energy level  $E_F$  as the gate voltage  $V_g$  is changed from negative to positive. (Adapted from [6])

When a graphene flake is deposited over standard  $300 \text{ nm}$  back-gate  $\text{SiO}_2$  covered wafers, the oxide is used to provide a gate voltage  $V_g$  to the flake so that to modulate the carrier density. Graphene exhibits a pronounced electric field effect, as can be seen in Figure 1.14, and its carriers concentration can be tuned continuously between electron and holes in concentration  $n = \alpha V_g$ , where in the case of a  $300 \text{ nm}$  dielectric  $\alpha = 7.2 \cdot 10^{10} \text{ cm}^2 / \text{V}$ , thus obtaining concentration  $n$  up to  $10^{13} \text{ cm}^{-2}$  and mobility  $\mu$  as high as  $15000 \text{ cm}^2 / \text{Vs}$  up to room temperature [2].

The pronounced electric field effect is indeed slightly affected by variations in the temperature, and the high concentration of available carriers translates to room-temperature ballistic transport on sub-micrometer scale (up to  $0.3 \mu\text{m}$ ). It seems that the room-temperature transport is limited by ripples and corrugations in the graphene flake and partially to some phonon scattering from the  $\text{SiO}_2$  substrate. If the substrate is removed, a mobility of  $200000 \text{ cm}^2 / \text{Vs}$  at a carrier density of  $10^{12} \text{ cm}^{-2}$  is reported for suspended graphene membranes.

Another interesting feature of graphene is that even at neutrality point, when no carrier is injected and the Fermi energy is at the intersection of conduction and valence bands, this material shows a conductance minimum. This is quite unexpected, since the conduction band is completely filled and the valence band completely empty, thus no carrier should be available for transport. It was recently

reported that even in this situation free electrons and holes are still present in local “puddles” [16]. Conductance can then take place between this random network of electrons and holes explaining that minimum charge transport.

### Envisaged applications for graphene

The very high density of carriers achievable in graphene, their great mobility (100 times that of silicon), and the fact that this is mainly unaffected by the temperature, renders it a promising candidate for replacement of silicon in CMOS channels. Ballistic transport at sub-micrometrical scale even at room temperature makes graphene an ideal candidate for spintronic application since you a spin could be injected and recovered without loss of information. The high Fermi velocity in graphene and the possibility to realize low-resistance contact without the formation of a Schottky barrier envisage the realization of fast transistors in the  $THz$  region.

A problem in the actual usage of graphene as a replacement of silicon in electronic logic is that it is always metallic. As a solution, graphene band-gap can be opened by breaking the symmetry of the honeycomb lattice either by introducing superlattice interaction with the substrate or by constraining one dimension of the sheet [33]. The second hypothesis seems easy to reach, since a band-gap of  $0.3 eV$  can be achieved by reducing the flake to a ribbon of just  $10 nm$  in width [34].

Graphene nanoribbons can thus be further engineered by tailoring their edges by doping or by precise crystallographic etching. Edges orientation determine ribbons electronic properties, with zig-zag edges making intrinsically metallic while armchair are semiconducting. The dependence of the electronic properties from the crystallographic orientation make in principle possible to carve an entire single-electron circuit out of a single graphene sheet [6]. Theoretical calculations and the first experimental results suggest that graphene could have enough mechanical and chemical resistance when scaling down, maybe even in the limit of a single benzene ring.

### 1.2.3 Synthesis of graphene sheets

Producing a perfect graphene flake of the dimension of many microns in a reproducible way is still a dream and new synthesis methods are under investigation. At the moment the state-of-the-art production of graphene can be divided in three big classes: mechanical exfoliation, chemical synthesis and epitaxial growth over suitable substrates. I will review here the first two, since they are the methods used to produce the samples further investigated by electron microscopy. A review of the

epitaxial synthesis methods may be found in the work of the group of Prof. Van DeHeer [35].

### **Mechanical exfoliation**

Mechanical exfoliation was the first technique used. The first discovered graphene flake was found among the debris left behind on a silicon oxide wafer by standard scotch tape exfoliated graphite [1]. Mechanical cleavage of large highly-oriented graphite crystals is still the best way to produce large and relatively defect-free graphene crystals.

The method is relatively easy, and the *graphene do-it-yourself kit* requires only a piece of graphite, some clean scotch tape and a standard 300 nm silicon wafer. Sticking a graphite crystal between the tape and then opening it up will exfoliate the crystal in two pieces. Repeating the process several times reduces the thickness of the graphite crystal, and after a certain time you will end up with a piece of only few layers. Placing the tape over the wafer and applying a gentle pressure will ensure that few layers of the crystal will remain attached to substrate surface when removing the tape [36].

Luckily, the light reflected by underlying silicon oxide interferes in a peculiar way when even a single graphene layer is on the surface. This effect makes graphene visible using a light microscope as a feeble contrast emerge between the flake and bare oxide [27]. The oxide layer thickness can be further tailored to enhance graphene contrast depending on the light wave-length used [7]. Without this lucky and unexpected effect, graphene would have been still to be discovered. An image of the overall appearance of the surface of a silicon wafer under the optical microscope is shown in Fig. 1.15.

Graphene flakes obtained with the method above are not suited for TEM sample preparation, since it is difficult to remove them from the SiO<sub>2</sub> substrate. Similar mechanical exfoliation of graphite crystal flakes can be done also by putting some graphite powder into a jade mortar, adding some isopropanol to form a dense paste and then grind it for several minutes using the pestle. Graphene layers will glide and the size of flakes can be easily reduced to few layers and, in some of them, down to single monolayers.

The paste can then be diluted in isopropanol, suspended by aid of sonication and successively centrifuged to sediment larger particles. The result is a good colloidal suspension, but the yield of single layer flakes is almost next to zero. Nonetheless,

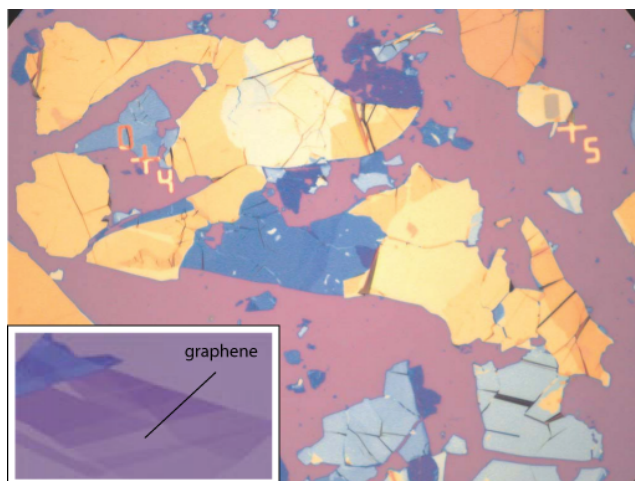


**Figure 1.15:** Thin graphite flakes produced by the mechanical scotch method. The borders of larger flakes sometimes end up in thinner regions. Bluish lighter contrast regions are good single-layer candidates. In the inset is shown a thin flake, with a portion being single layer. [Image adapted from [36]]

after drop-casting the solution on standard holey carbon grids, several thin particles made of few graphene layers can be found and at their borders it is not impossible to find some monolayer protruding into void. The result of TEM observations performed on samples obtained in this way will be thoroughly discussed in the next chapter.

All above mechanical exfoliation methods have severe drawbacks since it is not possible to distinguish graphene from few-layered graphite at the light microscope and promising candidates must be confirmed by scanning microscopy or by electrical measurements. Another major problem of the *scotch method* is that you will deposit on the substrate larger and thicker graphite pieces everywhere and there is no control on the position of the final graphene flake. Moreover all these ways of mechanical exfoliation are not suitable for large-scale industry grade production of graphene.

### **Chemical synthesis of graphene solutions**

Chemists suggested to overcome the low yield of the mechanical method in producing graphene by seeking a way to chemically exfoliate graphite directly suspended in solutions. The basis of most of these methods relies on the well established chemistry of graphite oxide (GO) [37] and graphite intercalated compounds (GIC) [38]. The idea is to induce single layers in graphite crystals to separate from each other and

stabilize them in a colloidal solution, easily mass-scalable and ready to use and deposit in specific locations.

It is beyond the scope of this manuscript to give a comprehensive description of all the chemical approaches developed during last years, even considering that the topic is new and new methods appear almost every week in the literature. In the work presented here, two methods have been used to produce samples for TEM characterization; more detailed information on them is given in the following.

**Coleman's method.** A recent article by Coleman's group in Dublin propose a liquid exfoliation of graphite flakes [39]. Graphite powder is dissolved in organic solvents like *n*-Methyl-Pyrrolidone (NMP) and the presence of the solvent, with the energy provided by sonication, readily exfoliates graphite down to single layers. The role of the solvent is crucial, since NMP has a strong interaction with the honeycomb lattice, thus easily infiltrating between the planes facilitating their exfoliation. Other similar solvents were tried by the group, but NMP resulted the one with the highest yield of single layer flakes.

The method is really simple and clean, since it does not involve modification of the chemical composition of graphite, and residual solvent evaporates without remarkable traces. Produced solutions provide a ratio of mono-layers over multi-layers of  $\sim 1$  wt%, ending in relatively large flakes. The strong interaction between the solvent and the carbon lattice, prevents also one of the most common drawback of graphene in solutions: the scrolling of flakes over themselves.

The method is really simple and straightforward to reproduce and we were able to produce quite good FGC sample even if we couldn't reproduce the same yield in terms of mono-layer over multi-layers ratio.

**Pénicaud's method.** The core of the exfoliation process presented just above is a physical exfoliation of the flakes. Other approaches involve chemical modifications of the pristine graphite in order to produce graphene and FGC membranes. We realized a compound of graphite and potassium, where the metal intercalates between each graphene layer in graphite. Under inert atmosphere potassium is melted over graphite powder. The resulting intercalated graphite compound is then dissolved in NMP, and the solvent oxidize the potassium producing a reactions that makes the compound to explode, separating graphene layers. The result is a colloidal solution of graphene layers suspended in NMP. As a result of the reaction between the NMP and the intercalated  $K^+$ , graphene layers remains in a reduced state and both surfaces of the layers possess a negative charge. This excess charge prevents scrolling and

flocculation of the single layer flakes as they will repel each others. A schematics of the process is depicted in Fig. 1.16.

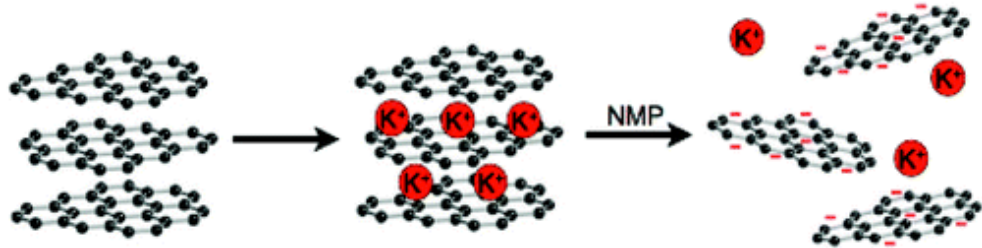


**Figure 1.16:** Schematics of the process of synthesis of negatively charged graphene sheets. [Adapted from [40]]

The negative charges on the surface of graphene flakes can also be exploited to improve their adhesion to metallic surfaces. Deposition substrates can be dip into the solution while a tension polarize their surfaces with opposite positive charges, resulting in improved adhesion. Moreover localized electrostatic assisted depositions can be envisaged using this synthesis method, controlling precisely the positioning of the deposited flakes.

### 1.3 Single Wall Carbon Nanotubes

Let's now introduce the other low-dimensional carbon allotrope that will be the subject of this structural characterization: carbon nanotubes (CNTs). After their discovery CNTs were extensively studied and characterized during 90s and soon after first applications exploited their extraordinary properties [5].

CNTs are rolled-up honeycomb lattice sheets and, as in graphene, their crystal structure determine if they are metallic or semiconducting. These structures have transport properties of a quasi-ideal 1D system and can act as wave-guides for electrons realizing ballistic transport [41]. CNTs peculiar electronic properties were thus exploited for the realization of field effect transistors [42], diodes [43] and more complex circuits for logic operations [44].

We will deal in the next sections with single-walled CNTs (SWCNTs), where the inner cavity is separated from the exterior by only one layer of carbon atoms. Thicker tubes are built with more graphenes in the CNT walls, i.e. with the tube walls made of concentric graphene cylinders. These multiple-shells tube are called multi-wall CNTs (MWCNTs).

### 1.3.1 Atomic structure

Single walled carbon nanotubes can be viewed as made up from a band cut out from a graphene sheet and rolled over itself [41], as shown in Figure 1.17. For each band we can specify a vector  $\mathbf{A}$ , called the *chiral vector*. When the nanotube will roll-up, this vector will be the perimeter of the resulting cylinder and the extremal points  $A$  and  $A'$  will coincide.

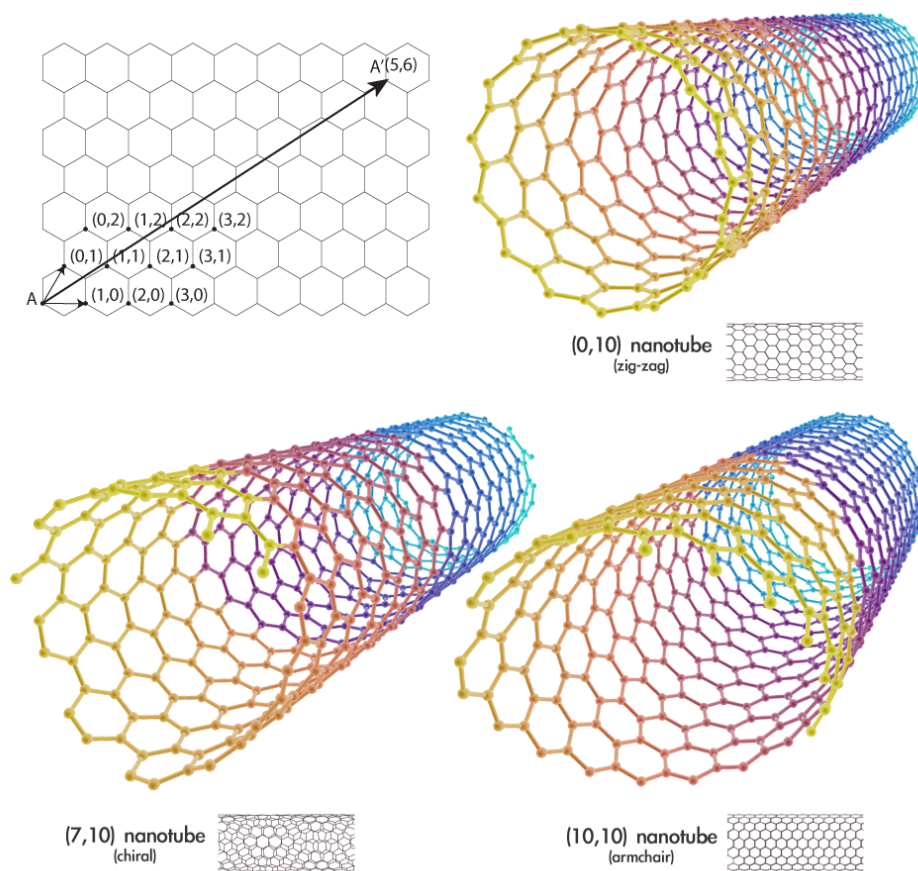


**Figure 1.17:** Graphene reference index system for CNTs indicization and types of carbon nanotubes and tubes examples. A SWCNT can be seen as rolled-up graphene band. The vector  $\mathbf{A}$  will be described by the couple of indexes  $(n, m)$  as shown. Graphene network is cut perpendicularly to  $\mathbf{A}$  so that the SWCNT is rolled up to bringing  $A$  and  $A'$  to coincide along the perimeter.

All SWCNT structures will derive from bands of different orientations and with different widths. An easy way to indicate the specific structure of a tube will then be by giving the vector  $\mathbf{A}$  specific of each band. To indicate a vector over the honeycomb

lattice the standard choice of a basis is unfortunately again different from the one described in Section 1.2.1. In this case we will use two base vectors  $\mathbf{a}_1$  and  $\mathbf{a}_2$  as depicted in Figure 1.17, and a generic vector  $\mathbf{A} = n\mathbf{a}_1 + m\mathbf{a}_2$  will be determined by the couple of indexes  $(n, m)$ . The indexes  $(n, m)$  will then also define a specific SWCNT, and they are called *chiral indexes*. Few SWCNT examples are shown in the Figure as well.

All the geometric dimensions of the tube can be calculated since the knowledge of the two chiral indexes. The modulus of the chiral vector  $A = a_0\sqrt{n^2 + m^2 + nm}$ , where  $a_0 = \sqrt{3}d_{cc} = 0.246 nm$ , and the diameter  $d$  of the tube will then be:

$$d = \frac{A}{\pi} = \frac{a_0\sqrt{n^2 + m^2 + nm}}{\pi} \quad (1.8)$$

The *helical angle*  $\alpha$ , defined as the angle formed between the chiral vector  $\mathbf{A}$  and the base vector  $\mathbf{a}_1$ , is given by:

$$\alpha = \tan^{-1}\left(\frac{\sqrt{3}m}{2n + m}\right) \quad (1.9)$$

In principle CNT can be made out choosing whatever vector  $\mathbf{A}$ , in reality there is no way to differentiate between a  $(n, m)$  tube and its inverse handed one  $(m, n)$ . There is therefore a restriction in the choice of chiral indexes for a tube, according to the following relations:

$$\begin{aligned} n &> 0 \\ n &\geq m \geq 0 \end{aligned} \quad (1.10)$$

In particular when  $n = m$  the tube will be called *armchair* and when  $m = 0$  the tube will be called *zig-zag*. Both these tubes are the only class of *a-chiral* tubes, since their helical angle is zero.

### 1.3.2 Electronic structure

The band structure of CNTs can be derived directly from the structure of the underlying honeycomb graphene lattice, by imposing cyclic boundary conditions. We will overview here, in a qualitative way, the principal characteristics of SWCNTs electronic structure, for a complete description you can refer to specific literature [41].

We will consider the wave vectors  $\mathbf{k}$  as decomposed in  $k_{\parallel}$ , parallel to the tube axis, and  $k_{\perp}$ , perpendicular to the tube axis and therefore parallel to tube diameter. It

is straightforward to impose that:

$$\begin{aligned} \mathbf{A} \cdot \mathbf{k} &= \pi d k_{\perp} = 2\pi j \\ k_{\perp} &= j \frac{2\pi}{A} \end{aligned} \quad (1.11)$$

Usually CNTs have an high aspect ratio: their diameter is usually in the range of  $\sim 1 \text{ nm}$ , while their length along their axis is usually several microns. Therefore they approximate a 1D structure, with an almost infinite length and therefore  $k_{\parallel}$  can assume any value continuously, while  $k_{\perp}$  will be quantized due to the above cyclic conditions.

In the reciprocal space the above conditions represents a family of parallel planes, perpendicular to the direction of the tube perimeter. These planes are equidistant, with a distance  $D$ , calculated from above relations,  $D = 2/d$ . The only allowed energy dispersion curves will be the ones defined by the intersection of this family of planes and the band energy dispersion surfaces of graphene of Figure 1.12. As an example, the situation in the vicinity of the points  $K$  and  $K'$  discussed above is represented in Figure 1.18 for the case of a tube of helical angle  $\alpha = 0^{\circ}$ .

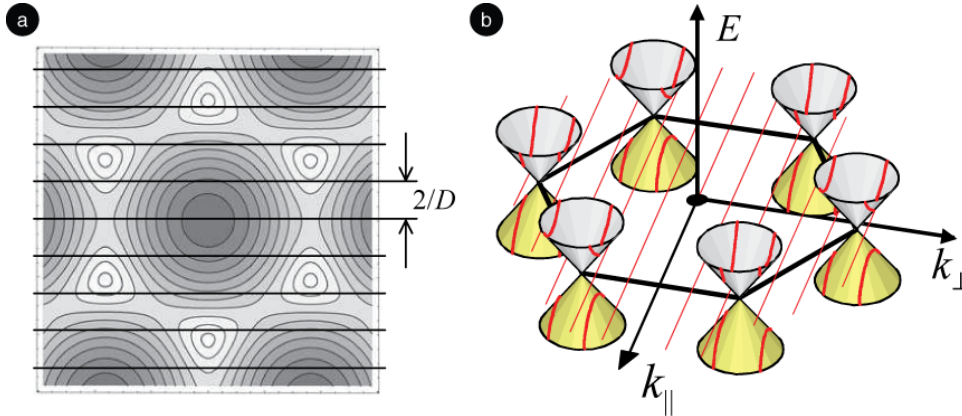


**Figure 1.18:** a) Representation of the contours line of the valence states of graphene. The parallel lines, spaced by a distance  $2/D$ , where  $D$  is the diameter of the tube, represent the allowed values for the wave-vector  $\mathbf{k}$  due to boundary conditions imposed for a CNT of chiral vector  $\alpha = 0$ . b) Representation of the electronic states near the Fermi level as the result of the intersection with the planes of allowed wave-vectors  $\mathbf{k}$  and the conical dispersion surface of graphene.

In general this intersection is different for each nanotubes and depends only of the length and direction of the chiral vector  $\mathbf{A}$ . We can easily see that only if the cyclic boundary conditions make that one of the allowed values for  $k_{\perp}$  is coincident

with one of the points  $K$  or  $K'$  the nanotube will be metallic, otherwise in all other cases it will be semiconductor. In this case the energy difference between the two bands will depend inversely on the diameter of the tube, following the relation:

$$E_g = \frac{2\gamma_0 d_{c-c}}{\sqrt{3}d} \sim 0.8 \text{ eV} \quad (1.12)$$

where  $\gamma_0 = -2.7 \pm 0.1 \text{ eV}$  is an experimental constant.

The condition for a nanotube to be either metallic or semiconductor can be transformed in a condition on its chiral indices  $(n, m)$  [45]:

$$n - m \begin{cases} = 3i & \text{SWCNT metallic} \\ \neq 3i & \text{SWCNT semiconductor} \end{cases} \quad (1.13)$$

where  $i$  is an integer number (including zero), i.e. if the difference between the chiral indexes is a multiple of 3 the tube will be metallic. As an example, all the armchair tubes ( $n = m$ ) will be metallic. The possible cases of intersection are represented in Figure 1.19. Statistically, among all the possible  $(n, m)$  nanotubes, 1/3 will be metallic and the remaining 2/3 will be semiconducting.

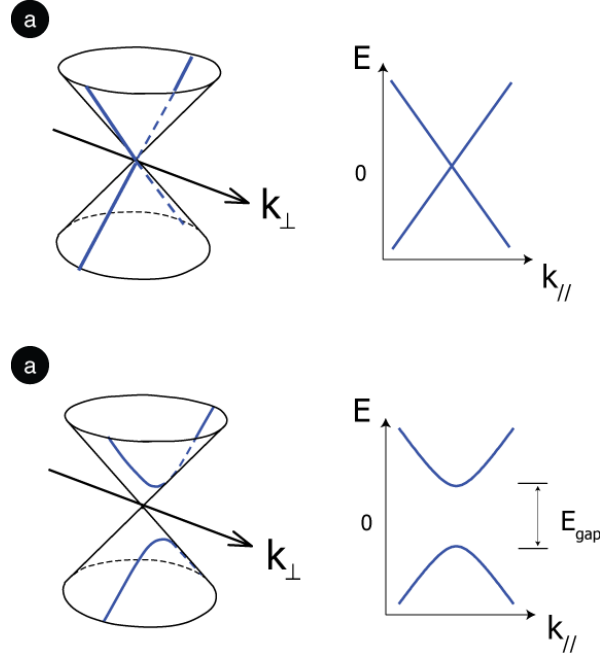


**Figure 1.19:** Detail of the shape of energy bands in a) a metallic SWCNT and b) a semiconductor one.

In imposing boundary conditions on the rolled-up graphene, we did not consider the effect of the bending of the sheet on the electronic structure. The effect of the

curvature of the graphene lattice is more pronounced in smaller nanotubes, where the curvature radius is smaller. The effect of this curvature is to induce an additional band-gap between valence and conduction bands.

For this reason all the nanotubes are strictly speaking semiconducting, but for all practical aspects this curvature induced band-gap is in the range of  $\sim 10 \text{ meV}$ . The same effect will be produced by any other distortion or bending of the tube such a traction along their axis [46] or a torsion of the tube [47, 48]. If compared with typical some  $eV$  semiconductors band-gaps, this  $meV$  effect will be negligible for almost all the practical applications.

### 1.3.3 Engineering the properties of SWCNTs

After 20 years of research CNTs synthesis methods are now well defined and most of their properties are well predicted by theoretical models. The aim of research is now on the technological application of CNTs in electronic devices. Unfortunately the usage of nanotubes by semiconducting industry has revealed more difficult than expected. Handling and positioning of CNTs with the necessary precision is still a far to be realized, due to their intrinsic low reactivity, low solubility and the extreme conditions necessary for their growth hardly compatible with the established silicon technology.

For electronic applications it is crucial to be able to select whether a nanotube is metallic or semiconducting and, in the latter case, to control its bandgap. Current growth method result in mixture of chiral indices, without enough control on diameter and chirality. Current researches investigate methods to select specific chiralities out of a mixture, either by controlling the growth or by post-processing the tubes.

In this scenario we investigated the surface interaction between SWCNTs and graphene membranes. The commensurability of the atomic lattices of these nanostructures makes the tubes to lock in to specific orientation over the membranes. Further, in Chap. 5, I will discuss how this effect can be exploited to select only zig-zag and armchair tube, using graphene membranes as nanoscopic tangential sieves.

Another approach to overcome the intrinsic limitations to SWCNTs actual usage could be to tailor their structural, physical and chemical properties. These modifications can be accomplished by building a complete new material from the pristine tube, achieving a *meta-nanotube*. Some way include doping to change CNTs composition, while preserving their structure, as in BN (boron-nitride) nanotubes

[49, 50]. Other ways focus on functionalization by grafting specific molecules or other nanostructures on the exterior wall of the tube.

The peculiar hollow shape of the tube suggests to fill the tube by other atoms or molecules or materials creating what is called a *hybrid nanotube* [51]. This approach is maybe the most versatile since the only limit is the small diameter of the tube, but solids, liquids and even gases were reported to be used to fill SWCNTs. The filling material will usually assume a completely different atomic arrangement, specific of the constraints of the nanotubes walls. In the next chapter I will present some experimental results obtained in the structural characterization of some hybrid nanotubes.

## Conclusions

In this chapter we presented the basic properties of low-dimensional carbon allotropes. In particular we focused on the description of graphene and SWCNTs.

The peculiar arrangement of carbon atoms in the honeycomb lattice originates the extraordinary properties of graphene based nanostructures. We showed how the orientation and structure of graphene membranes and SWCNTs strongly modify their electronic properties.

In particular whether a graphene flake is semiconducting or metallic depends on the direction and dimension on which it is cut from an infinite honeycomb lattice. Border effects and interactions with substrates further modify the bandgap of this material and open up an almost infinite range of potential applications. In the case of SWCNTs, chirality selection, in order to isolate between metallic and semiconductor behavior, is crucial for the actual exploitation of their properties.

The intimate link between atomic arrangement and physical properties in graphene and CNTs requires a complete structural characterization of these nanostructures. The requirements of atomic resolution and quantitative characterization makes Transmission Electron Microscopy (TEM) an ideal candidate for this task.

In the next Chapters we will describe the experimental parts of this work, that focuses on the advanced characterization of graphene membranes and hybrid nanotubes using TEM. The basic principles of TEM will be shortly described. The peculiar features and the details of the methodology applied will emerge directly during the description of the experimental results obtained for graphene and SWCNTs TEM characterization.



# TEM CHARACTERIZATION OF GRAPHENE AND SWCNTs

Where the telescope ends, the  
microscope begins. Which has the  
grander view?

*(Victor Hugo)*

## Introduction

Recently discovered graphene, and FGC in particular, provide an interesting challenge to materials scientists. More and more experimental results confirm the predictions of theoretical calculations about their extraordinary physical and electronic properties. New production strategies for these materials are presented almost every day. In the previous chapter the structure and electronic properties of graphene and SWCNTs have been discussed. In particular it has been shown that electronic and structural properties of these nanostructures are intimately related, and a structural characterization down to the atomic level is therefore mandatory.

The characterization of FGC and SWCNT should address some basic, but fundamental, questions: which is the dimension of the FGC flakes? How many layers they are composed of? In which order graphene layers were stacked? Which is the chirality of that individual SWCNTs? It is far beyond the aim of this manuscript to provide an exhaustive description of all the available using transmission electron microscopy (TEM) techniques for the structural characterization of these materials. We decided to focus our discussion on the specific assets of electron diffraction and aberrations-corrected high-resolution (HREM) imaging that can address those specific questions stated above. This Chapter is therefore a sort of step-by-step review of the experimental results obtained, guiding the reader through the techniques used and providing the basic knowledges necessary to understand their discussion.

## 2.1 Transmission Electron Microscopy

### 2.1.1 Looking into the *nanoworld*

The greek philosopher Democritus introduced the concept that all matter composing the world, plants, animals and humans was built up from microscopically “small quantum of things”: the atoms. We can imagine that the curiosity to look at what is invisible to human eyes fascinated mankind since ages. This dream had to wait to 17th century, when optical microscopes were invented.

The progress of technology and the knowledge of the structure of the matter pushed forward the limit of what is considered *small* and nowadays microscopy seek the answer to two fundamental questions: which atoms are and where? Which potentials are and where? The power of a microscope is described by its *resolving power*, i.e. the smaller distance between two points it can distinguish as separated.

The resolving power of a microscope, optical as well as electronic, is proportional to the wavelength of the radiation used for imaging. The resolution  $d$  of a microscope

is given by Abbe formula as:

$$d \approx 1.22 \frac{\lambda}{A} \quad (2.1)$$

where  $\lambda$  is the wavelength of the radiation used and  $A$  is the lens aperture, strictly connected to the physical dimension of the lens. For this reason, for a given  $\lambda$  it is not possible to reduce the resolution infinitely.

This is the so-called *diffraction limit* to the resolution of a microscope and it is then set by the smallest wavelength that can be used. The shortest wavelength in the visible region is that of blue color, with  $\lambda = 450 \text{ nm}$  and the best resolution achieved is of the order of  $200 \text{ nm}$ . Unfortunately, shorter electromagnetic radiation, like X-rays is not yet used, since no usable lens has been built so far.

Even if remarkably small, few hundreds nanometers is still too big to investigate the Angstrom-scale arrangement of atoms in materials. Material scientists needed a different type of microscope, and definitely, a different type of radiation. In 1923 Luis de Broglie, during a Science Academy conference in Paris, exposed its idea that at each material particle is associated a wave with wavelength  $\lambda$  given by:

$$\lambda = \frac{h}{p} \quad (2.2)$$

where  $p$  is the momentum of that particle. At the time electrons were known to be easily accelerated by electrostatic fields, thus acquiring great energies and, therefore, smaller wavelengths. Moreover, electrons trajectory could be easily changed by magnetic fields and, using electromagnetic lenses, already in 1931 the first electron microscope was built by Ruska and Knoll.

In the rest of this manuscript we will discuss electron microscopy, and in particular transmission electron microscopy (TEM), reviewing its basics principles and showing the finest result obtained in characterizing the structure of graphene membranes and SWCNTs. Electron microscopy is not the only technique available to materials scientists to investigate the atomic structure of nano-structures. Another type of technique is widely used: scanning probe microscopy, which does not rely on any kind of radiation to form a microscopic image of the sample. Since these techniques have a rather complementary approach to electronic ones and their usage is widespread in graphene and CNTs literature, we would like to briefly review here some of their principal characteristics.

Scanning probe microscopies come in different *flavors*: atomic-force microscopes (AFM), electric-force microscopes (EFM), tunnel-currents microscopes (STM)

and the more recent magnetic-force microscopes (MFM). The basic principle is common to all of those: a very small point, just one atom thick in most sophisticated instruments, is scanned over the sample at a few angstroms from its surface. Tips made of different materials, and different experimental set-up, change the type of interaction between the probe and the surface. A signal proportional to this interaction is collected and related to each position. The result is a map of the surface of the sample, which can be topographical, electrical, magnetic and so on.

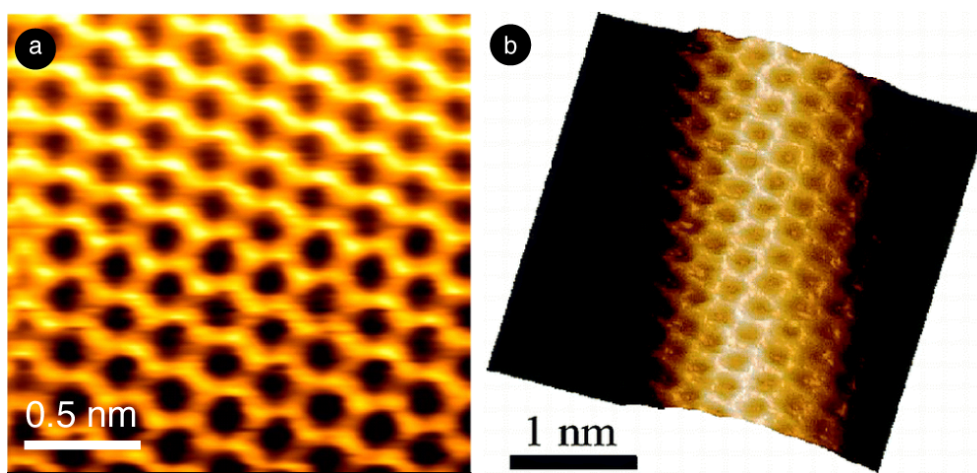


**Figure 2.1:** STM images. a) Image of the surface of a graphite crystal, showing atomic resolution imaging of the honeycomb lattice. [Image courtesy of Dr. F.J. Giessibl, University of Regensburg] b) Image of the surface of a SWCNT [Adapted from [52]].

The lateral resolution of these instruments is nowadays comparable with sub-atomic distances and the sensitivity so high that the map of the charge density associated to outer orbitals of surface atoms was demonstrated. The versatility of this kind of microscopes is really high as samples can be imaged at different temperatures and under different pressure ranges. Figure 2.1 a) shows the STM image of the surface graphene layer in bulk graphite, while b) is the image of the surface of a CNT.

All those methods rely on the interaction between the tip and the sample surface; however there are some drawbacks too. Apart from being a limitation in the characterization of the whole structure of the material, this pose some serious constraint on surface morphology. Homogeneity of the surface of the sample is therefore a stringent constraint, rapid and large height variations make impossible for the probe to follow surface morphology.

Another big constraint of these techniques is that the signal they collect is not

completely morphological but depends on the effective interaction volume of the probe, thus depending on the type of interaction acquired image is not in an univocal correspondence with the surface atomic positions. In the case of graphene on SiO<sub>2</sub> the observed triangular lattice instead of the real honeycomb one is challenging different groups around the world [53].

A fundamental requirement for scanning probe microscopy of nanostructures is that they must be supported on a substrate. In particular for graphene this is considered a limitation to some extents, as sometimes strong substrate-graphene interactions take place and they introduce a significative bias in the images of the structures. TEM on the other side requires that its samples are suspended over void, or if a substrate must be provided, or just over a thin and light membrane transparent to electrons. This condition is particularly important for high-resolution imaging (see further in the Chapter) as a thick substrate would prevent the acquisition of a well contrasted image.

TEM shoots accelerated electrons toward the sample and collect these electrons after they have interacted with the atomic structure of the material. Electrons are charged particles and they will interact with the electrostatic and magnetic potentials present in the sample. In conventional TEM the direction by which they emerge from the sample is used to create an image representative of the atomic structure traversed and other TEM techniques recover additional information about the electro-magnetic fields which have deflected the electrons.

### 2.1.2 TEM imaging

The TEM has been developed as an evolution of the optical microscope and its design is therefore very similar to that of its optical counterpart, where coils generating magnetic fields modify electron trajectories to focalize in the same way as a glass lens does for photons. Fig. 2.2 shows a schematics of the basic elements of a modern TEM.

As in a light microscope there is a source for illumination, in this case emitting electrons which are accelerated by an electrostatic voltage, typically 100 – 200 kV. The illumination system consists of a series of magnetic lenses which modulates the spread of the electronic beam before it arrives on the sample. The objective is the lens forming the magnified image of the sample and it is usually an *immersion type* one: the sample is inside the magnetic field generated by the lens itself. The magnified image of the sample forms on a plane below the objective and the subsequent lenses of the microscope transfer and additionally magnify this image to the final viewing

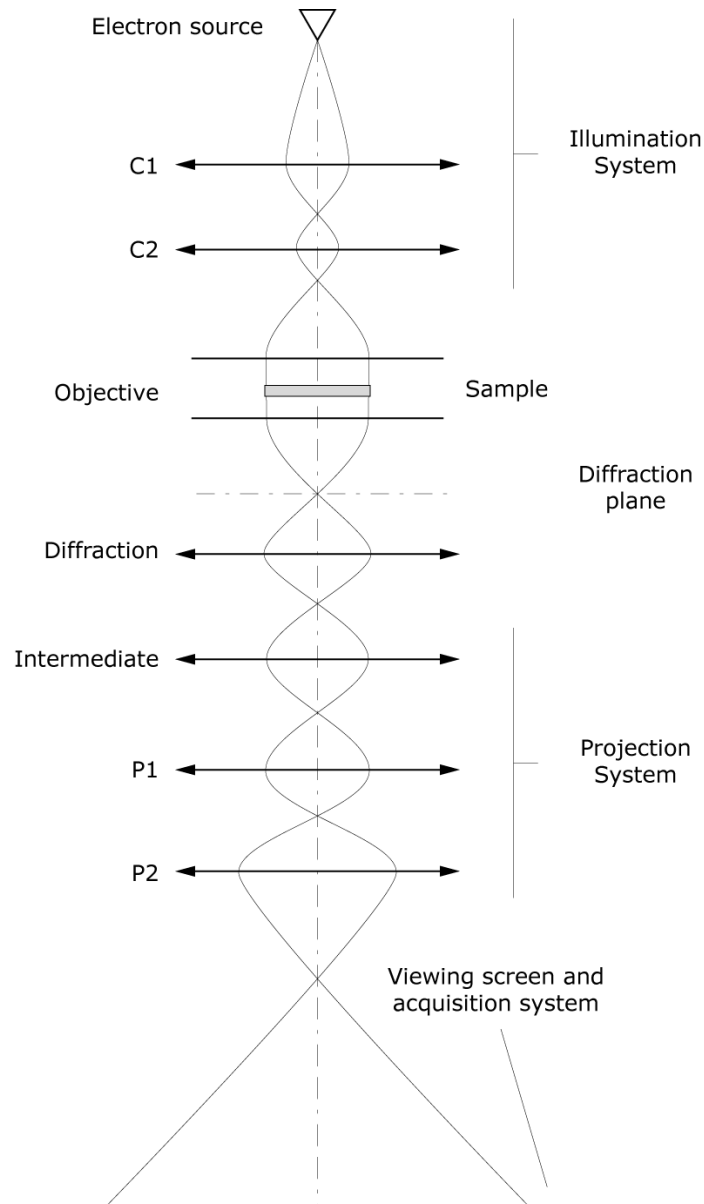


**Figure 2.2:** Schematics of a TEM. The electron source is at the top of the column emitting electrons in a beam modulated by the illumination system lenses ( $C_1$  and  $C_2$ ). The sample is immersed in the magnetic field of the objective lens and the diffraction pattern from the sample creates in the diffraction plane while the magnified image of the sample forms in the image plane just below. Diffraction and intermediate lenses operate to bring either the diffraction plane or the image plane to where the projector system (lenses  $P_1$  and  $P_2$ ) further magnifies them on the final screen.

screen or recording system [54].

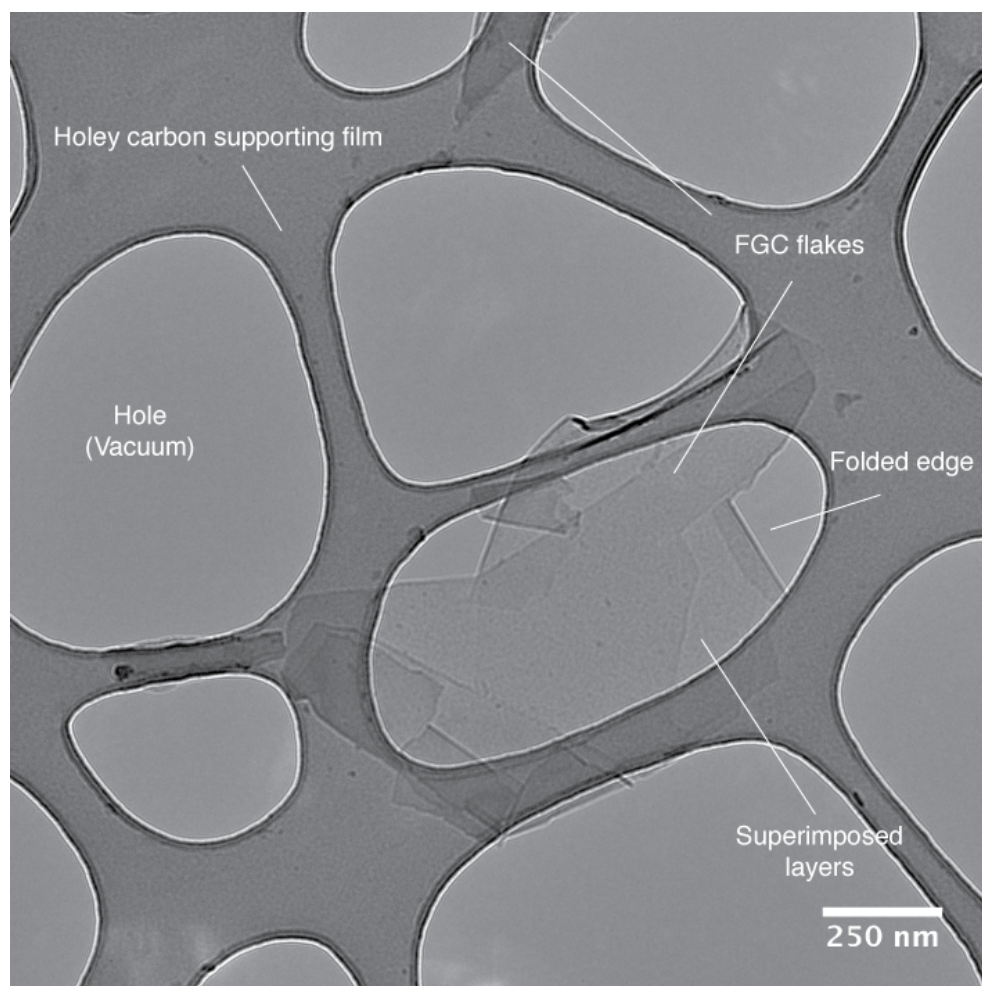


**Figure 2.3:** TEM micrograph of a FLG flake deposited on a holey amorphous carbon film.

In a TEM image, even just at the lower magnifications available, important information about the morphology of the sample is easily obtained. Figure 2.3 shows a thin FLG flake over a holey amorphous carbon film. From the TEM image it is immediately possible to see that the flake has straight borders, folded and partially superimposed. The contrast changes over the surface of the flake inform us that several layers are stacked one over each other, but we cannot say in which order, or how many layers are stacked in each region.

Figure 2.4, shows the intricate network of bundles of MWCNTs dispersed over a TEM grid. At this magnification carbon nanotubes are not seen as featureless one

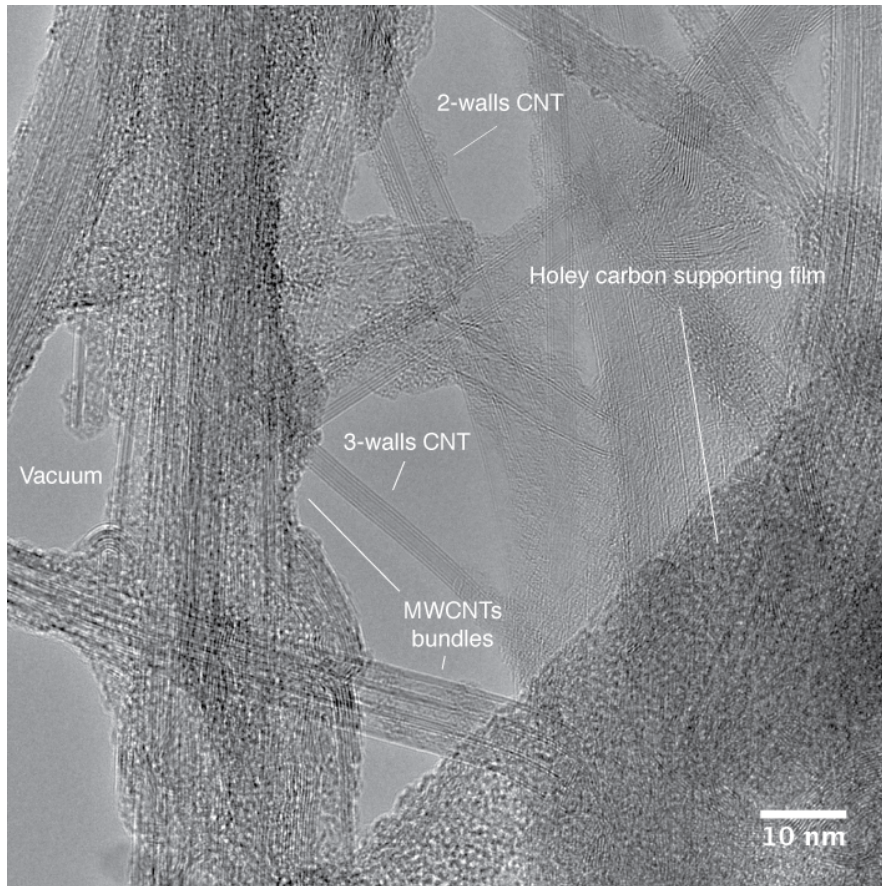


**Figure 2.4:** TEM micrograph of a network of bundled MWCNTs.

dimensional objects, but we can see directly the number of walls composing them.

In TEM the contrast in the micrograph has a completely different origin from that of transmission optical microscopy. In optical microscopy a region of the sample appears darker than its surroundings because in that region the sample adsorbed much more photons: it was less transparent. In the electron microscope there is almost no electron absorbance from the specimen, as the sample is so thin that almost all the electrons illuminating it passes through it.

In TEM it is common to speak of so-called *mass-thickness* contrast and *diffraction* contrast types [55]. *Mass-thickness contrast* arises from the Rutherford elastic scattering of electrons by the atoms of the sample. The cross-section for Rutherford scattering is strongly dependent on the atomic number  $Z$ , so that it will be a function of the mass, the density and the thickness of sample.

In a very simplified scenario we can imagine that thicker or higher- $Z$  areas of the

sample will scatter more electrons off axis than thinner or lighter areas. In the TEM a series of apertures, some of them controllable by the user, intercept these off-axis electrons, removing them from the beam. Heavier, thicker areas, locally scattered more electrons, and that area will appear darker in the final image.

The origin of *Diffraction contrast* is similar to mass-thickness one, but in this case the regular arrangement of atoms in the sample crystal diffracts electrons to specific discrete directions (see next Section for some details). Part of those electrons diffracted off-axis are intercepted by apertures and therefore removed from those contributing to image intensity. Differences in the intensity in the final image therefore relates to different crystallographic domains.

There is another type of contrast in TEM image, the so-called *phase contrast*. This type of contrast is at the basis of high-resolution (HREM) imaging and will be discussed in more details in Sect. 2.3. Operating the microscope in the low-magnification regime, mass-thickness and diffraction types of contrast dominates the description of the intensity in the final image, and can provide important morphological and structural informations about the sample [55].

For FGCs, for example, it is possible to see variations in sample local thickness, but it is not possible to state in which orientation different layers are stacked and to determine their number. More specific and precise informations about the atomic structure of the material under investigation will be obtained using electron diffraction and HREM imaging and these two techniques will be described in the following Sections.

## 2.2 Electron Diffraction from honeycomb lattices

It will be far beyond the scope of this manuscript to give a complete and detailed description of the phenomenon of diffraction in a TEM. In this section we will just provide the essential theoretical background to understand the experimental results presented thereafter.

### 2.2.1 Basic electron diffraction

By definition a lens, a magnetic as well as an optical one, focalizes all the rays exiting the object plane with the same angle in a single point on the back focal plane. In the TEM all electrons scattered by the sample with the same angle are focalized by the objective lens in a point of the so-called *diffraction plane* [55].

Usually the diffraction lens of the scheme of Fig. 2.2 is set to conjugate to the final screen the plane where the objective forms the image of the sample. To form an

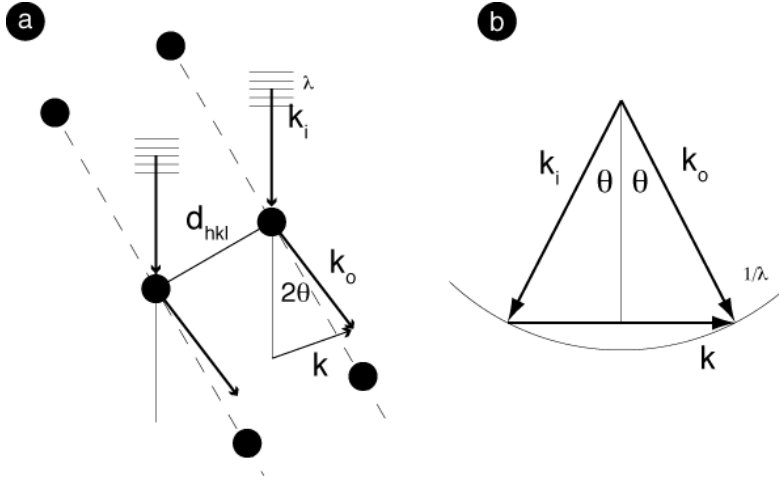


Figure 2.5

image of the diffraction pattern of the sample, the excitation of the diffraction lens has to be changed to conjugate the viewing screen plane with the diffraction plane (see Fig. 2.2).

When the sample has a crystalline order, and the beam is perfectly perpendicular to the sample's surface, the electrons in the beam can be considered as plane wavefronts described by a wave-vector  $k_i$  in the direction of the motion. The process of scattering from the regular arrangement of planes can be described by considering each atom in the crystal as a scatter center emitting a spherical wave stimulated by the incoming wave.

Figure 2.5 a) shows a schematics representation of the diffraction from a regular arrangement of scatterers. An incoming wavefront of wavelength  $\lambda$  and wave-vector  $k_i$  illuminates a series of atoms (black circles) arranged periodically over a family of parallel planes ( $hkl$ ) spaced by  $d_{hkl}$ . Each of the atoms is stimulated to emit a similar wavefront in all directions. In the figure one of these emitted wavefronts is indicated by the wave-vector  $k_o$  forming an angle  $2\theta$  with the direction of the former  $k_i$ .

All the wavefront emitted by the illuminated atoms will superimpose and interfere, and some of the  $k_o$  directions will cancel out due to destructive interference. The so-called *Bragg's law* gives the relation between the direction  $\theta$  producing constructive interference, the wavelength of the incoming radiation and the spacing between the scatterers, and can be expressed by the equation:

$$n\lambda = 2d_{hkl} \sin \theta \quad (2.3)$$

where  $n$  is an integer giving the *order* of the diffracted beam [55].

The wave-vectors  $\mathbf{k}_i$  and  $\mathbf{k}_o$  has both the same length  $|\mathbf{k}_i| = |\mathbf{k}_o| = 1/\lambda$ . Let's consider the vector  $\mathbf{k} = \mathbf{k}_i - \mathbf{k}_o$  representing the change in the momentum of the incoming electrons due to diffraction. Figure 2.5 b) shows, with a simple geometry that:

$$|\mathbf{k}| = 2|\mathbf{k}_i| \sin \theta = \frac{2 \sin \theta}{\lambda} \quad (2.4)$$

Substituting this expression in (2.3) we can translate the Bragg's law in the reciprocal space of momenta, obtaining:

$$|\mathbf{k}| = \frac{n}{d_{hkl}} \quad (2.5)$$

The vector  $\mathbf{g}_{hkl}$  of the reciprocal lattice has a length  $|\mathbf{g}_{hkl}| = 1/d_{hkl}$ , and therefore the Bragg's law in the reciprocal space can be expressed as:

$$|\mathbf{k}| = n|\mathbf{g}_{hkl}| \quad (2.6)$$

The relation between the reciprocal lattice of a crystal and its electron diffraction pattern is therefore clear. The difference between the wave-vector  $\mathbf{k}_i$  of the incident radiation and  $\mathbf{k}_o$  of the diffracted beams is always a multiple of a vector  $\mathbf{g}$  of the reciprocal lattice [55].

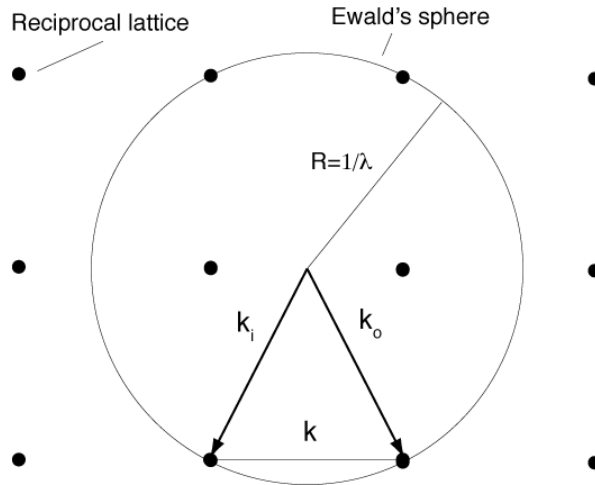


**Figure 2.6:** Ewald's construction for the possible  $\mathbf{k}_o$  for a given orientation  $\mathbf{k}_i$  and radiation wavelength  $\lambda$ .

From the scheme of Fig. 2.5, since  $|\mathbf{k}_i| = |\mathbf{k}_o| = 1/\lambda$ , it is clear that for any given orientation, the vectors  $\mathbf{k}_i$  and  $\mathbf{k}_o$  lie on a sphere in the reciprocal space of radius  $1/\lambda$ , called the *Ewald's sphere*. In this scenario, so-called *the Ewald's construction*, the diffraction pattern for a given direction of the incident radiation

can be obtained with a geometrical construction. The origin of the vector  $k_i$  in the reciprocal space is set that  $k_i$  point to one of the vectors  $g$ . The condition of Eq. (2.6) is therefore equivalent to select all the  $g$  of the reciprocal lattice intersecting the Ewald's sphere of radius  $1/\lambda$  centered in the origin of the vector  $k_i$ . Figure 2.6 shows the Ewald construction for a cubic 2D lattice.

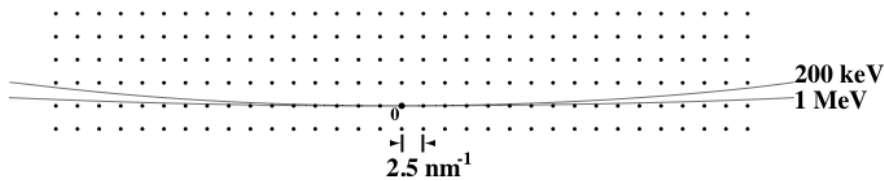


**Figure 2.7:** Representation of the Ewald circle for 200  $kV$  and 1  $MV$  electrons and a square lattice of lattice parameter 0.4  $nm$ . The large radius of the sphere makes that several  $g$  of the reciprocal space intersect its surface.

The wavelength of the electrons in TEM is of the order of few  $pm$  while interatomic spacing is of the order of the  $\text{\AA}$ . Figure 2.7 shows a scaled representation for the radius of the Ewald's sphere in reciprocal space for a square 2D lattice. The radius of Ewald's sphere is therefore three orders of magnitude larger than the spacing between  $g$  points, and it can be approximated by a plane. Thus nearby the central undiffracted beam several  $g$  of the reciprocal space intersect the sphere [54].

Another effect increases the number of experimentally available reflections due to the finite size of real crystals and the finite volume illuminated by the electron beam. The effect of the finite size of the specimen volume transforms perfect points in the reciprocal space into small regions. Since TEM samples are usually really thin in the direction of the beam and the illuminated area is large compared to this thickness, in the reciprocal space points are substituted by elongated structure, called *relrods*, in the direction of the incident  $k$  beam, with an extension inversely proportional to the thickness of the sample. [54].

### 2.2.2 Diffraction from plain honeycomb lattice

Let's approximate the Ewald's sphere with a plane and see what happens to the case of a graphene membranes when the electron beam is perpendicular to its surface. Graphene is a 2D crystal, thus its thickness can be considered as nearly zero and the relrods in the reciprocal space will have an almost infinite extension in  $k_z$  direction.

Figure 2.8 shows a representation of the reciprocal space relrods for a graphene crystal and the Ewald plane for an electron beam perpendicular to the surface of the crystal. As the length of the relrods in the reciprocal space is inversely proportional

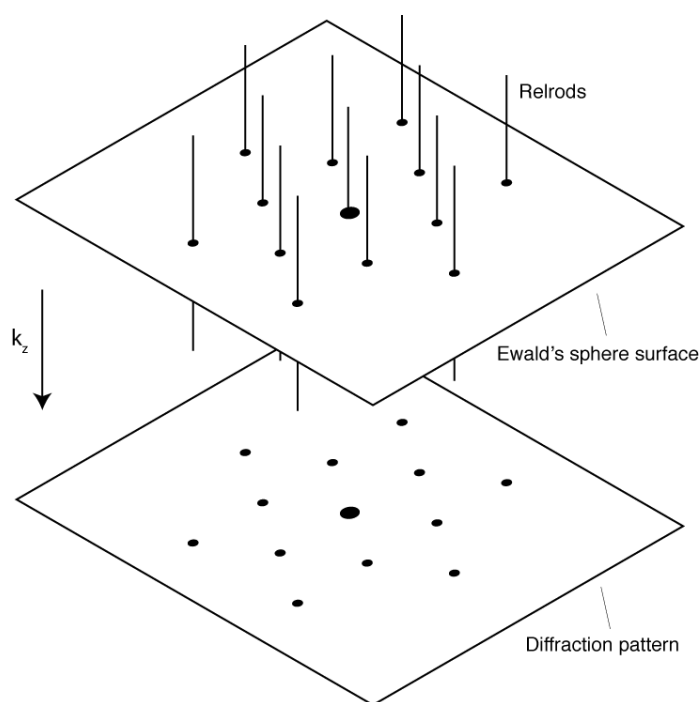
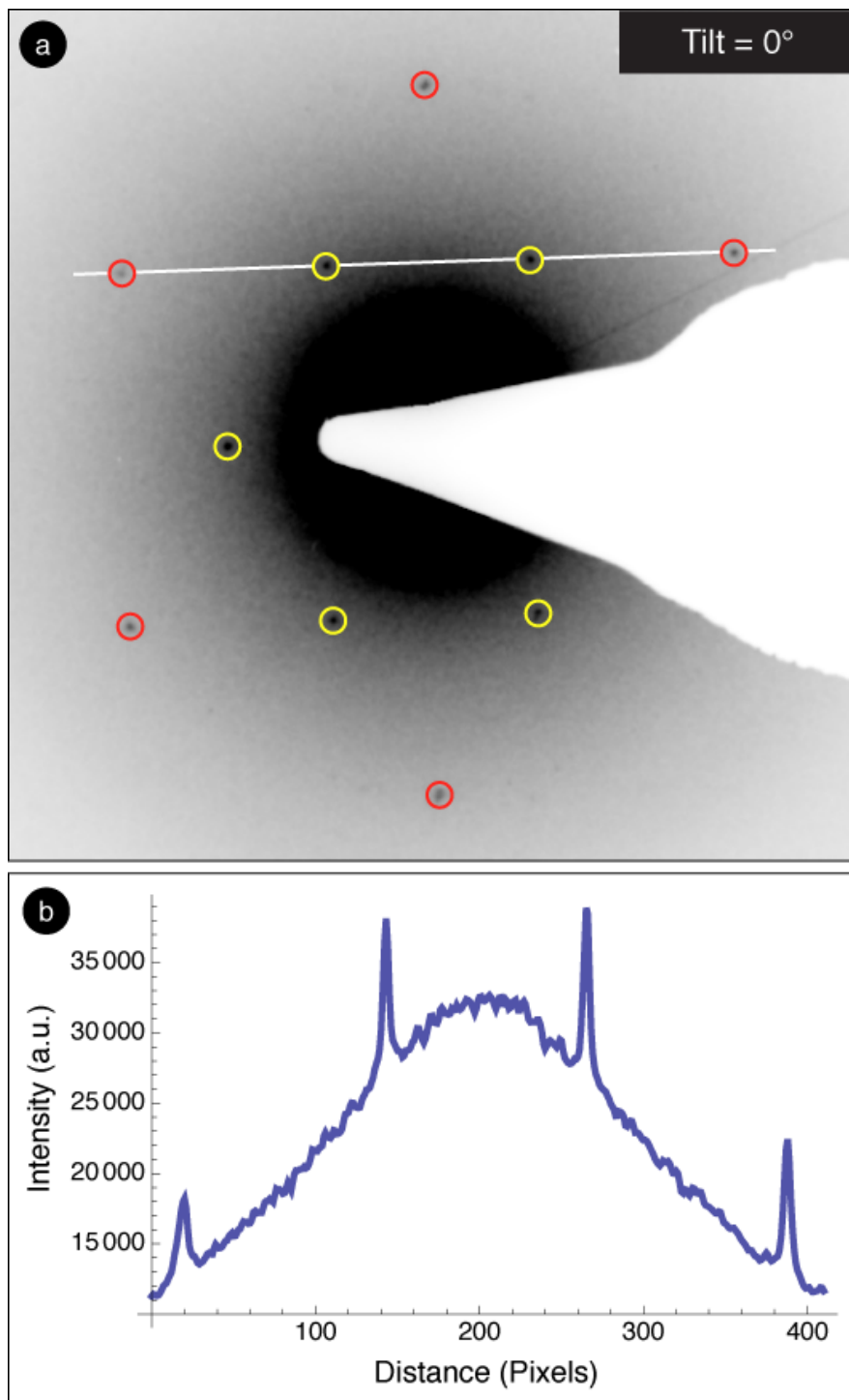


**Figure 2.8:** Schematics of the intersection in the reciprocal space between the reciprocal lattice of graphene and the Ewald sphere surface, determining the electron diffraction pattern for perpendicular illumination.

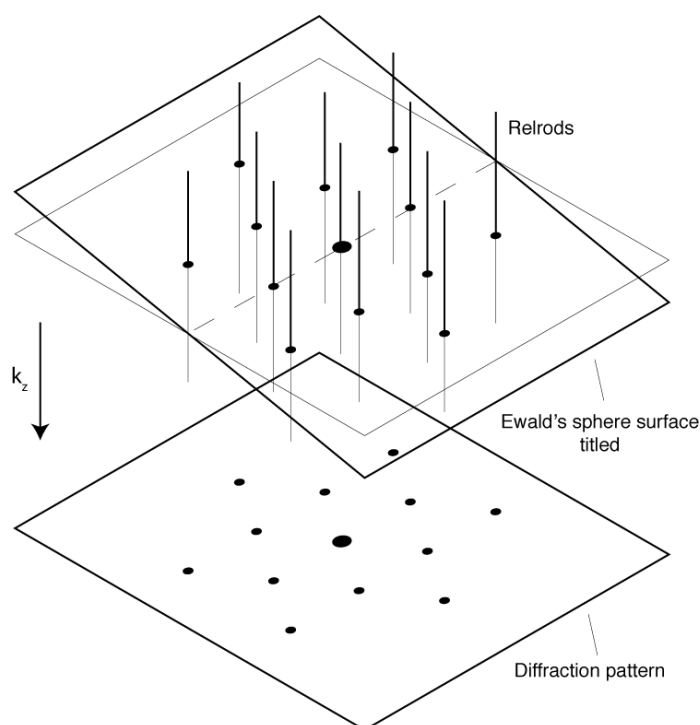
to the thickness of the specimen, in the case of graphene the length of the relrods is almost infinite. The intersection between the Ewald's surface and these relrods originates a diffraction pattern with the same geometry of the calculated reciprocal space of Fig. 1.9.

Figure 2.9 a) shows the experimental diffraction pattern for a graphene crystal, acquired at  $80\text{ kV}$ , while b) shows a linescan along the line indicated in the diffraction pattern. While the geometry of the pattern is regulated by the symmetry of the lattice, the intensity of the spots is regulated by the *structure factors*. For graphene, the calculation of the structure factors shows that the intensity of the spots of the inner hexagon should be stronger than that of the outer one.

An intrinsic feature of 2D crystals, like graphene, is that the diffraction pattern is not changing when the direction of the incident beam is tilted with respect to the normal to sample's surface: graphene crystals are always *oriented*. Figure 2.10 shows the Ewald's sphere surface and the reciprocal space relrods in the case of a tilted flake or illumination. As the relrods are *infinitely* long and their intensity continuous in the direction of elongation, the diffraction pattern will conserve its hexagonal symmetry



**Figure 2.9:** a) Experimental diffraction pattern from a monolayer graphene flake under normal illumination. (Intensity inverted) b) intensity profile of acquired along the line indicated in the pattern.



**Figure 2.10:** Schematics of the intersection in the reciprocal space between the reciprocal lattice of graphene and the Ewald sphere surface in determining the electron diffraction pattern in the case of tilting.

and the relative intensity of spots.

As an experimental example, Figure 2.11 a) shows the diffraction pattern for the same graphene crystal as in Fig. 2.9 tilted by  $10^\circ$ . Figure 2.11 b) shows the intensity profile along the line indicated in the pattern. At every orientation of the crystal with respect to the direction of the beam, the intensity of the inner reflections is always stronger than that of the outer hexagon ones.

As already mentioned, this intensity ratio invariance of the diffraction spots is really intrinsic to the two-dimensionality of the crystal. Even just a two-layers flake produce a completely different intensity in the diffraction pattern. Independently from the stacking order the symmetry of the reciprocal space is identical to that of graphene crystals. In this case the relrods have a modulation in intensity along the elongation direction.

In Fig. 2.12 this effect has been stressed by showing the relrods intensity as ellipsoids of different dimension, representing the iso-surfaces of maximum intensity. When the illumination is perpendicular to the surface of the flake the diffraction pattern is still similar to that of a single layer. When the crystal is tilted, Ewald's

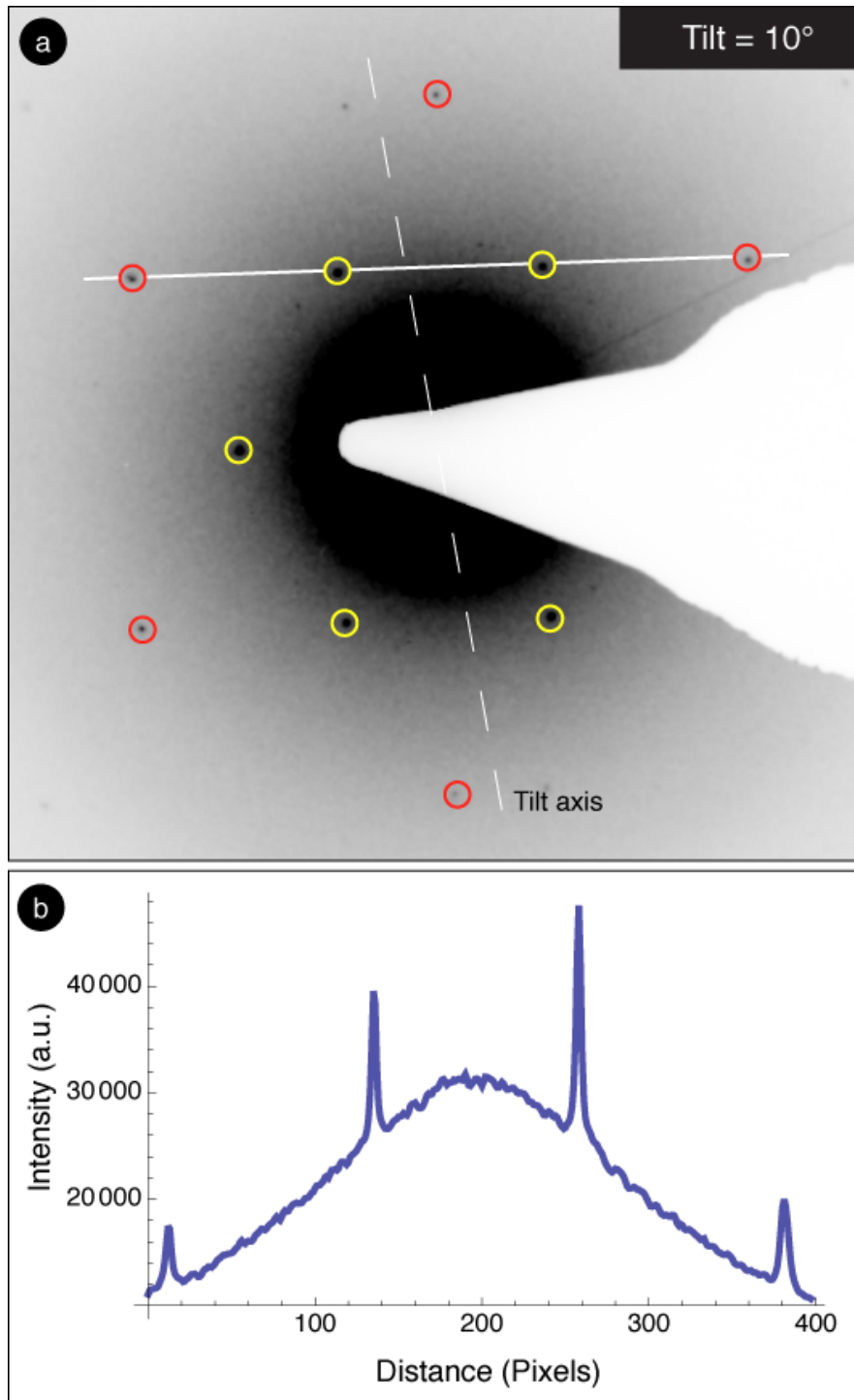


**Figure 2.11:** a) Experimental diffraction pattern from a monolayer graphene flake under tilted illumination by  $10^\circ$ . (Intensity inverted) b) Intensity profile of acquired along the line indicated in the pattern.

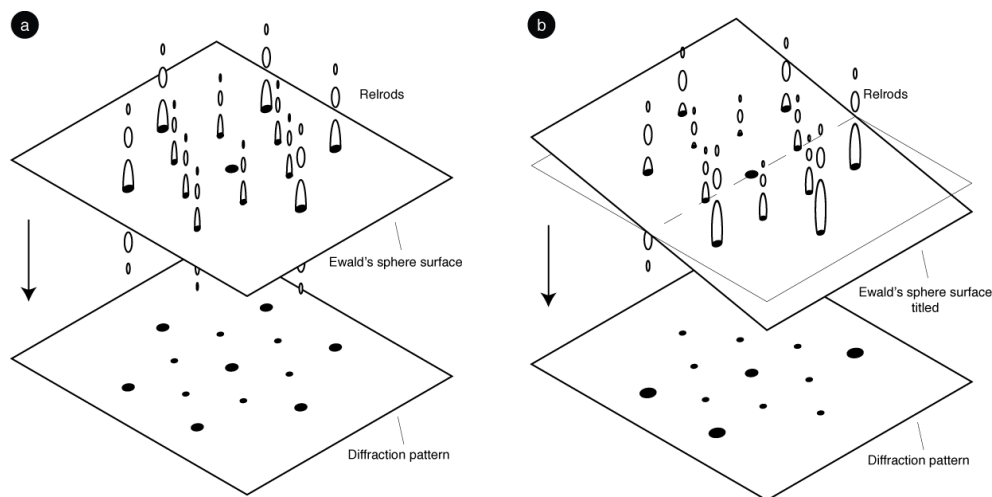


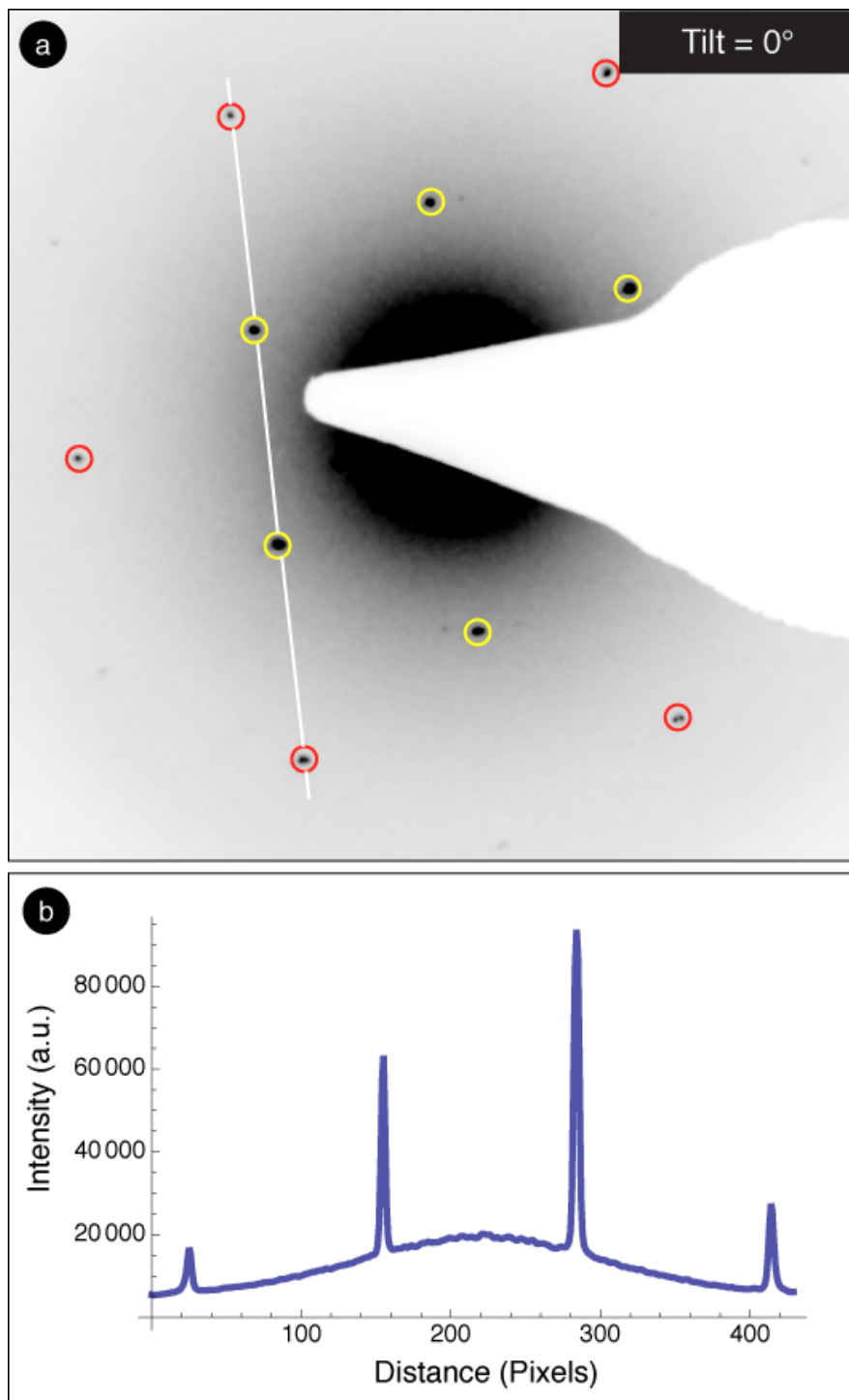
**Figure 2.12:** Schematics of the intersection in the reciprocal space between the reciprocal lattice of graphene and the Ewald sphere surface. a) Case of perpendicular illumination. b) Case of tilted illumination.

plane intersects these ellipsoids in a different way and the diffraction spots on the outer hexagon, corresponding to a spacing of  $0.123 \text{ nm}$  can be much more intense than the inner ones [14].

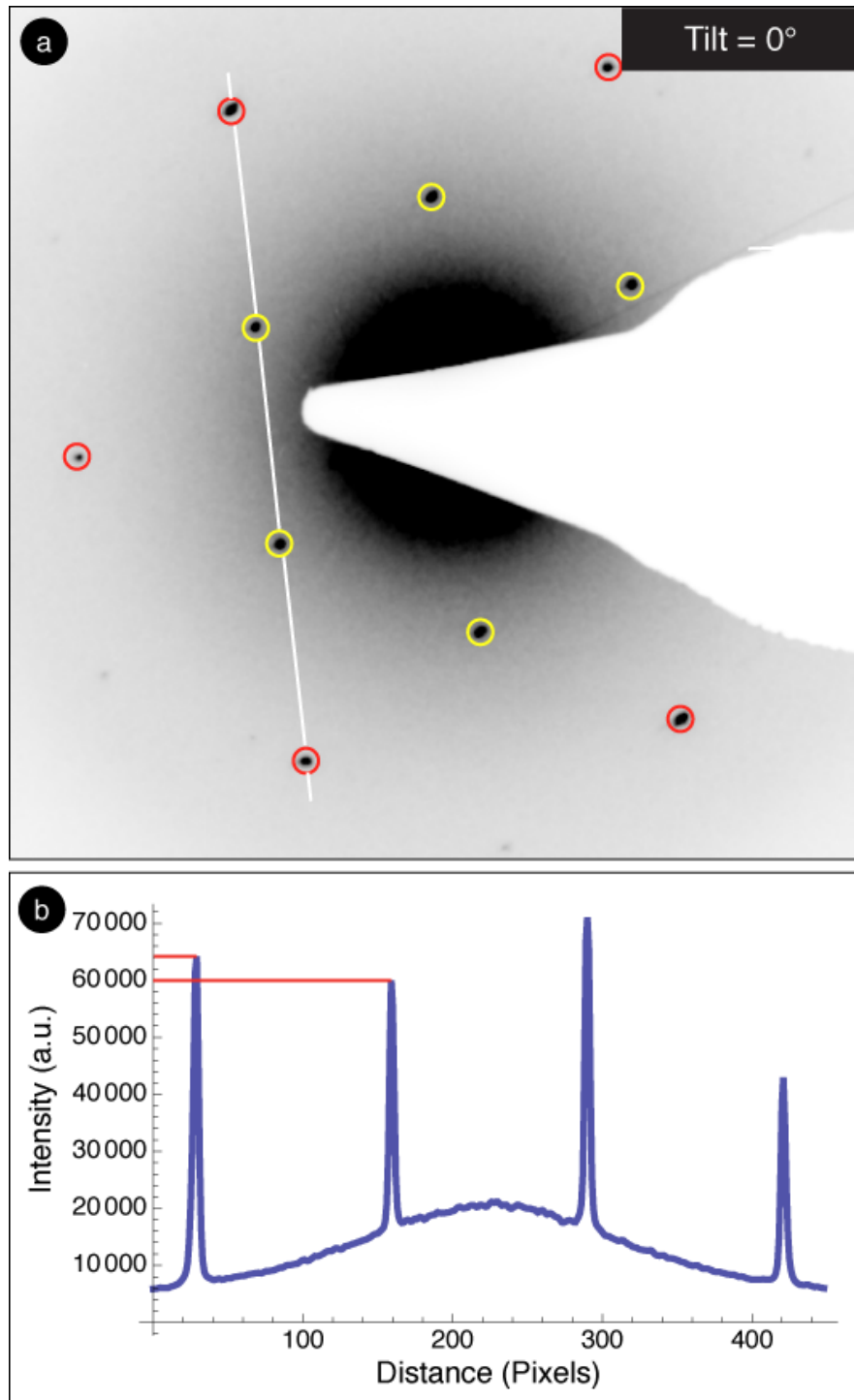
Figure 2.13 a) shows the experimental diffraction pattern of a two-layers graphite flake<sup>1</sup>, under perpendicular illumination. Fig. 2.13 b) shows a linescan along the line indicated in the pattern. The intensity of the reflections corresponding to  $0.213 \text{ nm}$  (yellow circles) is stronger than that corresponding to  $0.123 \text{ nm}$  (red circles). In general, when the number of layers is higher, calculation of the structure factor for relatively thick graphite crystals, shows that the outer reflections are always stronger than the inner ones. The case of two layers under perpendicular illumination is similar to the mono-layer one.

Figure 2.14 a) shows the diffraction pattern for the same graphite flake, in this case tilted away by  $10^\circ$ . Fig. 2.14 b) shows the intensity profile acquired along the line indicated in the pattern. It is evident, as marked in the profile, that the intensity of one of the outer reflection is more intense than its adjacent internal one. Even just this small intensity difference is sufficient to say that the flake is not a mono-layer graphene. Diffraction analysis of FGC flakes provides a fast and reliable method to

<sup>1</sup>The precise determination of the number of layers in a flake is performed analyzing the high-resolution image of the folded borders of the flake, and will be discussed later in this chapter.



**Figure 2.13:** a) Experimental diffraction pattern from a multilayer graphene flake under perpendicular illumination. (Intensity inverted) b) Intensity profile of acquired along the line indicated in the pattern.



**Figure 2.14:** a) Experimental diffraction pattern from a multilayer graphene flake under tilted illumination by  $10^\circ$ . (Intensity inverted) b) Intensity profile of acquired along the line indicated in the pattern.

characterize a dispersion of flakes looking for evidences of graphene crystals [14, 39].

### 2.2.3 Diffraction from rolled honeycomb lattice

As we previously discussed in Chapter 1, SWCNTs can be seen as rolled-up graphene sheet. We thus expect that the diffraction pattern of these structures will have some similarity with that of the pristine honeycomb lattice. On the other hand the diffraction pattern of SWCNT is quite different from that of graphene, due to the curvature and helicity of its lattice. The qualitative description of the diffraction pattern of SWCNTs can be seen as starting from considering the SWCNT as composed of repeated helices of carbon atoms. Carbon atoms are equally spaced along the helix, and the other helices add up with the same helical angle  $\alpha$  as the former one to complete the structure [56].

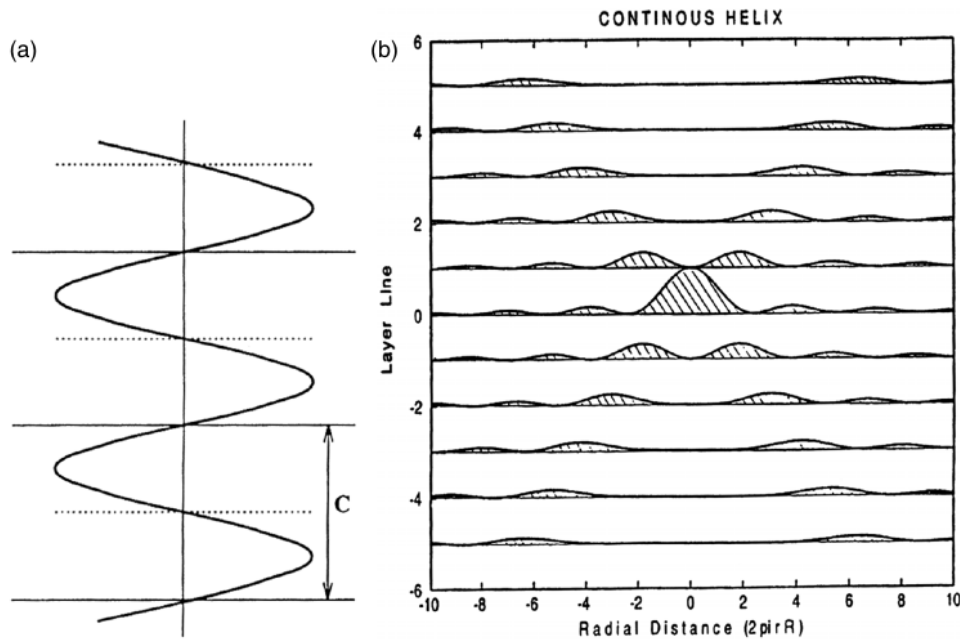


**Figure 2.15:** a) Schematic of a continuous helix of radius  $r_0$  and pitch length  $C$ . b) Corresponding simulated diffraction pattern for the continuous helix. It consists of discrete lines separated by  $1/C$  and with the intensity modulated by  $|J_l|$ . [From [45]]

As an example to illustrate the scattering from helical structures, Figure 2.15 shows the calculated diffraction from a scattering potential shaped as a continuous helix of radius  $r_0$  and pitch length  $C$ . The scattering factors and the diffraction amplitude are described by the equation, in polar cylindrical coordinates  $(R, \phi, z)$

[45]:

$$I(R, \phi, z) = I(R, \phi, l) = r_0^2 V_0^2 [J_l(2\pi r_0 R)]^2 \quad (2.7)$$

where  $l$  is an integer number and  $J_l$  is the Bessel's function of order  $l$ . There are two important characteristics of the diffraction pattern from an helix that deserve special mention. One is that the intensity falls only on discrete lines, spaced of  $1/C$ , indexed by the the integer  $l$ ; the other one is that the intensity on each of these lines is modulated proportional to to the square of the modulus of the Bessel function of order  $l$ .

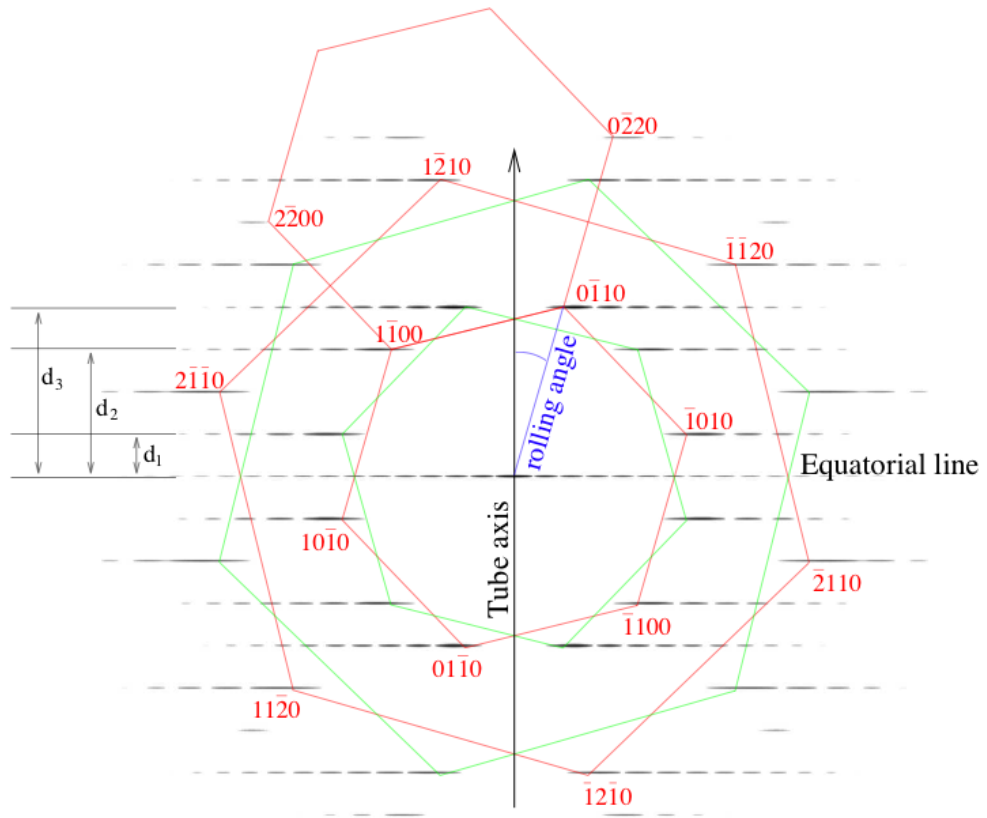


**Figure 2.16:** Simulation of the diffraction pattern for a chiral SWCNT. Hexagonal arrangement of maxima are marked and indicized according to graphene lattice convention.

In the case of nanotubes we need to consider discrete scatterers placed along each helix the formula describing the diffraction intensity is more complex the main characteristics due to the helical structure will remain. Figure 2.16 shows the calculated diffraction pattern for a chiral carbon nanotube. Diffraction intensities fall on discrete lines and along these lines the intensity is modulated proportional to the

square modulus of a Bessel function. The line passing horizontally in the center of the pattern is called the *equatorial line*. This line is perpendicular to the tube axis and the intensity modulation along this line is similar to that of the interference pattern of a two-slits experiment, where the distance between the slits is equal to that of the nanotube diameter.

The hexagonal symmetry of the honeycomb lattice diffraction pattern is recovered considering the positions of the maxima of intensity over each line. In the Figure these positions have been connected with hexagons and indicized in the same way as in the graphene diffraction. The diffraction from a single SWCNT presents two series of hexagonal pattern, represented in green and red in the figure, corresponding to the lattices of the upper and lower face of the tube. These two set of spots are rotated one respect to the other, and the angle of this rotation is related to the rolling angle of the tube.

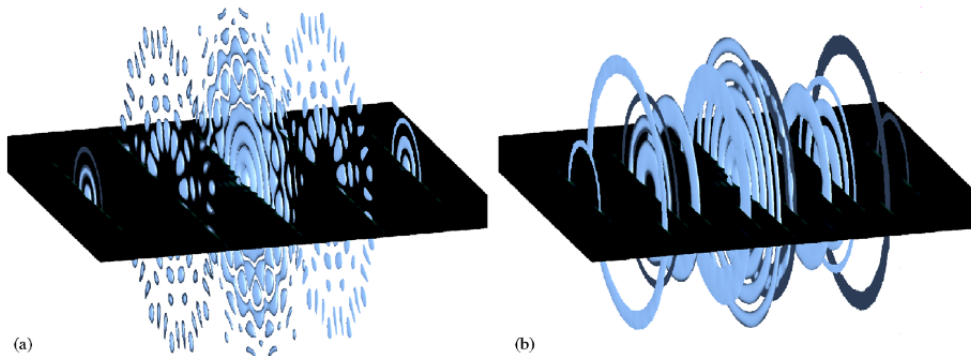


**Figure 2.17:** Reciprocal space representation of a (7, 7) nanotube a) and of a (8, 3) nanotube b). Iso-surfaces are drawn around the higher intensity volume elements. Since the nanotubes are quasi-1D structures in the reciprocal space there are not points but two-dimensional structures. The planar section corresponds to the part of Ewald surface for a beam normal to tube axis. (Image adapted from [57])

A precise and reliable calculation of the rolling angle  $\alpha$  can be done by measuring the distances between the lines  $d_1$ ,  $d_2$  and  $d_3$ . The helical angle is then calculated as [45]:

$$\alpha = \tan^{-1} \left( \frac{1}{\sqrt{3}} \frac{d_2 - d_1}{d_3} \right) \quad (2.8)$$

A rolling angle of  $0^\circ$  corresponds to a zigzag tube and in that case the lines corresponding to  $d_1$  and  $d_2$  coincides. A similar case is that of an armchair tube, with a rolling angle of  $30^\circ$ , where  $d_3$  and  $d_2$  are equal. In both cases the diffraction

pattern is not independent from a rotation of the tube around its axis.

Figure 2.17 shows the reciprocal space and the Ewald surface for a (7, 7) nanotube (a) and an (8, 3) nanotube (b). The chiral tube intensity in reciprocal space is rotationally symmetric around the tube axis and the intersection with the Ewald surface is not changing. In the case of the armchair tube the reciprocal space has a discrete 14-fold symmetry around the tube axis and upon rotation around this axis the intersection changes originating different diffraction pattern geometries.

The chiral indices of a single nanotube can be determined from the helical angle calculated from the diffraction pattern by means of Eq. (2.8), and the knowledge of the radius of the tube from conventional imaging. If the nanotube has a relatively small radius there will be few candidates with that particular combination of rolling angle and radius. The comparison with diffraction simulations of candidates structures will remove any indetermination [57].

As an experimental example, Fig. 2.18 shows the indicized experimental pattern from an individual single-walled tube. The helical angle was calculated to be  $\alpha = 28.3^\circ$  and the diameter of the tube was  $7.48 \text{ nm}$ , thus defining the tube indexes as (32, 29).

## 2.3 High-Resolution TEM of graphene membranes and SWCNT

### 2.3.1 High-resolution TEM principles

The principle of HREM resides in the phenomenon of interference between diffracted beams by the crystal.

Figure 2.19 shows a scheme of the optical set-up for HREM in the TEM. The sample is illuminated by a parallel beam of electrons perpendicular to its surface. In the example depicted, we consider a sample with only a family of crystal planes parallel to the beam direction. The sample is thus equivalent to a diffraction grating for the beam electrons.

The beam will be diffracted by these planes in two precise direction and a part of it will not be diffracted and proceeds directly transmitted. The objective lens focalizes all the diffracted beams from each point of the sample to single points in the image plane. In this plane the diffracted beam and the directly transmitted beam are superimposed, therefore generating an interference pattern. It is important to notice that the extension of the interference area, in this ideal representation, corresponds to the whole area of the sample.

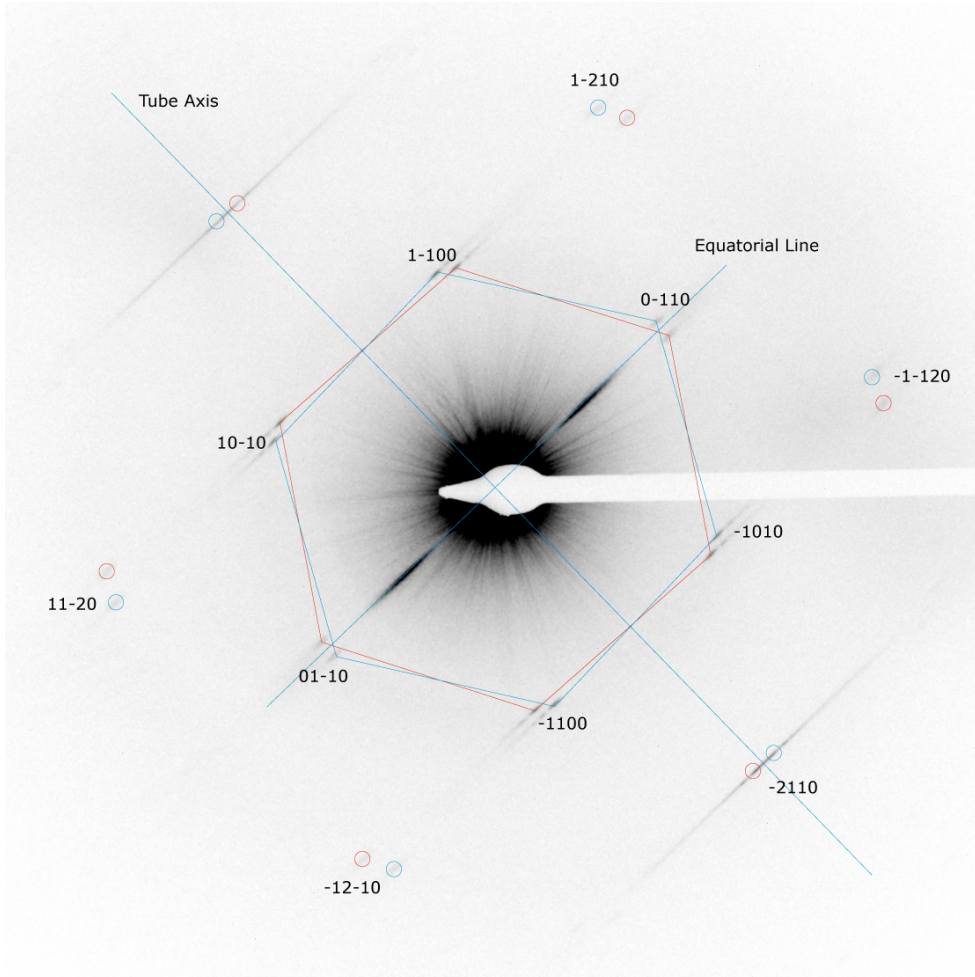


**Figure 2.18:** Experimental diffraction pattern of a (32, 29) SWCNT acquired on a CM20FEG microscope operated at 80 kV. (Intensity inverted).

In correspondence to the borders of the sample, we observe an interference pattern with fringes parallel to the arrangement of the planes in the sample. The spacing of the interference fringes, under certain conditions, corresponds to the spacing between the planes in the sample and a reliable representation of the crystal planes as a series of darker and brighter lines is realized. This is what happens in HREM mode and a higher resolution with respect to conventional imaging is achieved as single planes of the crystal are resolved. The final image of the sample shows both morphological and structural information.

The above description of an HREM image is complete only if the objective lens, and all the lenses in the microscope, are *perfect*. In reality, while from

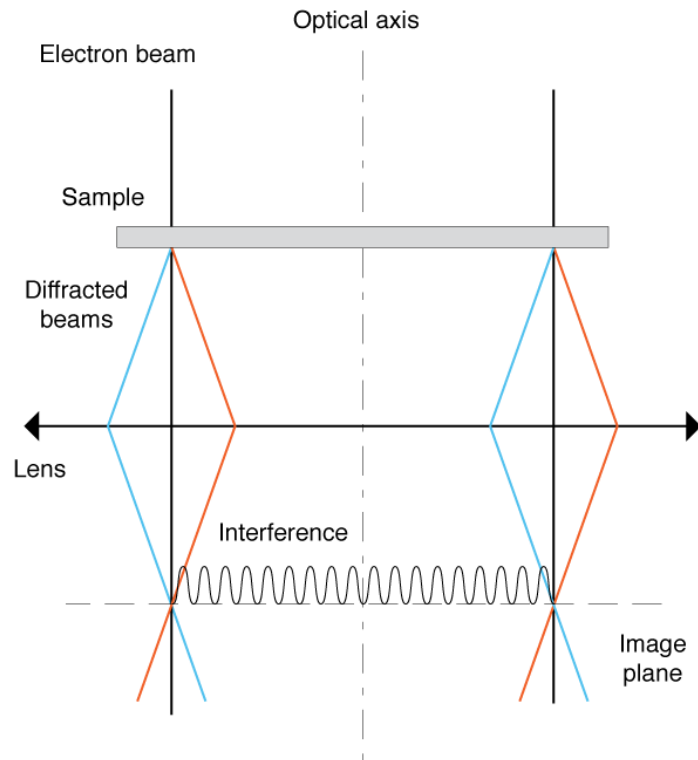


**Figure 2.19:** Simplified schematics of HREM optical set-up in a TEM. Diffracted beams by the specimen are brought to interfere on the image plane by the objective lens.

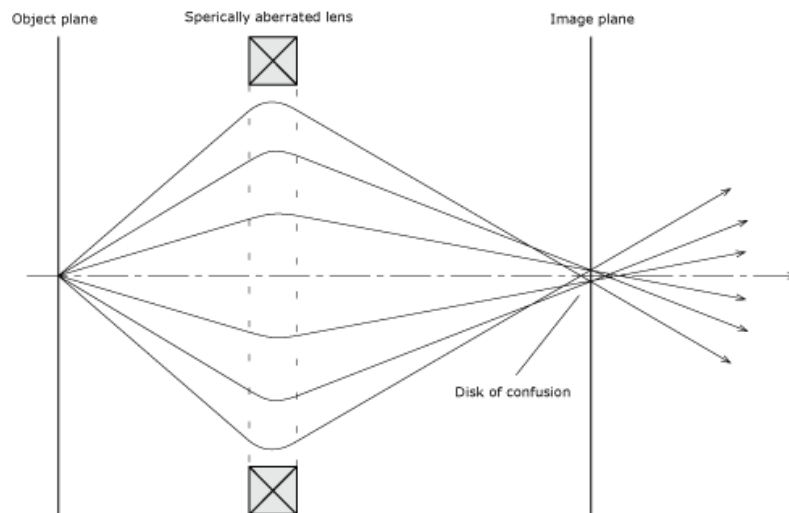


**Figure 2.20:** Schematics of magnetic lens affected by spherical aberration. Electrons entering the lens at higher angles are more strongly deflected by its magnetic field. The result is that the image of a point on the object plane is a disk on the image plane.

glass it is possible to obtain quasi-perfect optical lenses, magnetic lenses are intrinsically imperfect, or more correctly *aberrated*. The magnetic objective lens in the microscope is so aberrated that its equivalent in light optics would be the bottom of a beer glass used as objective lens.

The most important aberration in a magnetic lens is the *spherical aberration* indicated by  $C_s$ . Figure 2.20 shows a schematics explaining its effects. In a perfect lens all the electrons coming from one point of the object plane will be focalized in a single point of the image plane. By the way, the magnetic field of real lenses, is much stronger nearby the pole-pieces than around the optical axis. Electrons traveling more out-of-axis will be deflected more than that nearby the axis. For this reasons they will be focalized on different planes and the result is that a single point in the object plane is imaged as disk instead of point. If we recall the scheme of Fig. 2.19 this means that some diffracted beam at higher angles will be focalized outside the boundary of the image of the sample. The interference pattern will then be *delocalized* outside the crystal image.

There are much more aberrations in a magnetic lens. In order of decreasing effect there are: defocus  $d$ , astigmatism  $A$ , the already mentioned spherical aberration  $C_s$ , the coma  $B_2$  and many other of higher order<sup>2</sup>. Defocus and astigmatism can be corrected with specific optical elements in the microscope, so that the next most effective term is the spherical aberration.

These aberrations affects the way the microscope transfers the spatial informations from the specimen to the image. A spatial analysis of this process is more easily carried out in the reciprocal Fourier space of the spatial frequencies  $\mathbf{k}$  composing the sample. The frequency  $\mathbf{k}$  is the reciprocal of the distance vector  $\mathbf{r}$  in real space.

The effect of all aberrations combines, acting as a global frequency filter  $T(\mathbf{k})$ , modulating the intensity of the frequencies describing the object. This filter function is called the *contrast transfer function* (CTF) of the microscope. If the filter cuts all high-frequencies, all the smaller details of our sample will be eliminated from the final image. On the other side, if all low frequencies are eliminated we will lose all long-range details from the image. To obtain a representative image of our sample we would like the CTF to transfer with the same intensity all the frequency up to the highest possible ones.

Figure 2.21 shows a plot of the CTF for a FEI Tecnai F20 TEM operated at

---

<sup>2</sup>For a detailed description see [58]

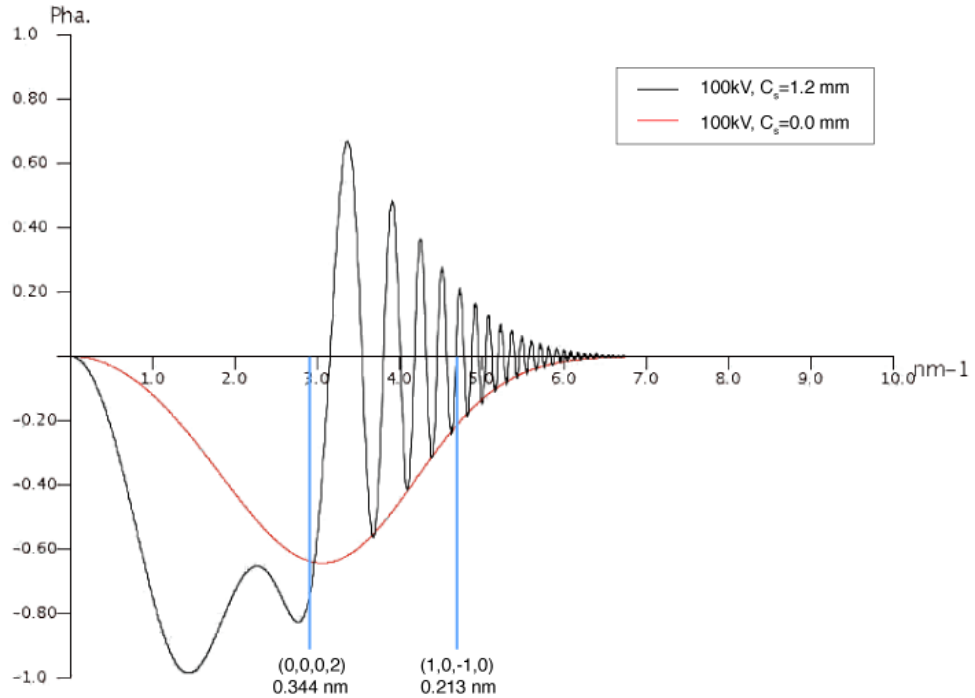


**Figure 2.21:** Plot of the CTF calculated for 100  $kV$ . the black curve is calculated for  $C_s = 1.2 \text{ mm}$ , while the pink one is for a corrected microscope where  $C_s = 0$ . Frequencies corresponding to  $(0, 0, 0, 2)$  and  $(1, 0, \bar{1}, 0)$  reflection of honeycomb lattice are indicated in the graph.

100  $kV$ . The black curve represents the CTF for a typical spherical aberration of 1.2  $\text{mm}$  affecting the objective lens of this microscope. There is significant transfer of frequencies, without contrast inversion, from 1 and 3  $\text{nm}^{-1}$ . All frequencies within this range will be transferred faithfully in the final image. Above 3  $\text{nm}^{-1}$  the CTF oscillates rapidly, indicating that some frequency won't be transferred at all, while for others the contrast will be reversed in the image. None of these higher frequencies will be transferred faithfully in the final image<sup>3</sup>.

The red curve represents the CTF for the same microscope with no spherical aberration. It is clear that now the range of frequencies transferred to the image has increased and no contrast inversion is present. Increasing the highest transferred frequency means to increase the resolving power of the microscope, because finer

<sup>3</sup>For simplicity, the graph depicted do not consider the effect of neither spatial or temporal envelope, as a detailed description of the complete imaging process is far beyond the aim of this manuscript.

details will be transferred correctly in the representation of the sample. In the last ten years the development of aberrations correctors based on multipolar optics was a real revolution in TEM. All top level commercial TEM are nowadays equipped with aberrations-correctors capable of correcting not only the spherical aberration but all aberrations up to the fifth order. New second-generations correctors are under development, with the aim to bring the TEM to the ultimate diffraction limit.

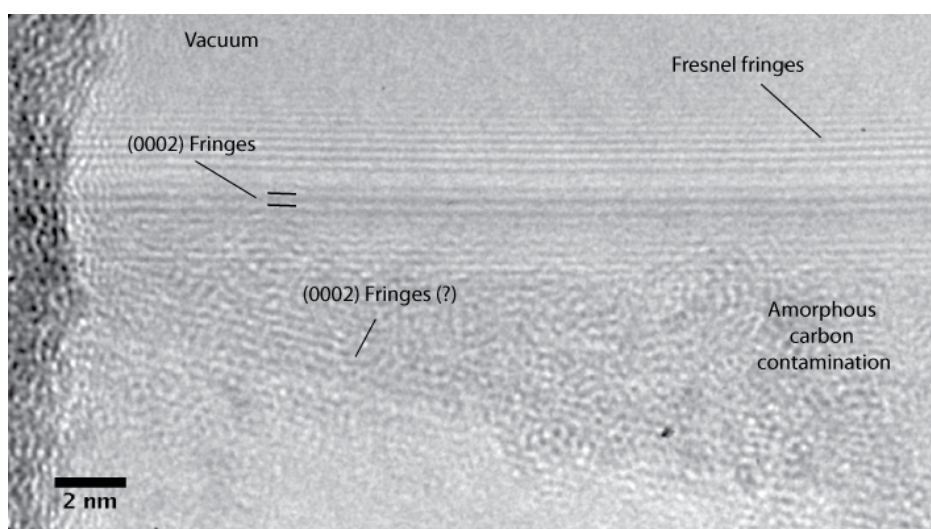


**Figure 2.22:** Aberrations affected HREM image of the folded edge of a two-layers graphite flake.

In our researches we used a FEI Tecnai F20 equipped with a first-generation aberrations-corrector from CEOS. Figure 2.22 shows the HREM image of a bi-layer graphite flake suspended over a holey-carbon film acquired in a similar Tecnai F20, operated at  $100\text{ kV}$ , but without a corrector. In the image is visible the folded border of this flake. Upon bending over itself, near the border we are looking parallel to  $(0002)$  planes of graphite, spaced by  $0.344\text{ nm}$ . The diffracted beams from these planes creates the two interference fringes visible along the border, and another few  $(0002)$  fringes are visible inside the flake as another folded border is superimposed to the underlying flake.

Fresnel diffraction from the upper border extends well in the void region near flake. Considering the CTF shown in Fig. 2.21 for the uncorrected microscope, it is immediately clear that the frequencies corresponding to the spacing of  $0.213\text{ nm}$  of the reflections of the inner hexagon of the reciprocal lattice of graphene are at the limit of the performances of the optical system. In the image of Fig. 2.22 this

periodicity is completely absent, as the slightest misalignment in the TEM make their transfer impossible. We can barely count the number of layers composing the flake - 2 in this case - from the (0002) reflections at the border, but from this image it is impossible to obtain more detailed structural information.

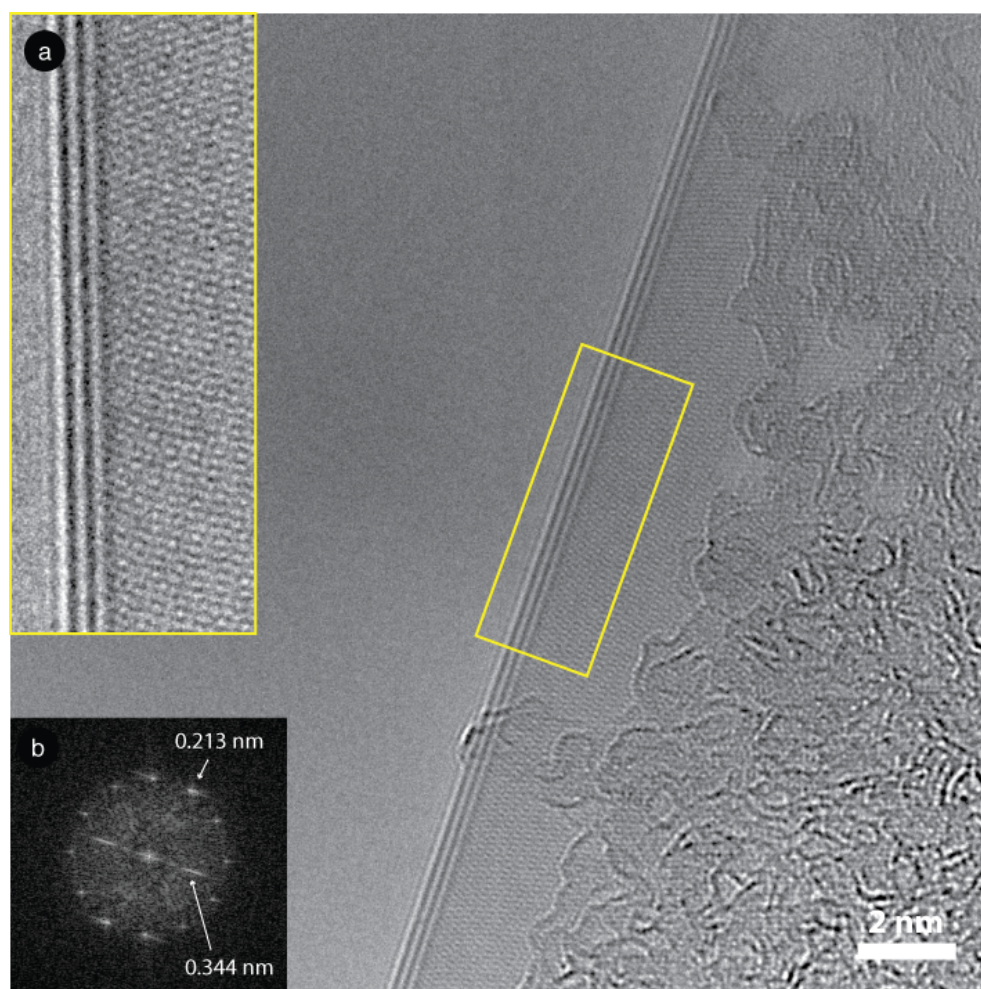


**Figure 2.23:** Image of the folded border of a three-layers graphite flake. a) Magnified image relative to the area in the yellow rectangle. b) FFT of the image, showing 0.344 *nm* and 0.213 *nm* corresponding reflections.

Figure 2.23 shows a similar graphite flake imaged at the same tension in a similar Tecnai F20 TEM, but corrected for aberrations. In the corrected image the interference fringes from (0002) graphite planes at the folded border are clearly visible. The inset a) shows a magnified view of the area in the yellow rectangle. The surface of the flake is no more featureless, instead an intricate diffraction pattern

emerges. The inset b) shows the Fourier transform of the image, displaying the intensity of the spatial frequencies composing the image. Spots corresponding to  $0.213\text{ nm}$  and  $0.344\text{ nm}$  fringe spacing are clearly visible. The 12 spots for  $0.213\text{ nm}$  corresponds to two hexagonal sets representing the diffracted beams of the two graphite sheets (each composed by 3 layers) superimposed by the folding. The aberrations-corrected image therefore provides a higher level of structural information.

### 2.3.2 Electron beam damage

In the discussion of the previous section it was pointed out that all the images were taken either at  $80\text{ kV}$  or  $100\text{ kV}$  instead of the  $200\text{ kV}$  usually the standard in TEM instruments. While scanning probe microscopies do not actually touch the sample during imaging, in TEM electrons cross the specimen at high energy and the interaction with the atoms of the sample may lead to high energy transfers from the electrons of the beam to that of the specimen producing structural modifications and damages in the sample itself. Beam damage is thus a fundamental issue of TEM.

Electron beam damage is particularly critical in investigating graphene based structures as at the typical accelerating voltage of  $200\text{ kV}$  of conventional TEM the cross-section for displacing an atom from the honeycomb lattice is quite high. The high electron dose typically needed for high-resolution imaging make the sample to loose atoms, and its structure therefore, in a matter of seconds. An effective solution is to lower the energy of the electrons of the beam.

Unfortunately variable acceleration voltage it is not a feature of all microscopes. The Tecnai F20 microscope we used to perform our experiments was equipped with an aberrations-corrector from CEOS, but the electro-optic set-up of the microscope and the corrector was originally tuned for standard  $200\text{ kV}$ . Re-calibration of all the currents of the all the multipolar optical elements of the correctors is an unimaginable work. The patience and stunning expertise of Peter Hartel from CEOS made this all possible.

Knocking an atom away from its lattice position with an electron is an elastic effect, as the electron loses part of its energy to provide kinetic energy to the nucleus. The minimum energy an electron must have to activate such a process is about  $90\text{ kV}$ . Already at  $100\text{ kV}$  the elastic cross section is low enough not to destroy lattice structure, but inelastic cross section starts to play a significant role.

The  $100\text{ kV}$ , or  $80\text{ kV}$  electrons won't knock away atoms, but they will provide energy to them, heating up the sample. Under these conditions endothermic reactions

between the carbon atoms of the graphene network and residual contaminants, like water and other hydro-carbons adsorbed over the surface, literally burns graphene and SWCNTs [59]. Adsorbed water and carbohydrates contaminating the surface of the sample will desorb under the beam and create a reactive micro-atmosphere nearby the surface.

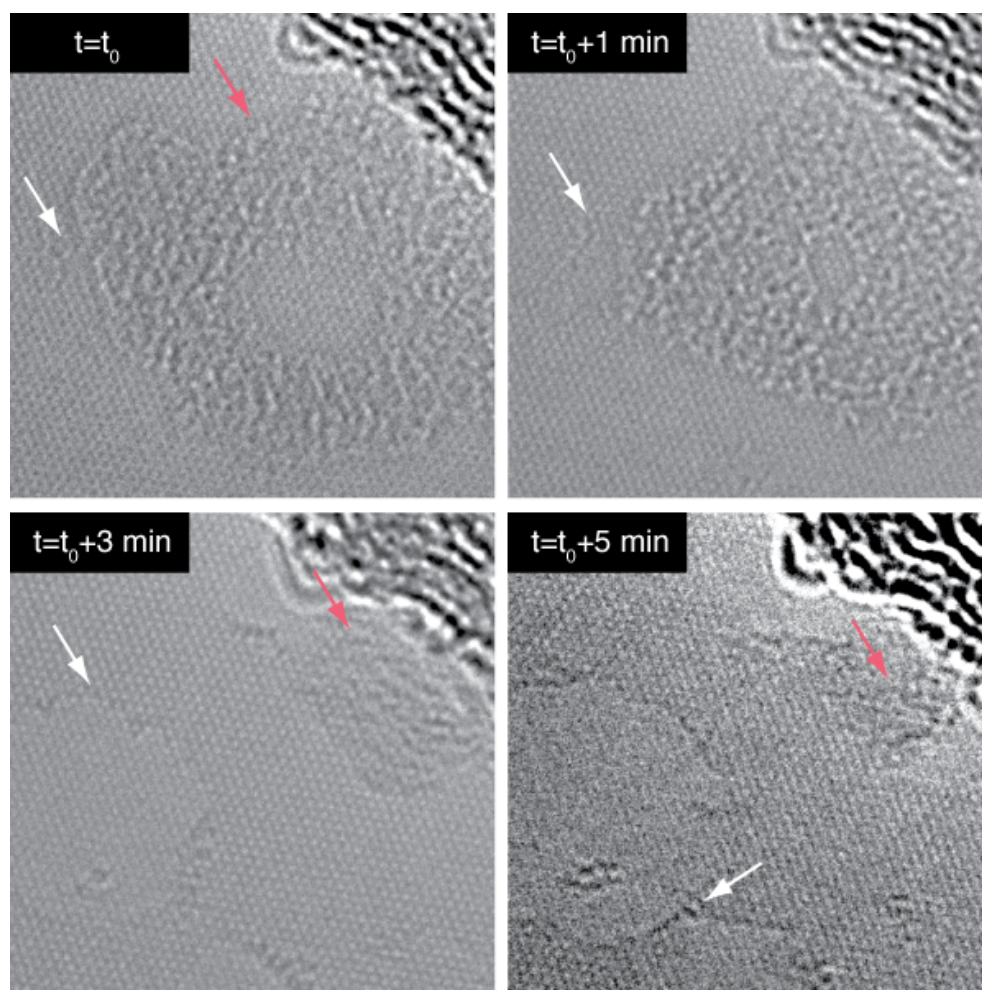


**Figure 2.24:** Temporal sequence of HREM images of the surface of a multi-layer graphite flake to investigate the effects of beam damage. Red arrows indicate the position of contaminants cluster over the surface, while white arrows indicates holes in the surface layer.

Figure 2.24 shows a time sequence of HREM images of the surface of a graphite flake. In the first image at  $t = t_0$ , the red arrow indicates a small cluster of amorphous contaminants, most likely a mixture of carbohydrates and burnt amorphous carbon. A small defective area in the graphene network is present on the side of the

contaminants cluster and it is indicated by the white arrow. The sample continued to be exposed to the electron beam during the whole time between sequential acquisitions.

In the image taken one minute after it is possible to see that the cluster of contaminants reduced its volume, probably burned under the beam. At the same time the defective area extended into a small irregular hole in the first layer of graphene. The underlying layer shows no change in the structure. In the image taken at  $t = t_0 + 3$  min the contaminants reduced to a small fraction of their original volume while the previously small hole, indicated by the white arrow expanded its perimeter releasing more carbon atoms from the peripheral region of the lattice. At  $t = t_0 + 5$  min the contaminants cluster is almost completely burned, while the hole in the layer expanded, joining another forming hole below. These observations seem to confirm that graphene damage is essentially a surface process, with layers peeling-off one after each other due to interaction with the reactive micro-atmosphere nearby the surface.

To limit this beam damage on graphene-based structures it was particularly effective to remove the surface contaminants with few seconds (less than 10) of plasma-cleaning in dedicated TEM holder plasma-cleaner. The reactive atmosphere of the plasma won't damage the graphene lattice of the flakes but will reduce degassing of the sample in the TEM, providing a cleaner micro-atmosphere around the sample. Leaving the sample inside the TEM overnight will also ensure a better imaging session the day after.

### 2.3.3 Low-voltage aberration corrected HREM experimental investigation

In the previous parts of this Section we discussed briefly the principles of HREM in the characterization of graphene membranes and SWCNTs. We are testing the ultimate performances of the microscope as we push HREM to image mono-atomic layers of carbon atoms.

Figure 2.25 shows the experimental image of a two-layer graphite membrane. The number of layer can easily be determined in this case as in the region indicated by the arrow the flake folds and (0002) fringes are clearly visible. The same way the walls of a CNT are counted by counting these fringes, here we could determine the flake to be constituted by two graphene layers stacked. The inset in the figure shows the FFT of the surface of the flake, and principal graphene reflections for a spacing of  $0.213 \text{ nm}$  are marked by blue circles. From the HREM image it is possible to

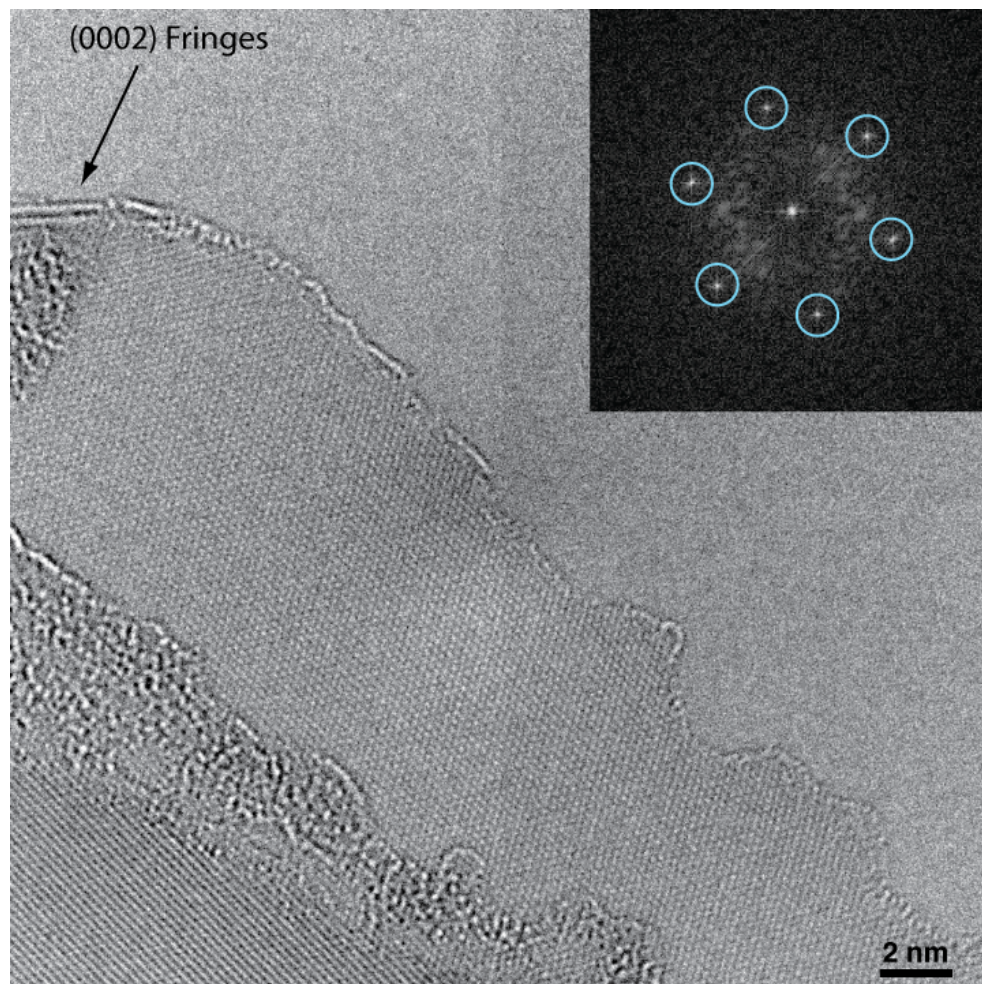


**Figure 2.25:** HREM image of a double layer graphite flake. White arrow indicates the (0002) fringes at the folded edge. Inset: FFT of the flake surface

analyze the surface of the flake searching for defects in the graphene lattice. This imaged flake is completely free from surface defects.

TEM HREM sensitivity is enough to provide images of single atomic layers, with unaltered lateral resolution. Figure 2.26 shows the border of a larger and thicker flake of mechanically exfoliated natural graphite. In the region at the center of the image just one mono-atomic layer of graphene was suspended over vacuum.

The inset shows the FFT of the flake area and the hexagonal pattern is marked by blue circles. By carefully looking at the FFT it is evident that the spots are somehow blurred and elongated. This means that different frequencies nearby the principal one corresponding to a spacing of  $0.213 \text{ nm}$  were present in the image. The interference hexagonal pattern of the flake is indeed slightly deformed and the flake is

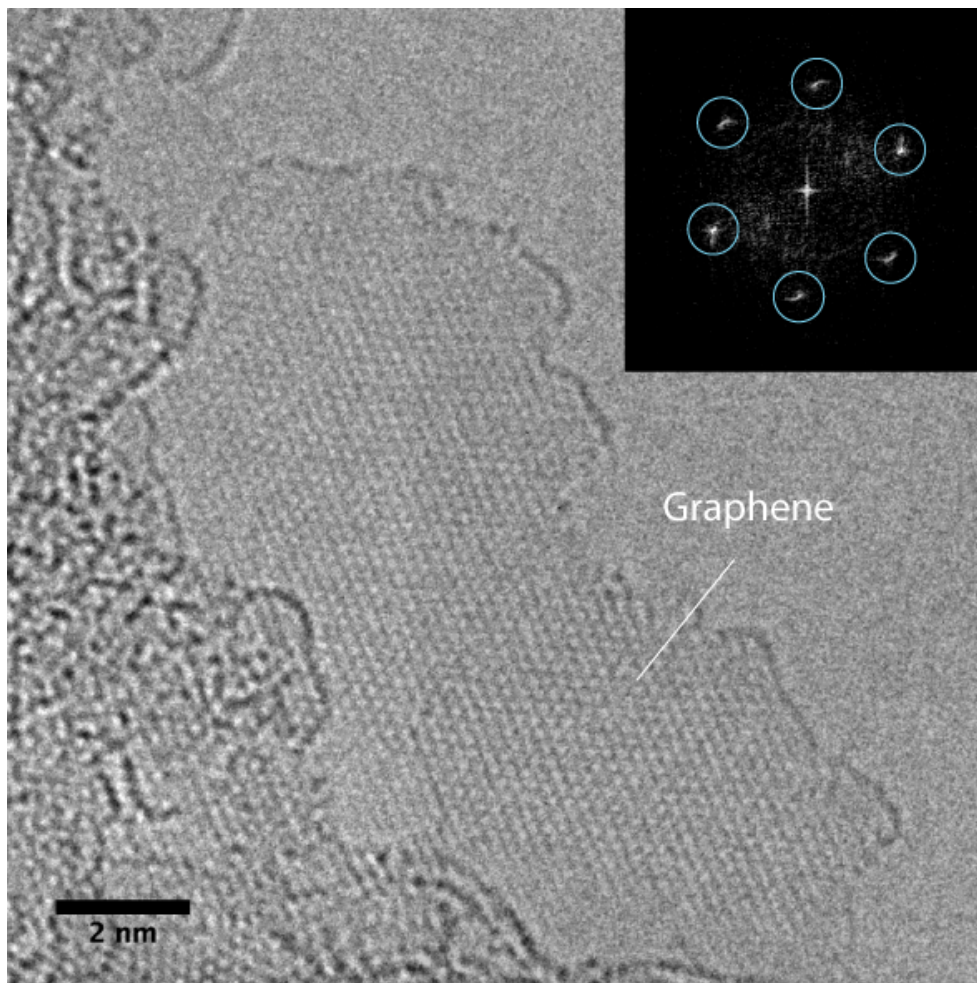


**Figure 2.26:** HREM image of a graphene flake. Inset: FFT of the flake surface

most probably deformed in three-dimensions, making some sort of undulation. Apart from this deformation effect, in this case too there is no defect in the lattice.

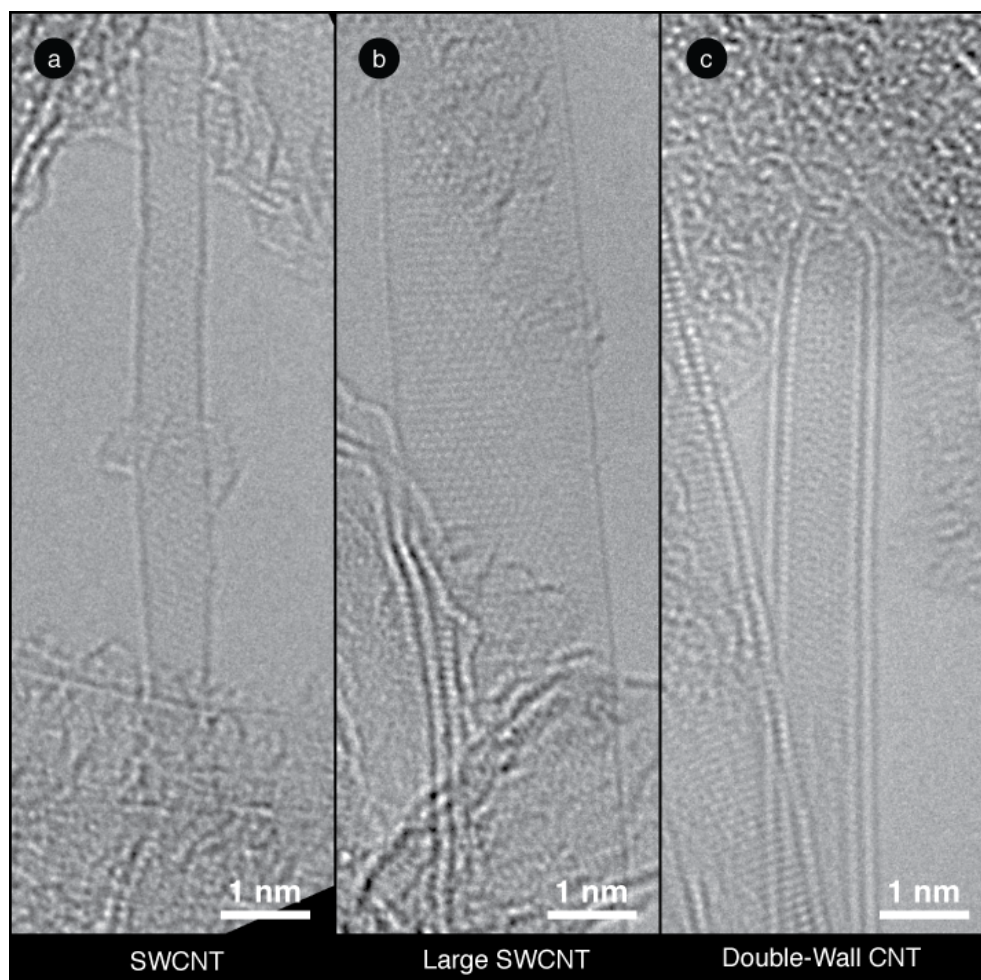


**Figure 2.27:** Collection of HREM images of CNTs. a) SWCNT. b) Extra-large SWCNT. c) Closed cap double-wall CNT.

Figure 2.27 shows some experimental results obtained with the low-voltage aberrations-corrected set-up in the characterization of CNTs. Fig. 2.27 a) shows a chiral single-walled nanotube, while b) shows a larger diameter zig-zag tube where the direct imaging of the lattice orientation of the walls allows for the direct determination of its chirality. Fig. 2.27 c) shows a double-walled nanotube. In TEM not only the outer wall of the tube is visible, but simultaneous structural information about the surface and inner wall is provided. The superposition of the four honeycomb lattice layers produces a characteristic moiré effect (the optical

interference between the period features of the two walls) on the image of the tube.

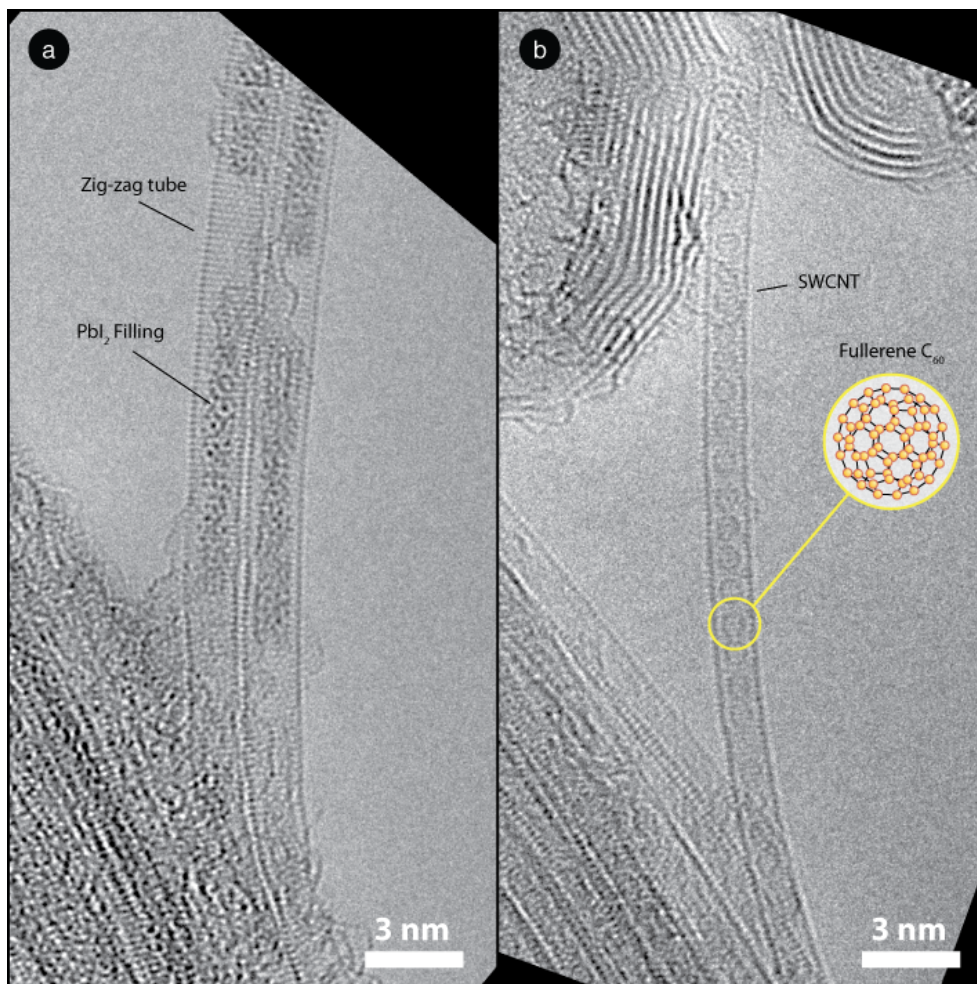


**Figure 2.28:** HREM image of filled SWCNTs. a)  $\text{PbI}_2$  filled zig-zag SWCNTs and b) fullerenes filled SWCNT (*peapod* [60]). The structure of both the tubes and of their fillings is resolved.

The possibility to investigate both the surface and the inner space of nanostructures is essential in the case of filled SWCNT. Figure 2.28 shows the example of some filled SWCNT. Fig. 2.28 a) shows two  $\text{PbI}_2$  filled SWCNT, separating from a bundle of similar tubes. Both the tubes were partially filled with  $\text{PbI}_2$  and the filling is clearly in amorphous phase. At the same time it is possible to determine directly on the image the orientation of the lattice of the two tubes which are both zig-zag. Figure 2.28 b) shows a fullerenes filled SWCNT [60]. Even in this case a comprehensive look of the inner part and of the surface of the structure is obtained in TEM. The tube result to be a zig-zag one and fullerenes structure is clearly resolved.

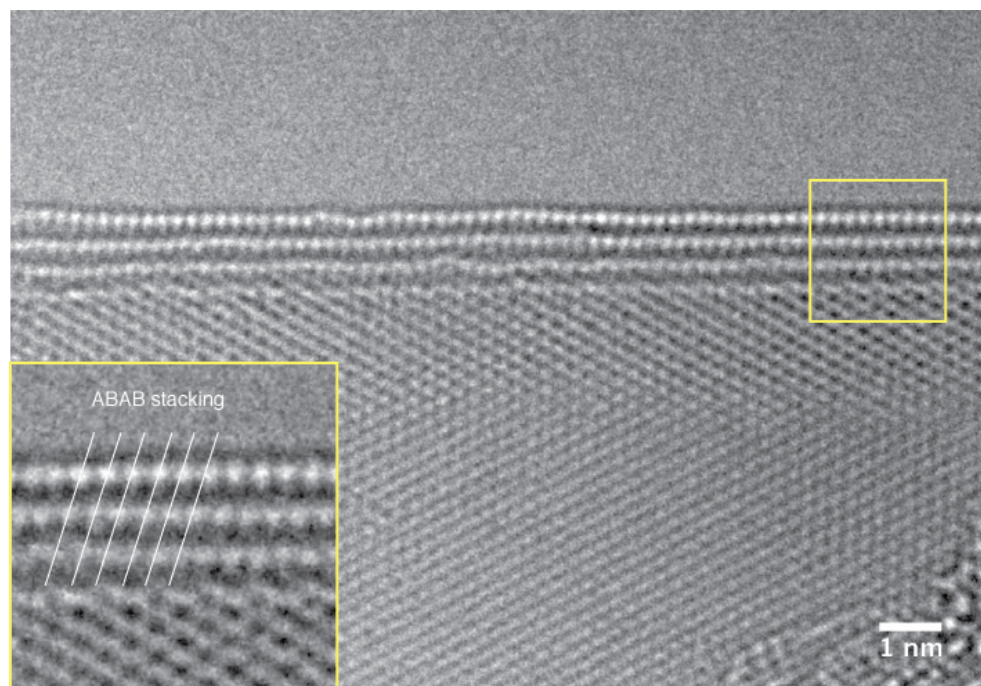


**Figure 2.29:** Image of the border of a four-layer flake. In the inset a detail of the (0002) fringes exposed where the flake folds. White lines mark the ABAB stacking orientation of the layers.

HREM investigation can provide important information about the stacking order of graphene layer in flakes as well. Figure 2.29 shows folded border of a mechanically exfoliated graphite flake. From the number of (0002) fringes at the border the number of layer composing the flake before the folding was 4. Interestingly, as opposed to the case of the flake of Fig. 2.23, here the border folds bringing the two layer of graphite to superimpose matching the honeycomb lattices in a ABAB or AA stacking order as a single hexagonal pattern is visible on its surface.

In the inset of the Figure is shown a magnified view of the region in the yellow rectangle. The alignment of the dot structures on each fringe with respect to neighbor ones can give us information about the stacking order of the graphene layers. In this flake the dots, corresponding to the center of the hole hexagon in the the honeycomb lattice, are shifted with respect to those of neighbor fringes. The dots are aligned over lines not perpendicular to the border direction. This arrangement is specific of graphene layer stacked following ABAB order. We found that most of the flakes prepared by sonication of mechanically exfoliated graphite crystals end in folded

borders following this stacking order. In natural graphite, ABAB order is the most thermodynamically preferred order but seems to be favorable for folding too.

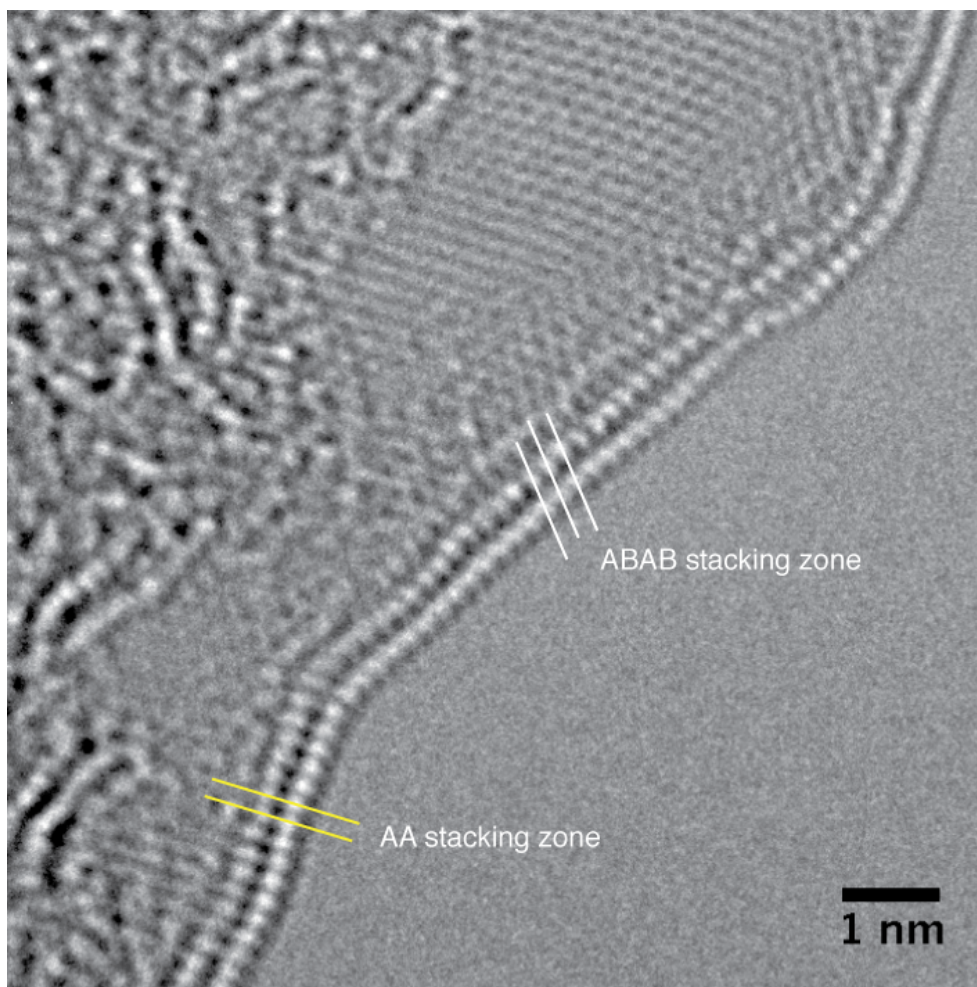


**Figure 2.30:** HREM image of a double-layer flake folded edge with mixed stacking order. Localize zones with AAA order (yellow lines) are connected to zones with ABAB order (white lines) by a bending in the border.

In some flakes some stacking order defect is associated to the local curvature of the folded border and mixed stacked area can coexist nearby. Figure 2.30 shows the image of the border of a similarly prepared thin graphite flake. In this case the flake is not folded along a straight line, but indeed it presents a bended profile. As marked by the orange lines in most of the straight areas the stacking order is confirmed to be the standard ABAB one. In the lower part of the image yellow lines indicates a localized zone of AAA stacking order. The two zones are connected by a small curve

where the interlayer distance relaxes and allows for the registration between the two zones.

## 2.4 Conclusions

In this Chapter we presented several techniques available at the TEM for the structural characterization of low-dimensional carbon allotropes like SWCNT and FGC membranes. We focused on a combination of low-voltage transmission electron diffraction and aberrations-corrected HREM investigation. The discussion has been structured as a step-by-step guide to the available methods capable of answering few fundamental questions about the structure of these materials.

In particular, electron diffraction results on graphene and FGC membranes were discussed, pointing out the capacity of this technique to determine, in a simple and immediate way, the mono-layer nature of the flake under investigation. When applied to SWCNTs, electron diffraction analysis can univocally characterize their crystal structure, determining the chiral indices  $(n, m)$  of individual structures.

Low-voltage HREM allows for the direct imaging of the morphology and the atomic structure of FGC membranes and SWCNTs, preserving the samples from the electron beam damage. The experimental results, obtained on individual graphene membranes, show how enhanced performances of aberrations-corrected microscopy enabled atomic resolution characterization of these materials.

The methods, and experimental results, presented in this Chapter are just a limited preview of the wide range of methods available in a TEM. Nonetheless they confirmed to be an extraordinary set of tools for scientists to investigate the structure of these low-dimensional materials. Many other TEM techniques are available, and among them we will focus on electron holography, allowing probing of the electronic properties of FGC and SWCNT, and geometric phase analysis of HREM images enabling the complete 3D reconstruction of flakes surface waviness. These somehow "*advanced*" TEM techniques deserve a specific description, and will be discussed in the following Chapters of this manuscript.



# **ELECTRON HOLOGRAPHY OF GRAPHENE MEMBRANES AND SWCNTs**

We might be the holographic image  
of a two-dimensional structure at the  
horizon of the universe.

*(Leonard Susskind)*

## Introduction

Electrons in the TEM are charged particles and they interact with the electric and magnetic fields present in the sample. The scattering of electrons by the charges in the atoms composing the sample is at the basis of HREM imaging and electron diffraction. In the previous Chapter we discussed the possibilities given by TEM to investigate the morphology and atomic structure of SWCNTs and FGCs. Shape, geometry, lattice orientation and other important structural informations can be obtained combining HREM imaging and electron diffraction data.

Describing HREM imaging, in analogy with light wave optics, we discussed briefly how electrons in the TEM can be described through their associated wavefunction. All the information about the electro-magnetic interaction with the sample is contained in the phase term of the electronic wavefront. In the case of SWCNTs and FGCs no intrinsic magnetic moment is present in the sample and only the electrostatic charges of the crystal lattice contributes to the electronic phase shift.

In the first Chapter of this manuscript we reviewed how the electronic properties of graphene membranes strongly depends on their crystal structure. In particular simulations predict that when these 2D crystals are bended and undulated, the redistribution of valence charges, due to the deformation of the crystal lattice, induces localized electrostatic potentials [17]. Those localized potentials should strongly affects the transport properties of graphene, acting as long-range scatterers for carriers.

Unfortunately, the shape and intensity of the electro-magnetic fields, which modulated the phase of the electronic wavefront, are not directly retrievable from the analysis of the interference pattern composing an HREM image nor from the position of the diffraction peaks in a recorded pattern. Nevertheless there is a technique in TEM which allows for the recovery of those fields. Electron holography is this experimental technique; it can recover the phase information of the electronic wavefront that interacted with the specimen in a TEM.

Through holographically reconstructed electronic phase maps, the shape and intensity of the electric and magnetic fields present in the sample can be mapped with sub-nanometric resolution. In the case of FGCs and SWCNTs, electron holography gives the possibility to probe the electronic charge configuration of the crystal lattice, mapping and measuring the actual electrostatic potential. The electronic properties of the nanostructure can therefore be investigated relative to the actual arrangement of atoms in space.

## 3.1 Electron holography

### 3.1.1 Electron waves and the missing phase

Inside the TEM the electrons are accelerated to high velocities by an electrostatic potential  $U_a$  of the order of few hundreds  $kV$ . The high velocity of electrons makes their kinetic energy comparable with their rest mass  $m_0$ , which is about  $0.5 MeV$ , and relativistic corrections must be applied. At the end of the accelerating stage electrons will have a kinetic momentum  $p$  described by the equation:

$$p = \sqrt{2em_0U_a^*} \quad (3.1)$$

where  $e$  is the electron charge and  $U_a^*$  is the accelerating potential, corrected for relativistic effects, with the form:

$$U_a^* = U_a \left( 1 + \frac{eU_a}{2m_0c^2} \right) \quad (3.2)$$

where  $c$  is the speed of light [61].

Electrons have wave properties too. A wave-function  $\psi$  is associated to each particle, with a wave-vector  $\mathbf{k}$  which is dependent on the momentum  $p$ :

$$\mathbf{k} = \frac{\sqrt{2em_0U_a^*}}{h} \mathbf{e}_p \quad (3.3)$$

where  $h$  is the Planck constant and  $\mathbf{e}_p$  is the unit vector in the direction of the momentum vector.

Accelerated electrons in the TEM could then be viewed as a wavefront of radiation. In analogy with light wave optics a complete beam/specimen description would be given by tracking the modifications of this wavefront from the gun down to the viewing screen.

A cartesian coordinates system is set, with the  $z$ -axis coincident with the optical axis of the microscope, directed from the gun to the viewing screen. In this scenario, for each  $z$ , the electron wavefront  $\psi_z$  can be written as:

$$\psi_z = a(\mathbf{r})e^{i\phi(\mathbf{r})} \quad (3.4)$$

where  $\mathbf{r}$  is a two-dimensional vector in the  $xy$ -plane at the height  $z$ . The electron wave has been written in its exponential form, with an amplitude term  $a(\mathbf{r})$ , related to the charge density at each point of the plane, and a phase term  $\phi(\mathbf{r})$  expressing local variation in the direction of the wavefront [62].

The electron wavefront illuminating the specimen will interact with the electric and magnetic fields in the specimen. In this particle description, electrons will modify their trajectories due to elastic scattering with the atoms of the samples, or they could inelastically lose energy in the collisions and eventually being absorbed by the material. All these processes, in the wave description, result in a modulation of the wavefront, both in its amplitude and phase term. After the interaction with the object the wavefront will have a different form  $\psi_{obj}$ :

$$\psi_{obj}(\mathbf{r}) = a_{obj}(\mathbf{r})e^{i\phi_{obj}(\mathbf{r})} \quad (3.5)$$

In a very simplified view we can imagine this wavefront to proceed through the microscope to the detector, where an image will form. The electron detector is a device sensitive to electric charge. Thus the intensity  $I(\mathbf{r})$  on the final image will be given by:

$$I(\mathbf{r}) \propto |\psi_{obj}(\mathbf{r})|^2 = a_{obj}^2(\mathbf{r}) \quad (3.6)$$

In conventional imaging all the information about the phase term is lost and only the amplitude term contributes to the image intensity. We could think that the precise recovery of the phase terms is not an issue. Let's consider a wave optical analogy. Three-dimensional perception of human eyes is related to resolving the different direction of the incoming radiation. This directional information is contained in the phase term of the wavefront. Figure 3.1 a) shows the schematics of a conventional optical image acquiring set-up.

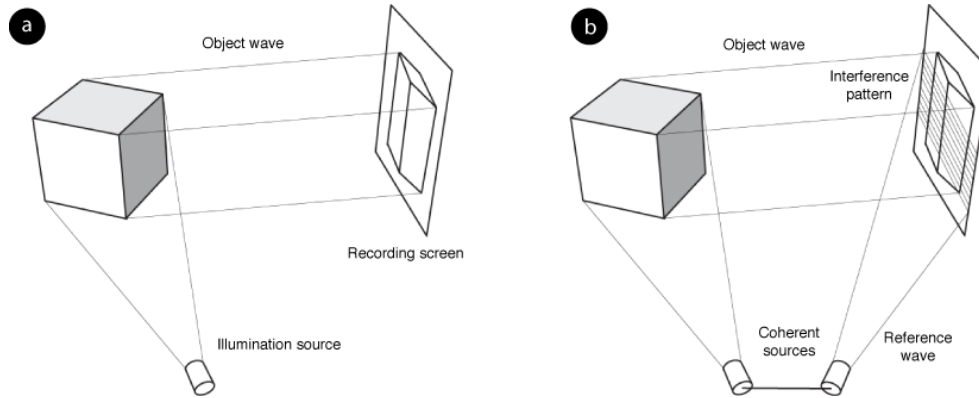


**Figure 3.1:** Conventional and holographic light recording. a) Schematics of conventional image recording in light optics. A source illuminates the object and reflected wavefront part is recorder on a light sensitive screen. b) Holographic recording schematics. A reference wave superimpose coherently to the object one and the resulting interference pattern is recorded.

A light source emits e wavefront which is subsequently reflected by the object in different directions. A screen collects part of the reflected wavefront and converts

it in an image. The resulting image is fully two-dimensional and in the final image is lost as it is only a “single-view” of the object. The case of electrons in a TEM is not different. After interaction with the sample, the electron beam is scattered and diffracted and all the information about the direction of these beams is in the phase modulation of the electronic wavefront.

The solution to the lost phase term comes from the wave nature of light and electronic radiation. Figure 3.1 b) shows a schematics of a recording set-up, where on the screen two waves converge. One is the object wave  $\psi_{obj}$  scattered by the surface of the object, and the second one directly illuminates the screen without being scattered by the object. We will call this wave the *reference wave*  $\psi_{ref}$ .

There are two ways different wavefront can superimpose: incoherently and coherently. In the former on the screen the two intensities will add resulting in a total intensity  $I(\mathbf{r})$  given by:

$$I(\mathbf{r}) \propto |\psi_{obj}(\mathbf{r})|^2 + |\psi_{ref}(\mathbf{r})|^2 = a_{obj}^2(\mathbf{r}) + a_{ref}^2(\mathbf{r}) \quad (3.7)$$

The result is the simple sum of the two separate intensities, and phase is lost.

If the two sources are coherent, the total intensity will be the intensity of the superposition of the two waves:

$$I(\mathbf{r}) \propto |\psi_{obj}(\mathbf{r}) + \psi_{ref}(\mathbf{r})|^2 = a_{obj}^2(\mathbf{r}) + a_{ref}^2(\mathbf{r}) + 2a_{obj}(\mathbf{r})a_{ref}(\mathbf{r}) \cos(\phi_{obj}(\mathbf{r}) + \phi_{ref}(\mathbf{r})) \quad (3.8)$$

On the screen will be recorded the interference pattern of the two waves, with interference fringes with a periodicity in space determined by the cosine of the sum of the two phase terms. The phase term of the object wave is then successfully recorded on the acquired image, and from the analysis of the interference pattern it can be reconstructed.

This experimental technique is called *Holography*. It exploits the interference between the object wave and a reference one, as in the above schematics, to reconstruct the full object wave, with both intensity and phase, from the analysis of the interference pattern recorded, called the *hologram*. Holography was invented in 1947 by Dennis Gabor, granting him the Nobel prize for physics in 1949 [63].

An hologram can be realized using either optical or electron radiation. Light holography is performed using lasers as coherent sources and a series of biprisms and mirrors to split and deflect beams to make the superimpose on the recording screen. Which are the electronic counterparts of optical biprisms and, moreover, what does it mean *interference of electrons waves*?

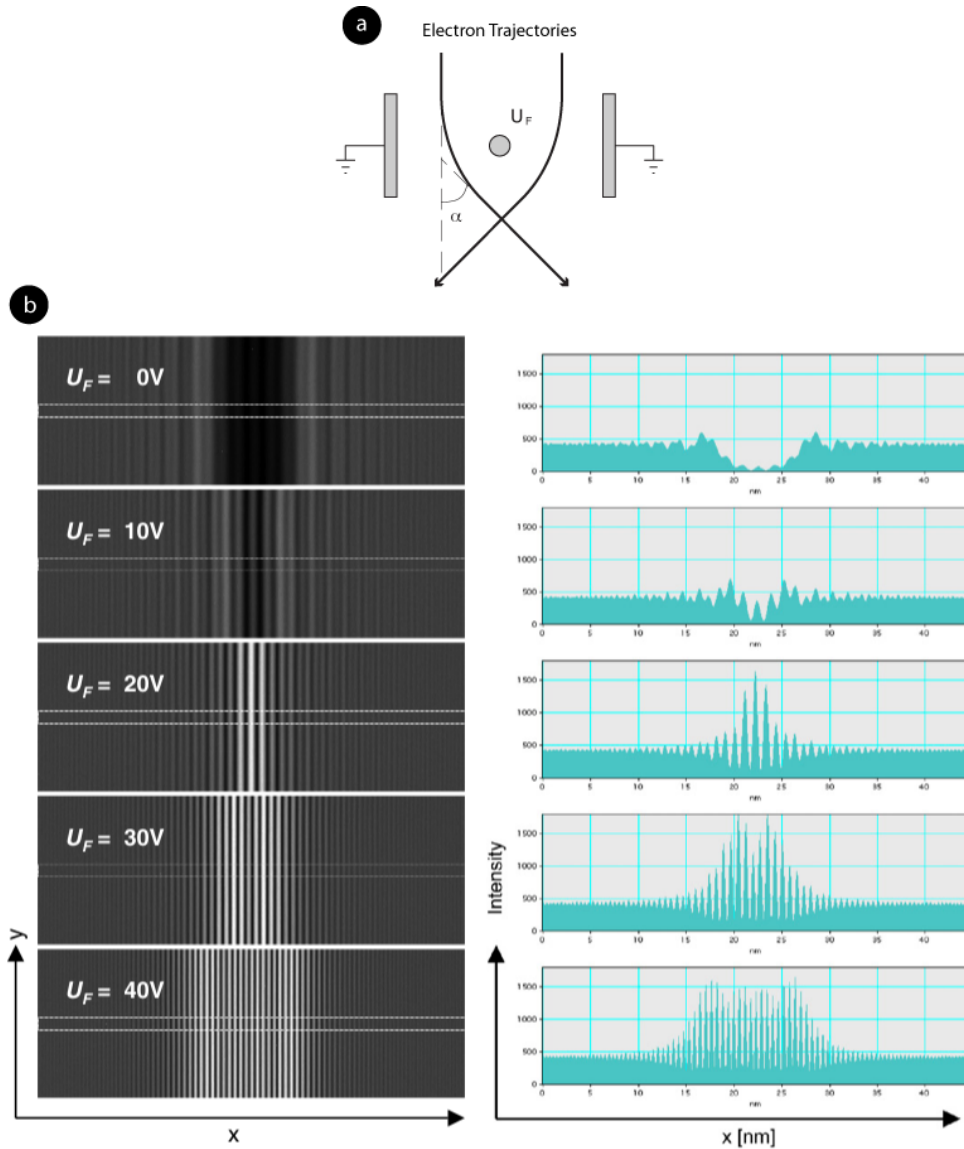


**Figure 3.2:** Making electrons interfere. a) Schematics of the electron biprism: a thin wire brought to an electrostatic voltage  $U_F$  between grounded shields. The electric field around the wire deflects incoming electrons depending on their velocity and the intensity of the generated field. b) Sequence of TEM images (left) and intensity profiles (right) for different biprism voltages. At 0 V the dark area in the center of the image is the shadow of the wire. As the wire tension is increased the electron beams superimpose coherently creating an interference pattern in the superposition area. [Adapted from [61]]

It is possible to split and deflect a beam of electrons, as in a TEM, by using a so-called *electrostatic biprism*, composed by a simple metallic wire placed on the electrons path in the TEM column and polarized to a different potential with respect to the surrounding microscope column. Figure 3.2 a) shows the schematics of the electron biprism.

The electrons pass on both sides of the wire, in a region where the applied biprism electrostatic potential  $U_F$  generates an electric field. This electric field attracts with traveling electrons deflecting their trajectory. The effect of a positive potential is to bend each side of the beam toward the optical axis, superimposing the left and the right part of the wavefront.

The effect of superposition is clear from the sequence of TEM micrograph of Figure 3.2 b) acquired at different filament voltages. At zero applied voltage the dark area in the center of the image is the shadow of the filament. As the tension increase left and right beam parts superimpose and interference fringes appear parallel to the wire edges. The spacing between the fringes is inversely proportional to the voltage applied to the filament.

But what is coherence for matter waves of electrons? Quantum mechanics affirms that two quantum states  $|\psi_1\rangle$  and  $|\psi_2\rangle$  are *coherent* only if they are the same quantum state. It is impossible even that two electrons are emitted at the same time from the electron source in the gun, clearly they won't have the same quantum state.

What interfere in the electron microscope is in fact each electron with itself. It is the single wavefunction associated to each electron that is brought to interfere with itself by the biprism. This will be clearer by looking at the time-sequence of figure 3.3.

The image shows the arrival of electrons over the detector placed after the biprism making the wavefunction interfere. TEM beam intensity was reduced to few electrons per second. In the first image we see one bright spot corresponding to a single electron hitting the detector. Nevertheless it is still one single particle hitting the detector at a specific position. As more and more electrons hit the detector the interference fringes build-up as a regular arrangement in space of single electron events [64].

Feynman considered the interference of matter waves the phenomenon containing all the mysteries of quantum theory. Nonetheless he considered the experiment of electron interference a *gedankenexperiment*: a conceptual proposal for an experiment, impossible to be actually performed. The images of Figure 3.3 state that indeed it was possible and the experiment, performed by Missiroli, Merli e

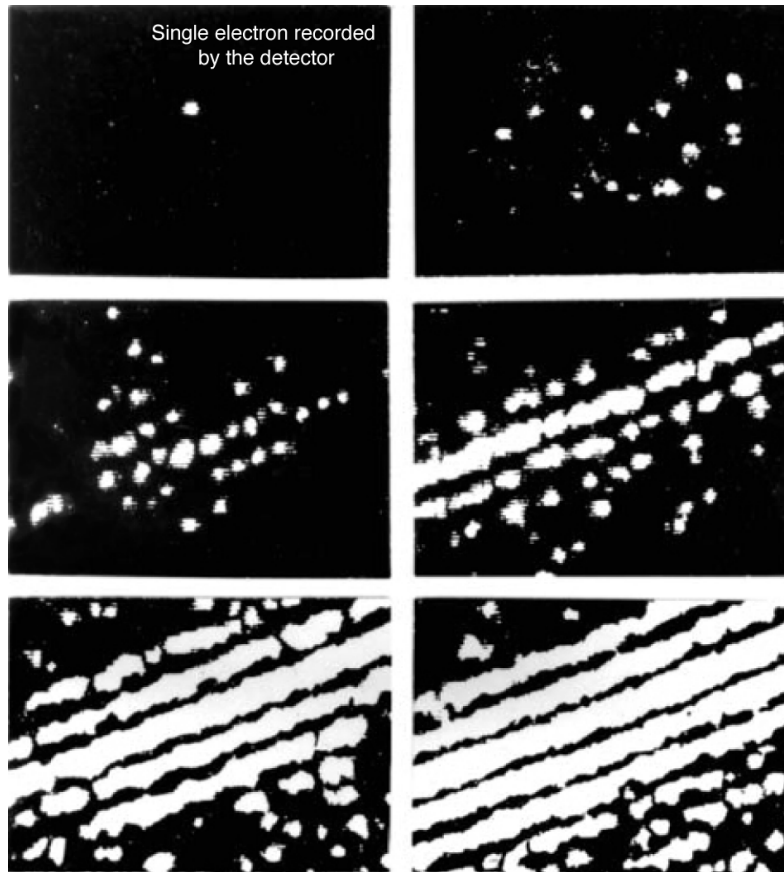


**Figure 3.3:** Build-up of interference fringes as single electron impacts on the detector. The wave-function associated to each electron is brought to interfere with itself by the biprism. [Adapted from [64]]

Pozzi in 1976 [64], was later awarded as “the most beautiful experiment of physics” by the journal *Physics World*<sup>1</sup>.

### 3.1.2 Acquisition and reconstruction of electron holograms in the TEM

Figure 3.4 shows the schematics of the holographic set-up in a TEM. Part of the electronic beam passes through the specimen, while the other part proceeds in vacuum. The wavefront part which has interacted with the specimen is commonly called the *object wave*, while the other one is known as the *reference wave*. This two waves are deflected and forced to superimpose by the presence of the biprism placed

<sup>1</sup>The text of the article can be found at the address: <http://physicsworld.com/cws/article/print/9746>

after the objective lens. On the imaging plane, the CCD records the interference pattern between the two waves.

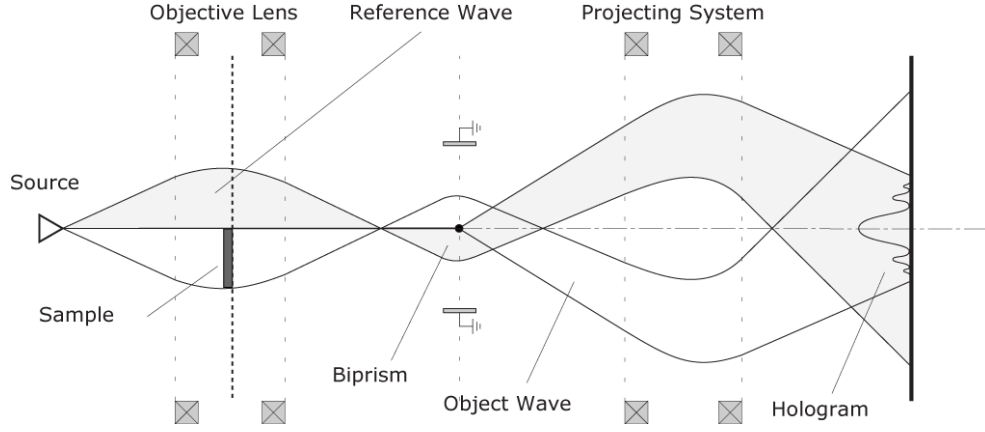


**Figure 3.4:** Schematics of the holographic set-up at the TEM. The sample is partly illuminated by the beam which will be split by the electron biprism. The part of the wavefront which has interacted with the specimen is superimposed to the one passed through the vacuum. The resulting interference pattern, the hologram, is recorded on the screen.

As we discussed previously, the information about the amplitude and phase of the object wave is encoded in the intensity and space modulation of the hologram fringes. Let's introduce some mathematical tools to access this information in the hologram. The object wave  $\psi_{obj}$ , will be modulated in its amplitude  $a_{obj}$  and its phase  $\phi_{obj}$  terms. Recalling equation (3.8), the intensity on the final image will be [65]:

$$I(\mathbf{r}) = a_{obj}^2(\mathbf{r}) + a_{ref}^2(\mathbf{r}) + 2a_{obj}(\mathbf{r})a_{ref}(\mathbf{r}) \cos\left(\phi_{obj}(\mathbf{r}) + \phi_{ref}(\mathbf{r}) + \mathbf{k}_c \cdot \mathbf{r}\right) \quad (3.9)$$

where the effect of the deflection induced by the biprism  $\mathbf{k}_c \cdot \mathbf{r}$  has been added to the phase term. The tension applied to the filament deflects the two waves, adding an additional phase term. The frequency  $\mathbf{k}_c$  is the spatial frequency of the interference fringes originated by the superimposition of the two waves, and will depend only on the filament voltage.

To simplify, without loss of generality, we can assume that the electron wavefront from the source is just a plane wavefront with uniform intensity and phase, thus the same will hold for the reference wave  $\psi_{ref}$ , since it passed nearby the specimen unaffected. In equation (3.9) we can therefore impose  $a_{ref} \equiv 1$  and  $\phi_{ref} \equiv 0$ , and

the hologram intensity is simply described by:

$$I_{holo}(\mathbf{r}) = 1 + a_{obj}^2(\mathbf{r}) + 2a_{obj}(\mathbf{r}) \cos\left(\phi_{obj}(\mathbf{r}) + \mathbf{k}_c \cdot \mathbf{r}\right) \quad (3.10)$$

The amplitude and phase term of the object wave are hidden inside the cosinusoidal intensity variations of the hologram. These informations can be recovered by analysis of the image in the frequencies domain, i.e. by analyzing its Fourier coefficients. If we apply a Fourier transform  $\mathcal{F}$  over the hologram intensity we obtain [66]:

$$\begin{aligned} \mathcal{F}\left(I_{holo}(\mathbf{r})\right) &= \mathcal{F}\left(1 + a_{obj}^2(\mathbf{r})\right) + \\ &+ \delta(\mathbf{k} - \mathbf{k}_c) \otimes \mathcal{F}\left(a_{obj}(\mathbf{r})e^{i\phi_{obj}(\mathbf{r})}\right) + \\ &+ \delta(\mathbf{k} + \mathbf{k}_c) \otimes \mathcal{F}\left(a_{obj}(\mathbf{r})e^{-i\phi_{obj}(\mathbf{r})}\right) \end{aligned} \quad (3.11)$$

where  $\delta$  is the Dirac delta function. In the frequencies space the information about the object wave  $\psi_{obj}$  is spatially separated and centered around the points corresponding to the carrier frequency  $\mathbf{k}_c$ . Since the hologram is recorded as a digital image, it is easy to calculate its frequencies spectrum by using Fast Fourier Transform algorithms (FFT). In this case all the information about the object wavefront will be in the complex valued pixels regions, called *sidebands*, around the points  $\mathbf{k}_c$  corresponding to the carrier frequency. It is easy to isolate the wavefunction contribution by means of a mask, paying attention that the regions corresponding to the carrier frequency  $\mathbf{k}_c$  are well separated from the central part of the FFT. Returning to equation (3.11) we can select one of the the two components and transform back to real space:

$$\mathcal{F}^{-1}\left[\delta(\mathbf{k} - \mathbf{k}_c) \otimes \mathcal{F}\left(a_{obj}(\mathbf{r})e^{i\phi_{obj}(\mathbf{r})}\right)\right] = a_{obj}(\mathbf{r})e^{i\phi_{obj}(\mathbf{r})} \quad (3.12)$$

With an analogous but inverse FFT, we obtain an image of complex pixels with the real and imaginary part of  $\psi_{obj}(\mathbf{r})$ .

Figure 3.5 shows a schematic representation of the reconstruction algorithm. The digital hologram is Fourier transformed to its frequencies spectrum. In the spectrum the three terms of Eq. (3.11) are clearly visible. The two regions around the brighter spots aligned in the direction perpendicular to the real space interference fringes are the group of pixels where the information of the object wavefront is stored.

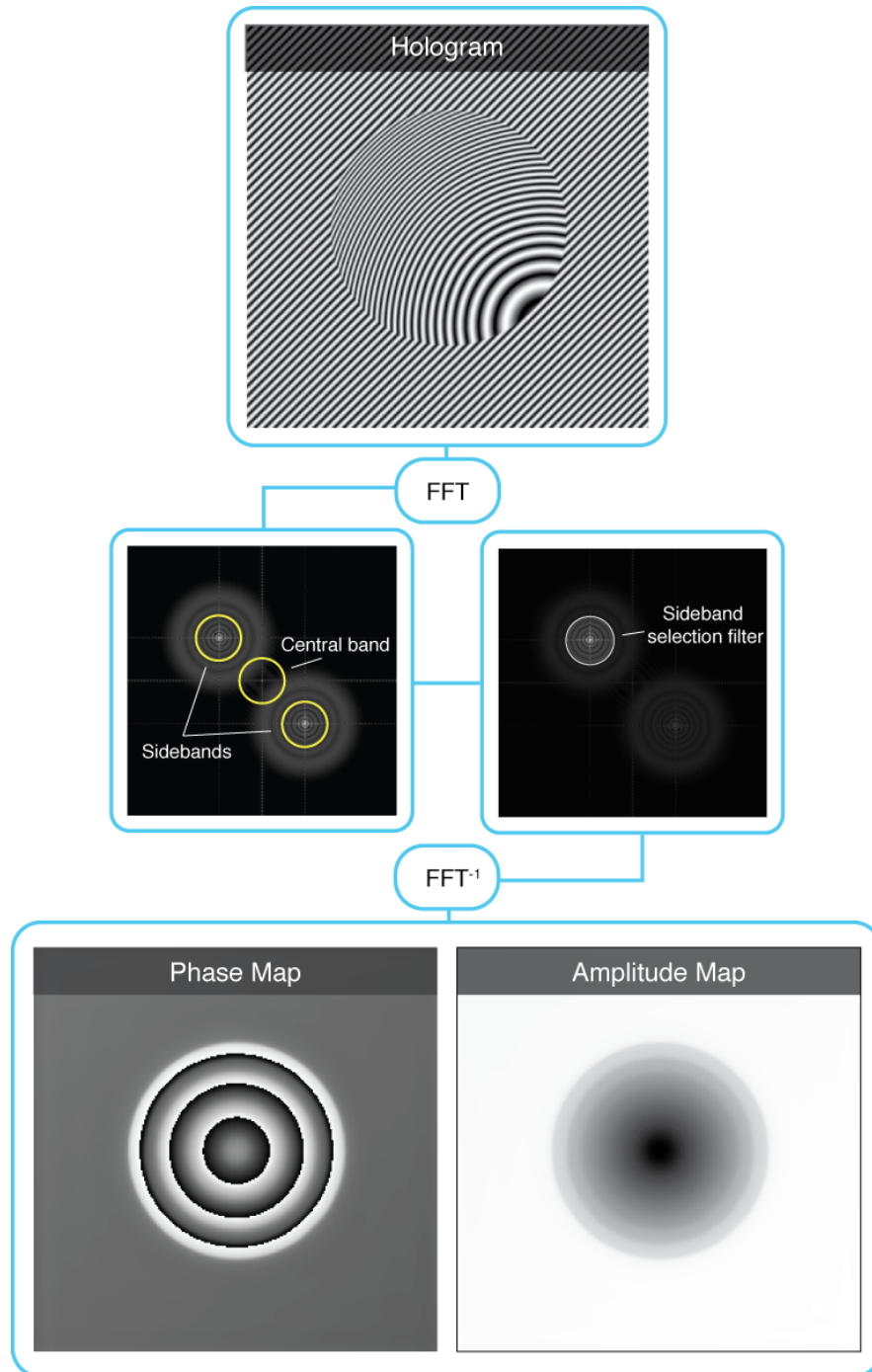


**Figure 3.5:** Schematics of the digital reconstruction of holograms. The hologram is Fourier-transformed to the spatial frequencies spectrum. The spectrum is masked out except for one of the two sideband selected. The inverse transform of the sideband is a complex image, made of real and imaginary parts. Using these two components, amplitude and phase component are calculated.

These pixels are selected by means of a mask and only them are inverse transformed back. The result is a complex image of real  $R(n)$  and complex  $C(n)$  pixels, with  $n$  an integer index indicizing the pixels. From these pixels arrays it is possible to calculate the amplitude  $a_{obj}(n) = \sqrt{R^2(n) + C^2(n)}$  and the phase  $\phi_{obj}(n) = \tan^{-1} (C(n)/R(n))$ .

The phase map values are mapped between the interval  $[-\pi, \pi]$ , thus originating discontinuities called *phase wrapping*, when their values are bigger than this interval. These discontinuities can lead to misinterpretation of the phase profiles of the sample and should be removed by specific numerical algorithms.

### 3.1.3 Phase and nanoscopic electromagnetic fields

From a microscopical point of view in the TEM we deal with just an arrangement of charges, electrons and protons, composing the atoms of the sample. The spatial arrangement of these charges distribution originates a distribution of electric  $V$  and magnetic  $\mathbf{A}$  fields in the region of the specimen. The beam electrons interacts, as charged particles, with these fields.

The effect on the wave function, as we previously introduced is a modulation in amplitude and phase of the wavefront. It is possible to calculate the phase difference  $\Delta\phi$  between electron wavefunction, before and after the interaction of the specimen, as [65]:

$$\Delta\phi(\mathbf{r}) = \frac{\pi}{\lambda U_a^*} \frac{m^*}{m_0} \int_{l(z)} V(\mathbf{r}, z) ds(z) - \frac{e}{\hbar} \int_{l(z)} A_z(\mathbf{r}, z) ds(z) \quad (3.13)$$

where  $\lambda$  is the relativistically corrected electron wavelength,  $m^*$  is the relativistic electron mass,  $V$  is the three-dimensional electric field present in the sample and  $A_z$  is the  $z$  component of the magnetic vector  $\mathbf{A}$ . The integrals are calculated over the real electron trajectory  $l(z)$  inside the sample.

It is now evident that all the information about the electric and magnetic fields in the sample is contained in the phase term. The electric field  $V$  and the magnetic vector  $\mathbf{A}$  are comprehensive of all the contributions in the sample. Within this framework electron holography gives the possibility to map these fields with resolutions of the order of  $0.1 \text{ nm}$  and in a truly quantitative way. Atomic electrostatic charges, atomic magnetic moments, dopant induced potentials and current induced magnetic fields can all be directly measured from the recovered phase maps.

## 3.2 Experimental results

### 3.2.1 Holography of carbon-based materials

Electron holography of monoatomic thick lattices of SWCNTs and graphene flakes has some important constraints and technical limitations which must be overcome to successfully reconstruct usable phase maps. The phase displacement due to a monoatomic lattice layer is nearby the limit of detection of current TEMs.

As we discussed in the previous Section, with the approximation of no inelastic scattering, each electron emitted from the source will interfere with itself by the biprism. Electrons are emitted by the source with a beam current of several  $nA$ , thus one would expect strongly contrasted interference fringes on the screen for relatively fast acquisition times. Unfortunately this is not true. Each electron is perfectly coherent with itself, but the beam in a TEM is composed of multiple electrons and the final interference pattern must be considered statistically. It is thus more correct to consider the beam to be *partially coherent*. The electron source has a finite dimension from which the electrons are emitted. Each emission is completely incoherent and uncorrelated with other emission from either the same point or other positions of the source.

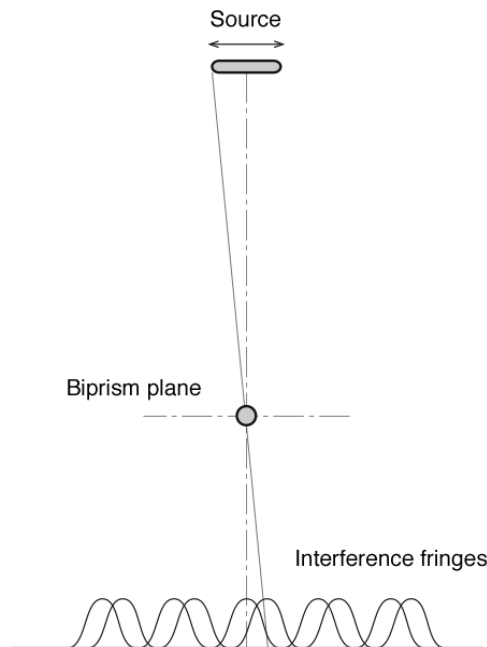


**Figure 3.6:** Effect on the interference fringes of the spatial extension of the electron source. Electrons emitted from different points of the source will be deflected differently by the biprism and will generate interference patterns in different positions.

Figure 3.6 shows the effect of the emission of electrons from different points of the source on the interference fringes. All the electrons emitted by the same location of the gun filament tip will produce an identical interference pattern. Electrons emitted from other points will leave the source with a different angle, and will reach the screen producing an interference pattern slightly shifted from the other ones. The net effect is a blurring of the interference fringes, with a significant reduction of their contrast  $\mu$ , defined as [62]:

$$\mu = \frac{I_{max} - I_{min}}{I_{max} + I_{min}} \quad (3.14)$$

Holographic reconstruction is based on the Fourier analysis of the spatial frequency of the interference image and the limited contrast of the fringes ends up in significant noise of the final amplitude and phase maps. The final resolution on the phase image  $\delta\phi$  is inversely proportional to the average number  $N$  of electrons per pixel [62]:

$$\delta\phi \propto \frac{1}{\sqrt{N}} \quad (3.15)$$

The only solution is to increase the dose of electrons per pixel on the CCD, to reduce  $\delta\phi$ , therefore increasing beam intensity or exposing the CCD for longer times.

In Chapter 2 we discussed the problem of beam damage to the lattice structure of low-dimensional carbon based materials like SWCNT and graphene flakes. As we noticed reducing beam energy from standard 200 *kV* to 100 or even 80 *kV* drastically reduces the cross-section for elastic knock-on events, but, at the same time, increases the cross-section of inelastic scattering. Electrons have more probability to transfer energy to crystal lattice, heating it up. Thermal vibration, and energy activated chemical reactions with water molecules adsorbed on the surface of the structure eventually burn the sample at higher electron doses [59].

A compromise has to be found between the instability of the sample under irradiation and the high doses needed to have sufficient signal in the hologram. This Chapter presents a collection of holograms of SWCNTs and FGCs acquired with an exposure time of 3 seconds, which resulted to be enough to have sufficient contrast on the interference fringes and short enough to induce an acceptable damage to the sample.

Figure 3.7 shows a typical hologram acquired at an accelerating voltage of 100 *kV*, with a biprism tension of 160 *V* and an exposure time of 3 sec, using a Tecnai F20 with aberrations corrector. In the inset is shown the intensity profile of the area marked by the yellow rectangle in the hologram. Fringe spacing is about 0.1 *nm*, while the final contrast is around 58%. With this experimental set-up phase resolution better than 0.025 *rad* at a lateral resolution of 0.5 *nm* can be achieved.

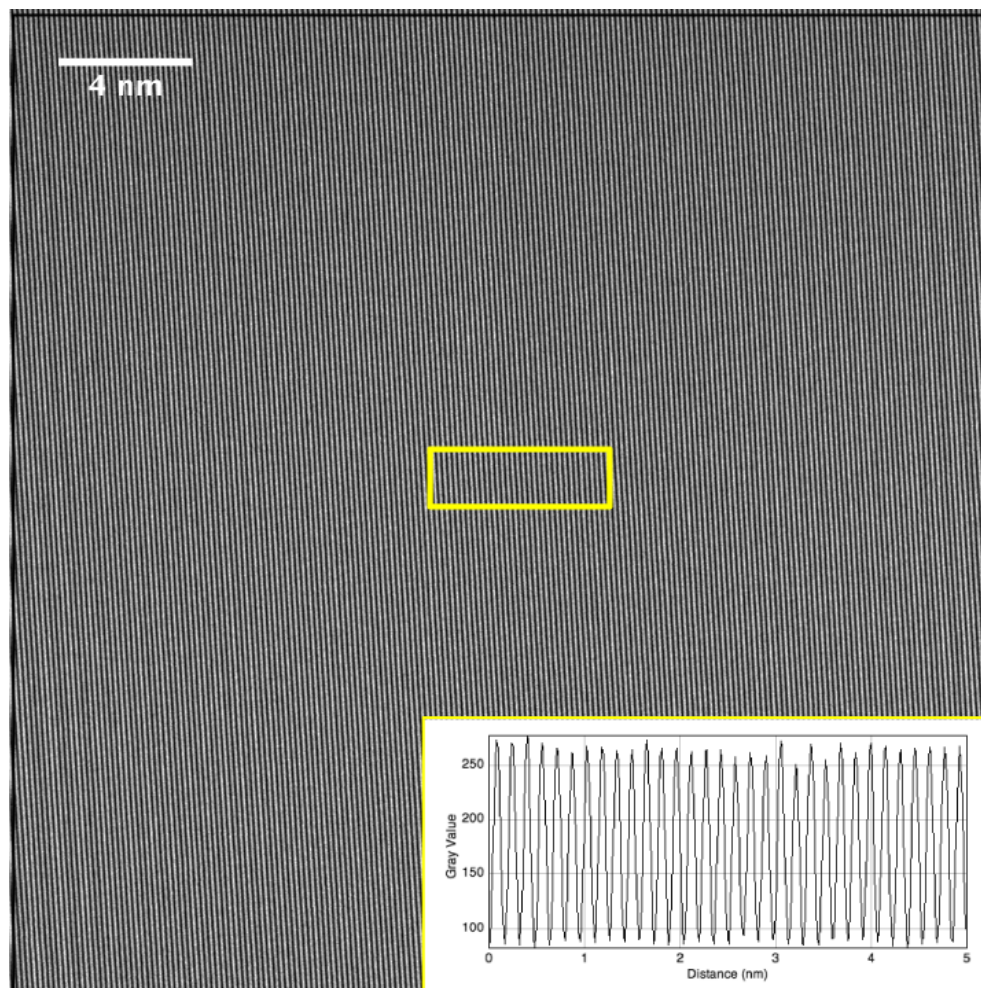


**Figure 3.7:** Hologram taken in the vacuum, acquired at an accelerating voltage of  $100\text{ kV}$ , with a biprism tension of  $160\text{ V}$  and an exposure time of  $3\text{ sec}$ , using a Tecnai F20 with aberrations corrector. In the inset is shown the intensity profile of the area marked by the yellow rectangle in the hologram. Fringe spacing is about  $0.15\text{ nm}$ , while the final contrast is around  $58\%$ .

### 3.2.2 Electron holography of SWCNTs

SWCNT grown by arc-discharge method were purified in HCl to remove residual catalyst metal particles and then dispersed in isopropanol. TEM samples have been prepared by drop-casting these solutions over a standard holey carbon film. The result is a dispersion of bundles of tubes, however few individual tubes suspended across bundles were not difficult to find.

Figure 3.8 a) show the TEM micrograph of two SWCNT bridging between two larger bundles of tubes. The tubes are covered with impurities, mainly amorphous

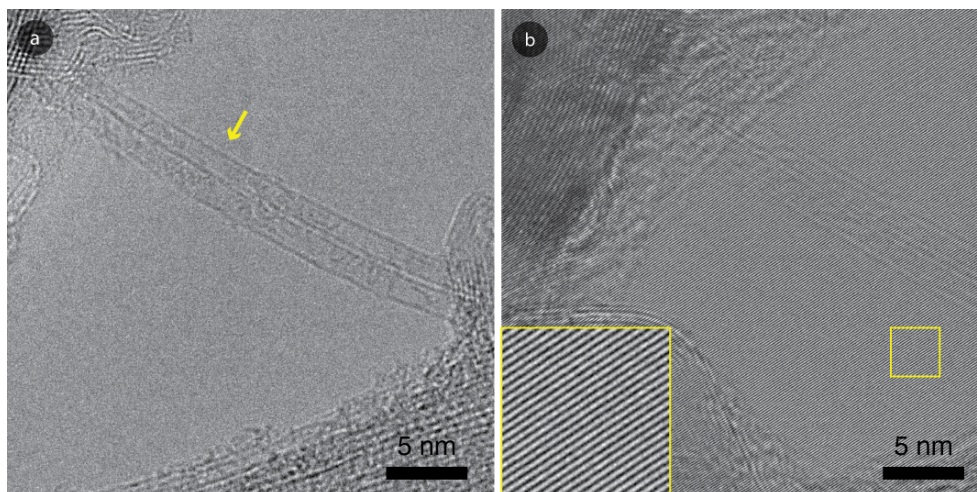


**Figure 3.8:** a) TEM image of two bundled SWCNT bridging over vacuum. b) Hologram of the region. In the inset a close-up of the indicated area of the interference fringes. (inset) close-up of the interference fringes area as indicated by the yellow square

carbon. The yellow arrow indicate a region of the upper tube which is almost completely free from any contaminants. Since our goal was to probe the electrostatic charge distribution of the honeycomb lattice we concentrated our analysis in regions like that, where only the carbon lattice is present. Figure 3.8 b) shows the hologram of the two tubes in a). The deflection effect of the biprism is clearly noticeable as the upper left part of the two tubes has been superimposed with a nearby region of amorphous carbon. In the inset is shown a higher-magnification detail of the interference fringes in the region marked by the yellow rectangle.

Holographic reconstruction was performed using a mask in Fourier space of 105 pixels in radius, corresponding to a final reconstruction lateral resolution of 0.28 nm. As an additional step in the reconstruction process a *reference hologram* has been taken. The reference hologram is just an hologram taken in vacuum. Under this condition, both object and reference wave did not pass through the specimen but were only influenced by the magnetic field of all the lenses of the microscope.

The reference hologram is reconstructed with the same parameters as the normal hologram, resulting in a phase and an amplitude map of the interactions with the magnetic fields of the microscope lenses. These fields are always present and, provided the reference is taken shortly after the hologram, it is reasonable to assume they are in the same configuration as the in the object hologram. The phase of the object is then calculated and the phase of vacuum, from the reference hologram,

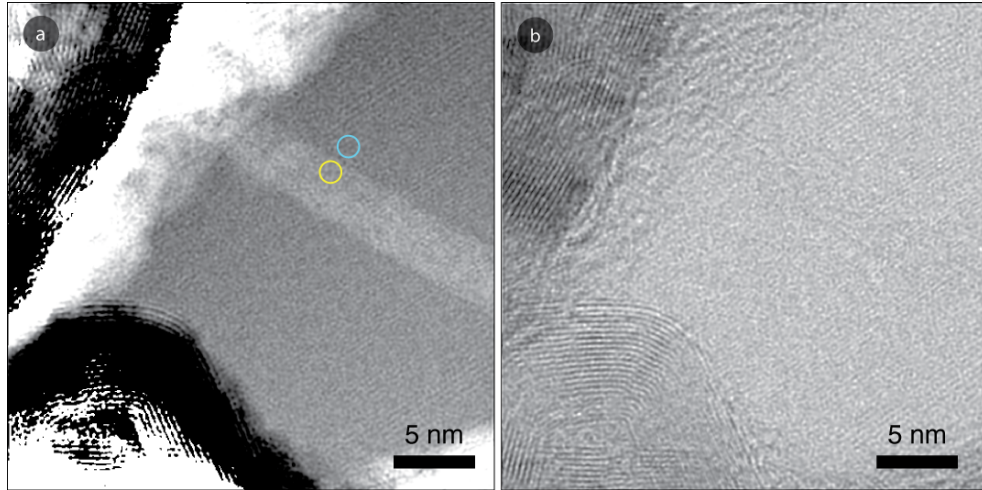


**Figure 3.9:** Reconstructed phase (a) and amplitude (b) maps for the hologram in Fig. 3.8.

is subtracted to eliminate all artifacts. This procedure has been used in all the holographic measurements here presented and is always strongly recommended.

Figure 3.9 shows the result of the reconstruction. Fig. 3.9 a) shows the reconstructed phase map, while b) the amplitude map. At a first glance it is clear that the two tubes are clearly visible in the phase image, instead in the amplitude image only few hints about their borders are visible. Reconstructed amplitude has a very low signal mainly due to the reduced electron dose used during the acquisition. On the other side, phase signal is much more stronger, even at the low doses used. Precise electron dose measurement was not possible, however, in the case of those images, we can estimate it to be of the order of  $\approx 10 e/pixel$ .

Phase resolution can be estimated by analyzing the intensity variation in vacuum, and resulted to be  $\approx 0.05 rad$ . The phase displacement due to the two graphene layer traversed by the beam electrons crossing the upper tube was measured in the area marked by the yellow circle, with reference to the value of vacuum in blue area. The phase displacement has been estimated in  $0.16 rad$ , thus each monoatomic layer contributes with a phase displacement of about  $0.08 rad$ .

The measured phase displacement in this case is not so precise, due to the limited phase resolution and to the presence of an electric stray field in vacuum near the tube. The effect is barely noticeable as a darkening of the phase in vacuum nearby the upper left border. This stray field is probably due to the massive amorphous layer charging under the beam. The effect of locally accumulated charges is much more evident in Figure 3.10.

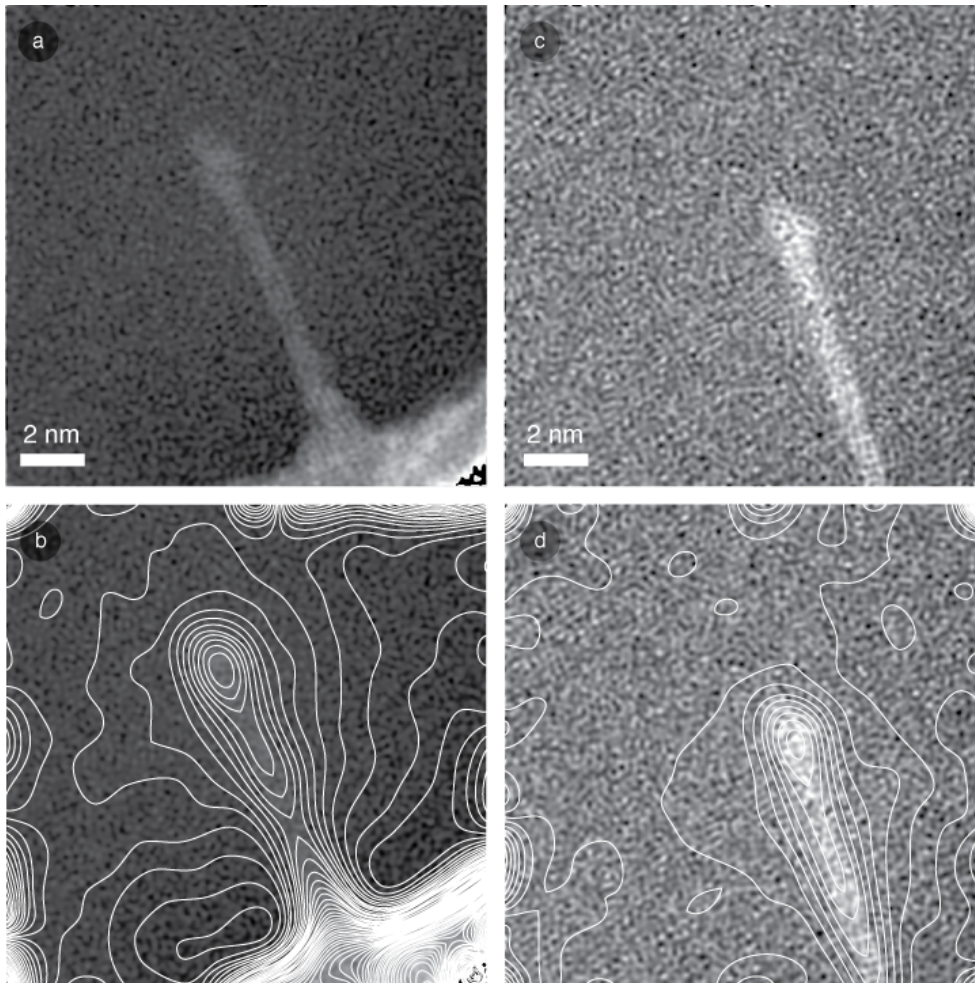


**Figure 3.10:** Mapping strain electric fields in charged SWCNTs. a) Phase map of a SWCNT near its tip. b) Contours plot of the amplified phase. Each contour line corresponds to  $1.7 \text{ Vnm}$ . c) Phase map of the same region after about 30 sec. d) Contours plot of the amplified phase, each corresponding to  $1.7 \text{ Vnm}$ . The electric field nearby the tip is reduced by about 30%.

Fig. 3.10 a) shows the reconstructed phase map of the tip of a suspended SWCNT. Fig. 3.10 b) shows the contour plot of the phase amplified 200 times, superimposed to the original phase map. Each contour line represents an equipotential line of  $1.7 \text{ Vnm}$  of the projected electrostatic potential present around the tube. Some contaminants are present over the tip of the tube and these are more likely to charge locally under the beam accumulating negative charges on the tip of the tube connected to the conductive amorphous carbon film in the lower right corner.

Fig. 3.10 c) shows the reconstructed phase map of the same area taken about 30 *sec* later. Again the stray electric field can be visualized by plotting the contours of the amplified phase as shown in d). After 30 seconds the charge over the tip is reduced by roughly one third, most probably charges have been evacuated through the tube to the amorphous carbon layer, electrically connected with the microscope ground tension.

To obtain a reliable measurement of the phase displacement induced by the two walls of the tubes, charged region like the ones previously describe were avoided, and the phase shift has been measured over contaminants-free portions of the tubes. Figure 3.11 shows the phase map of one of these tubes. The final lateral resolution in the reconstructed image is  $0.2 \text{ nm}$ , while the phase resolution has been estimated to be  $0.04 \text{ rad}$ .

In the inset of Fig. 3.11 is shown the phase profile along the area marked by the yellow rectangle. In the profile the red curve represents the fitted profile for phase displacement from the nanotube. The diameter of the tube resulted to  $1.4 \text{ nm}$ , while the phase displacement was estimated to be  $0.14 \text{ rad}$ . Thus, for the case of a tube of radius  $R = (0.7 \pm 0.2) \text{ nm}$ , each graphene wall induces a phase displacement  $\Delta\phi = (0.07 \pm 0.02) \text{ rad}$ .

### 3.2.3 Electron holography of graphene membranes

Graphene membranes were produced following Coleman's procedure of sonication assisted exfoliation in NMP [39], as previously discussed in Chap. 1. Figure 3.12 a) shows the HREM image of the border of one of these flakes. The inset b) shows the FFT of the whole image, where two graphite hexagonal reflections sets were highlighted by red and yellow circles. The two lattice structure superimposed generates a moiré effect which is clearly visible in the magnified area of inset c). The flake surface is not completely homogeneous and locally only one of the two lattices is present. The inset d) shows the FFT of one of these single-lattice area confirmed by the presence of only one hexagonal pattern. The flake is therefore composed of

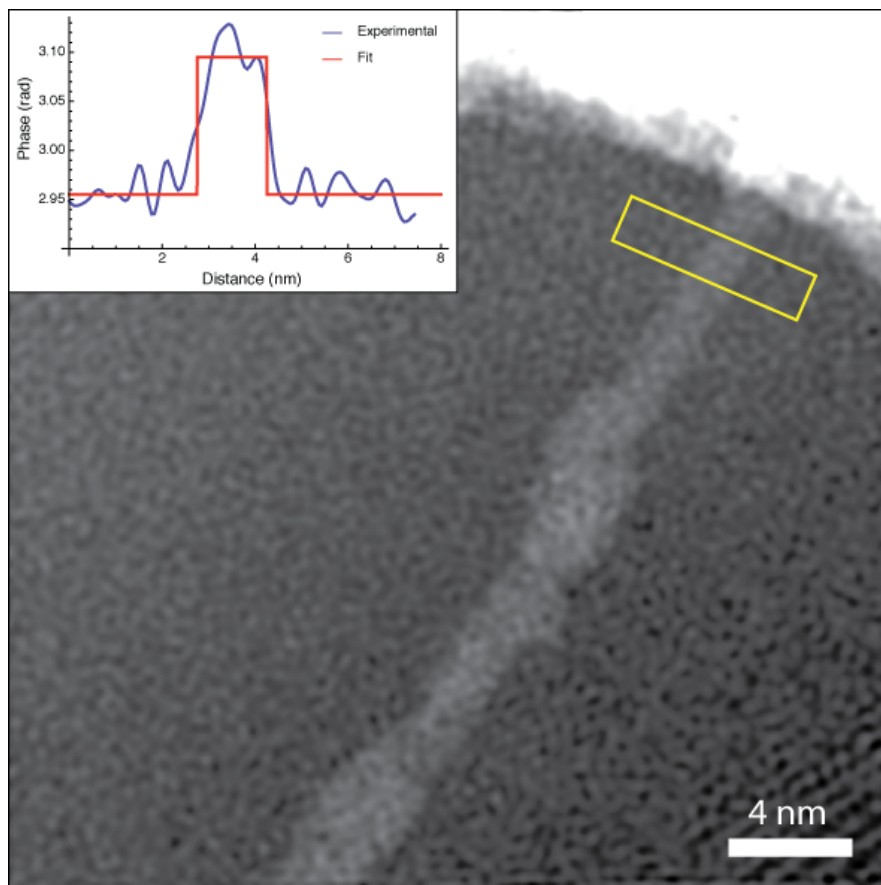


**Figure 3.11:** Reconstructed phase map for an individual suspended SWCNT. In the inset is plotted the phase profile taken over the area marked by the yellow rectangle.

two graphene layers stacked turbostratically.

In order to acquire an hologram of this flake, it is necessary to change the optical set-up of the microscope. After these modifications it has been impossible to get back at the same position over the sample and the hologram has been acquired over the same flake, but on a different position of the border of Fig. 3.12. In this position the flake was composed of three layers, again turbostratically stacked. Figure 3.13 shows the hologram of the flake border.

The three graphene layer are almost invisible below the contrast of the interference fringes which was around 58%. The inset of Fig. 3.12 shows the intensity profile of the interference fringes over the area marked by the yellow rectangle.

Figure 3.14 shows the reconstructed phase map of the flake border region. The reconstruction was done using a circular mask of 70 *pixels* of diameter,

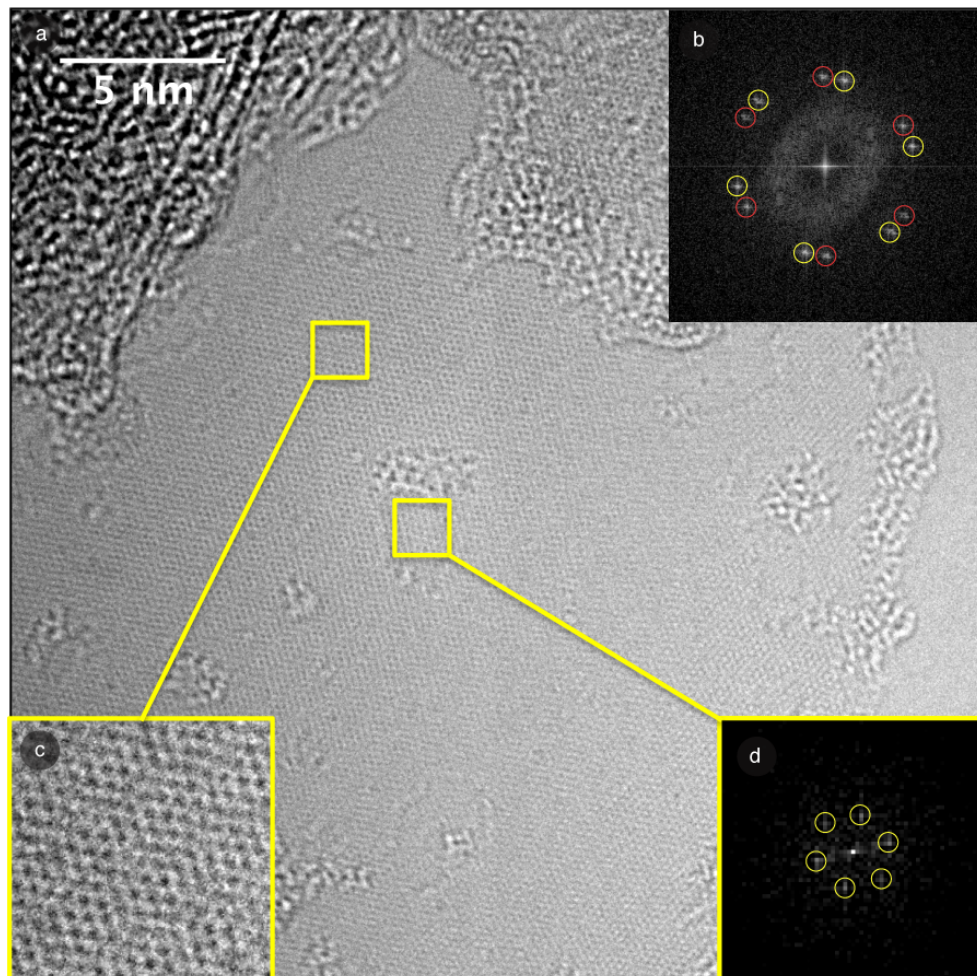


**Figure 3.12:** a) HREM image of the border of a FLG flake where the layer were stacked turbostratically. b) FFT spectrum of the whole image with hexagonal reflections marked. c) Close-up of the indicated region in the HREM image. d) FFT spectrum of the indicated region, with only one hexagonal pattern of reflections.

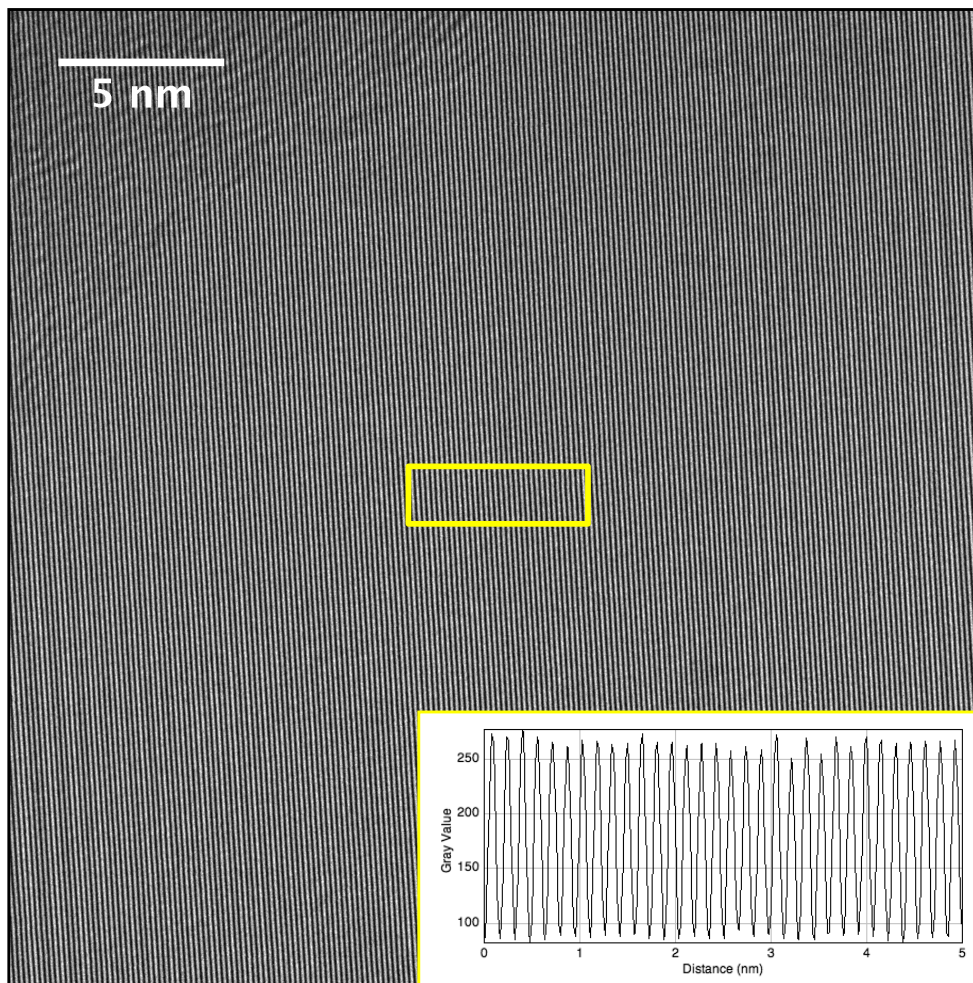


**Figure 3.13:** Hologram of the border of a FLG flake. In the inset is shown the intensity profile of the area marked by the yellow rectangle in the hologram. Fringe spacing is about 0.15 nm, while the final contrast is around 58%.

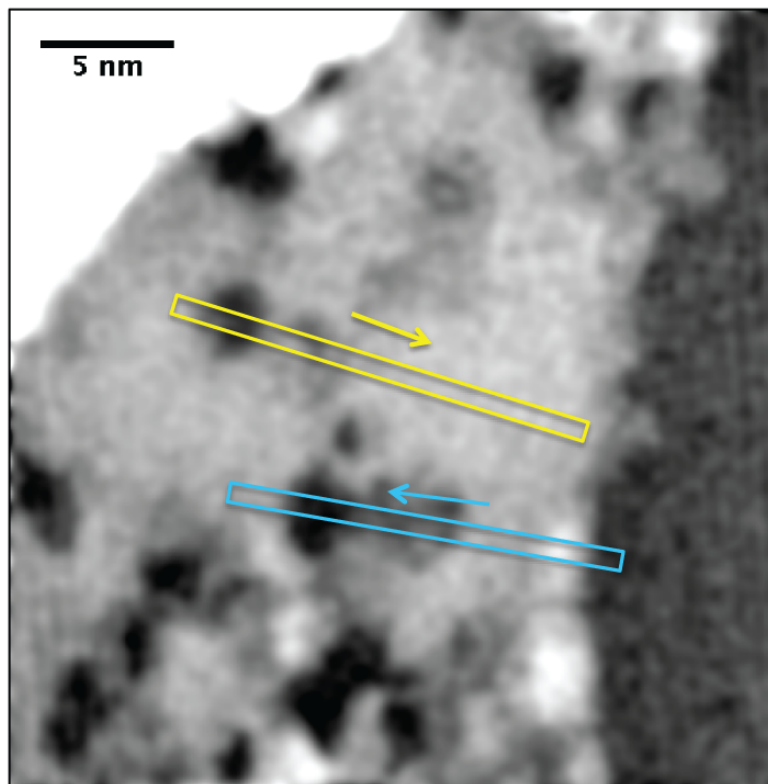


**Figure 3.14:** Experimental reconstructed phase map of the edge of a holey FLG flake. Reconstruction was performed with a final lateral resolution of  $0.5\text{ nm}$ .

corresponding to a lateral resolution in phase map of about  $0.5\text{ nm}$ . In this case the high fringes contrast achieved reduced the overall noise of the image and phase resolution was better than  $0.01\text{ rad}$ . The flake surface is not homogeneous and holes were opened all over due to prolonged previous flake irradiation.

The presence of holes gives us the opportunity to measure the phase displacement due to each graphene layer independently. Phase intensity seems to have step-like variations around the holes and this is confirmed by the analysis of the phase profile taken over the blue and yellow regions, shown in Fig. 3.15. In Fig. 3.15 a) we can see clearly three different phase steps, each of which was estimated to be  $0.06\text{ rad}$ .

On the profile shown in Fig. 3.15 b) from the vacuum level there is a first step of  $0.06$  and a second upper level  $0.18\text{ rad}$  above vacuum level. The subsequent higher bump probably originates from the contribution of some contaminant amorphous carbon near the edge of the flake. Each step in the phase profiles can thus be identified by the phase shift induced by graphene layers. The phase shift of the carbon atoms lattice in a graphene layer can thus be estimated to be  $(0.06 \pm 0.01)\text{ rad}$ .

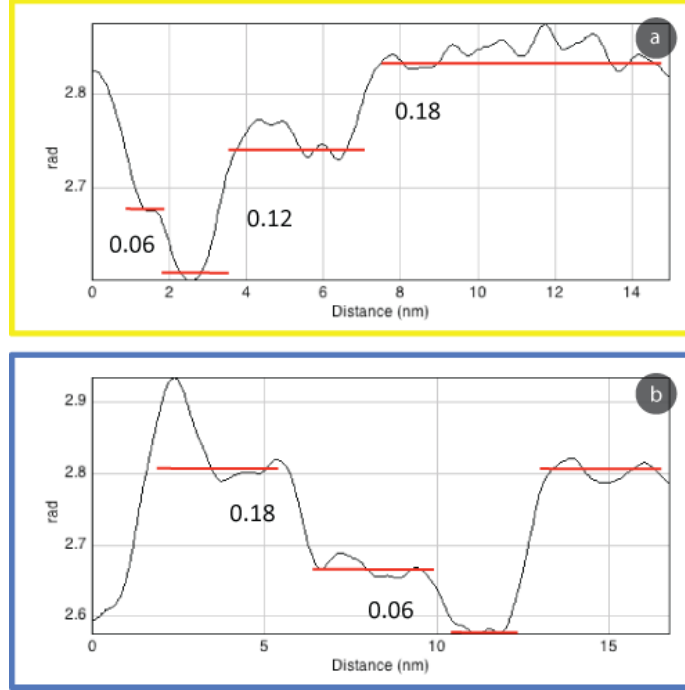


**Figure 3.15:** Experimental plot of the phase profile acquired over a FLG flake. a) Plot relative to yellow region in Fig. 3.14. b) Plot relative to the blue region. In both graphs the values of the phase of individual graphene layers contribution are marked.

### 3.3 Discussion

#### 3.3.1 Mean electrostatic potential of graphene lattices

In electron holography measured phase displacement is proportional to the nanoscopic electric and magnetic fields in the region of the sample. When no magnetic field is present in the sample, Eq. 3.13 reduces to the electrostatic term only:

$$\Delta\phi(\mathbf{r}) = \frac{\pi}{\lambda U_a} \frac{m^*}{m_0} \int_{l(z)} V(\mathbf{r}, z) ds(z) \quad (3.16)$$

$V(\mathbf{r}, z)$  is the resulting potential given by the electric charge density distribution  $\rho(\mathbf{r}, z)$  present in the sample. A standard assumption is that the specimen is neutral so that there is no net charge when the charge density is integrated over the whole space occupied by the sample. Nevertheless, in the previously shown experimental results, we saw that localized charge accumulation is possible. Moreover we saw how the effect of this net charge is to create a stray field in the vacuum nearby the

sample. This fields can be easily mapped by electron holography, even in the case of few electron charges [67]. In the case of the FGC membrane and the SWCNT of Fig. 3.11 we ensured that no stray field was present in vacuum nearby the sample, before measuring phase shifts.

In the experiments performed, lateral resolution in reconstructed phase maps was not sufficient to map atomic charge densities with sub-angstrom precision. At a resolution of few tenths of nanometers, it is possible to reconstruct only the average phase displacement acquired by electrons in that area. Over such a distance it could be reasonable to consider the average amount of charges equal to zero, as in the case of graphene lattice we are considering multiple crystal cells. In reality, due to bonding, the electronic charges redistributes with nearby atoms, and the result is locally a non-zero average effective electrostatic potential.

The average electrostatic potential inducing the phase displacement is called the *mean inner potential* (MIP)  $V_0$  and it can be defined as the average over the volume of the unit cell  $\Omega$  as [68]:

$$V_0 = \frac{1}{\Omega} \int_{\Omega} V(x, y, z) dx dy dz \quad (3.17)$$

In a simplified picture, the MIP represents an average value of the electrostatic energy of the potential hole trapping electrons in a solid. The MIP is a positive quantity and typical values in solid range from around 10 V for the case of amorphous carbon, to several tens of Volts in the case of noble metals [61].

For convenience all the constants and parameters before the integral in Eq. (3.16) will be grouped into an *interaction constant*  $C_E$  defined as:

$$C_E = \frac{\pi}{\lambda U_a^*} \frac{m^*}{m_0} \quad (3.18)$$

that will be dependent on the accelerating energy  $U_a^*$  only [65]. Using the equation (3.17) describing  $V_0$  and Eq. (3.18), we can rewrite the equation (3.16) for the phase displacement of beam electrons as:

$$\Delta\phi = C_E V_0 t(\mathbf{r}) \quad (3.19)$$

where, introducing the volume integral of  $V_0$ , the integration along the electron trajectory inside the sample can be included in the function  $t(\mathbf{r})$  representing the local thickness of the sample.

In the case of the investigated FGC membrane and SWCNTs, the thickness of the sample is a known quantity with atomic precision, as the number of graphene layers traversed by the electrons is precisely determined. A common assumption for the thickness of a layer of graphene is  $0.344 \text{ nm}$  [69], as the distance between two stacked layers in graphite.

In the case of the nanotube of Fig. 3.11, using  $t = 0.344 \text{ nm}$  in Eq. (3.19), each layer induce a phase shift of  $\Delta\phi = (0.07 \pm 0.02) \text{ rad}$  and we obtain  $V_0 = (22 \pm 3) V$ . Using the same procedure, each graphene layer in the FGC membrane of Fig. 3.14 induces a phase shift  $\Delta\phi = (0.06 \pm 0.01) \text{ rad}$  and the MIP of graphene is then  $V_0 = (19 \pm 2) V$ .

Even with the limited precision achieved, we observe a systematic difference between the MIP values for a graphene layer in FGCs and those of SWCNTs. The only difference between the two structure is the curvature of the honeycomb lattice in SWCNTs, compared to the plain one of the FGC, which could account for the measured higher value of MIP.

### 3.3.2 Curvature induced electric dipole effect in CNT

The difference in the values of MIP of the SWCNT and that of the FGC, can be the result of charge redistribution due to the curvature of the lattice in the tube. The curvature of the nanotube wall induces a deformation of the bonding  $\sigma$ -orbitals, bending their direction toward the inner part of the tube.

A theoretical investigation of the effect of this deformation on the carbon orbitals charge redistribution predicts that the displacement of the  $\sigma$  charges toward the inside of the tube induce a redistribution of the  $\pi$  orbital, with a net charge transfer from the concave region towards the convex one [70]. The effect of this charge transfer is the induction of a net dipole charge density distribution over the surface of the wall, as shown in the schematics of Fig. 3.16.

The effective dipole moment  $\mu$  is dependent on the radius of the tube only, without contributions from tube chirality and, for tubes similar to the one observed, it follows a trend described by the equation [70]:

$$\mu = \frac{0.087}{R(\text{nm})} \text{ Debye} \quad (3.20)$$

For the curvature of the tube we measured,  $R = 0.7 \text{ nm}$ , we can calculate an expected dipole moment  $\mu = 0.1 D$  for each carbon atom of the tube.

The total charge of the crystal is still zero, and in the same way there is no net dipole moment. Nonetheless this dipole distribution induces a net quadrupole

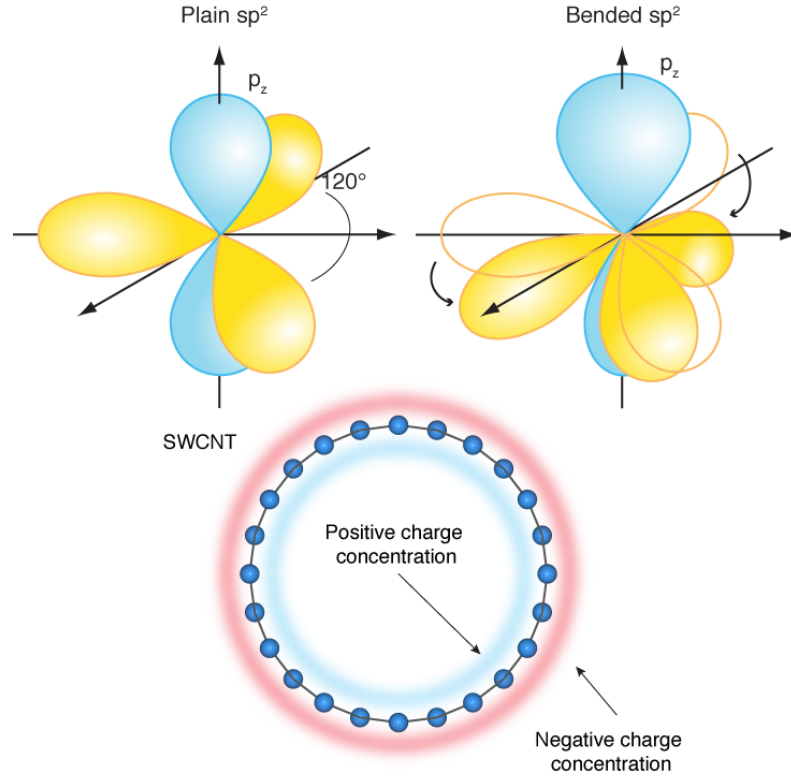


**Figure 3.16:** Charge redistribution on the wall of a SWCNT due to its curvature. Compared to a plain one an  $sp^2$  deformed orbital has the  $\sigma$  parts bended below the  $xy$ -plane and the upper part of the  $p_z$  orbital increase its electronic population. The net effect is a negative charge density distribution on the outer wall and a positive one on the inside, originating a net dipole moment pointing inside the tube.

moment, which generates an electric field acting on the electrons of the beam. In this configuration, the surface dipole distribution originates a constant electric potential  $V_\mu$  in the volume enclosed by the surface, which can be written as [68]:

$$V_\mu = 4\pi k_0 \frac{N_A}{A_{cell}} \mu \quad (3.21)$$

where  $k_0 = 1.44 \text{ Vnm}/e$  is the Coulomb's force constant,  $N_A = 2$  is the number of carbon atoms per unit cell in the honeycomb lattice and  $A_{cell} = 4.7 \cdot 10^{-2} \text{ nm}^2$  is the area of the unit cell. Outside the tube, the electric field induced by the surface dipole distribution goes to zero as  $1/R^3$  and its effect on the phase can be neglected. For a tube of radius  $R = 0.7 \text{ nm}$ , the net dipole moment per atom of  $0.1 D$  originates a positive potential  $V_\mu = 2 \text{ V}$  inside the tube.

The electrostatic potential inside the tube induces an additional phase displacement of the electron wavefront, with respect to the case of a plain honeycomb lattice. If we add  $V_\mu$  to the value of  $V_0$  for the plain honeycomb lattice calculated for the FGC, we obtain an expected value  $V_0 = 21 V$  for the SWCNTs matching the experimental value of  $V_0 = (22 \pm 3) V$  for the tube of radius  $R = 0.7 nm$ .

We can compare our experimental values for MIP with that obtained previously by Lin *et al.* for SW- and MW-CNTs in a similar experiment [69]. They measured the phase displacement of a large SWCNT of about  $2 nm$  of radius and calculated a MIP  $V_0 = (20 \pm 6) V$ . For such a large nanotube, the effect of curvature is less important, as it induces a dipole moment, from Eq. (3.20) with  $R = 2 nm$ ,  $\mu = 0.04 D$ . As the curvature effect is less pronounced, the MIP value they report is therefore comparable with the one we measure for the plain lattice in the FGC.

The researchers measured the phase displacement of a MWCNT, measuring a MIP of  $V_0 = (24 \pm 4) V$ , significantly higher than the one measured for the SWCNT. In this case the nanotube, with a radius  $R = 2 nm$ , was composed by 5 walls, and the sum of the dipole contribution from each one can account for the higher measured value of the MIP.

### 3.3.3 The effect of valence charges distribution on the phase shift

As a final remark, let's turn our attention to the strong dependence of the electronic phase shift on charge redistribution effects due to atomic bonds in the crystal. As previously discussed, the MIP, and phase shift therefore, depends directly on the quadrupole moment of the charge distribution. Unfortunately precise determination of the charge distribution in real crystals is not not easy to measure experimentally and even more difficult to model theoretically.

In solid state physics it is common to calculate electron scattering factors for solids from x-ray scattering data. The interaction between x-ray photons and electrons nevertheless is completely different, as photon scattering is basically sensitive to the electronic part of the charge distribution  $\rho(\mathbf{r})$  in a crystal, while electrons are scattered by the complete Coulomb potential, related to the charge by Poisson's equation.

In electron microscopy the crystal potential, and its average effective value, the MIP, are of fundamental importance since they are the base of all images and diffraction patterns simulations. A precise knowledge of these quantities is thus mandatory. A common approximation made in calculating the crystal lattice potential is to assume the crystal as built of charge distribution of single atoms, with spherically symmetric potentials and neglecting any bond contribution [71].

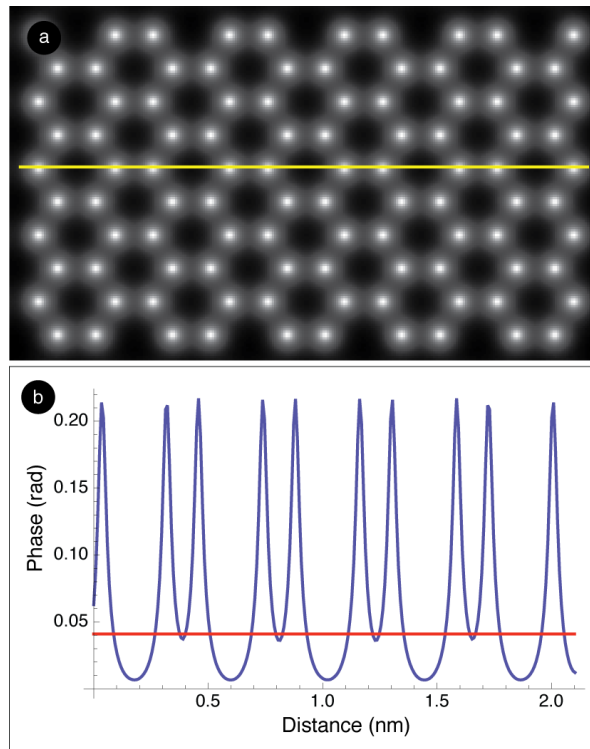


**Figure 3.17:** a) Simulated phase map of a graphene layer using spherically symmetric atomic potentials generated by JEMS. b) Profile of the phase intensity along the yellow line and average phase shift of  $0.041 \text{ rad}$  marked in red.

Figure 3.17 a) shows the phase map of a graphene layer, simulated using the above spherical approximation for projected atomic potentials. The simulation has been computed for electron beam energy of  $100 \text{ keV}$ , as used experimentally, and using the modified Doyle-Turner atomic potentials [71] used in the simulation algorithm of JEMS<sup>2</sup>. The simulated phase image has subatomic resolution and the spherical symmetry around the peaks corresponding to the center of the nucleus of carbon atoms is clearly visible.

Figure 3.17 b) shows the intensity profile of the phase taken along the yellow line. The peak corresponding to the positions of nuclei give a maximum phase displacement of  $0.21 \text{ rad}$ , while at the center of each hexagon the phase is less than  $0.01 \text{ rad}$ . In our holographic experiment we had a much lower resolution and what

<sup>2</sup><http://cimewww.epfl.ch/people/stadelmann/jemsWebSite/jems.html>

we measured was the average over distances of about  $0.5 \text{ nm}$  of this local phase shift.

To obtain comparable results we can compute the spatial average of the simulated phase image over distances greater than  $0.5 \text{ nm}$  corresponding to our experimental resolution. The result is the average phase shift (red line in Fig. 3.17 b)), proportional to the average electrostatic projected potential  $V_0$ . If we do not consider bonding effect the average phase shift for a single graphene layer is  $\Delta\phi = 0.041 \text{ rad}$ , and the MIP results to be  $16 \text{ V}$ , which is significantly below the experimentally measured values of  $0.06 \text{ rad}$  and  $V_0 = 19 \text{ V}$ . Neglecting the contribution of valence-charge distribution in phase simulations clearly originates a remarkable effect on the value of MIP, which must be taken into account.

## Conclusions

In this Chapter we discussed the experimental results of the holographic investigation performed on SWCNTs and FGCs samples. We introduced the basics of electron interference and we discussed the experimental set-up to realize holograms of these carbon-based nanostructures. In the experiments we used a low-voltage ( $100 \text{ kV}$ ) TEM configuration, to reduce beam damage to the samples, in an aberrations-corrected microscope. We demonstrated how this experimental set-up allowed for highly sensitive and laterally resolved phase maps reconstructions.

The phase displacements induced by an isolated SWCNT and that of the monoatomically thin graphene crystal were successfully measured. The electric potential generated by the surface distribution of electric dipole density, due to the valence-charge redistribution, induced by the curvature of the honeycomb crystal lattice in a SWCNT [70], could be measured for the first time by electron holography.

# **3D RECONSTRUCTION AT THE NANOSCALE: MAPPING GRAPHENE WAVINESS**

I do not think that the wireless  
waves I have discovered will have  
any practical application.

*(Heinrich Rudolf Hertz)*

## 4.1 Introduction

As previously discussed in the first Chapter, the stability of 2D crystals was debated for decades. According to the so-called Mermin-Wagner theorem, in 2D membranes thermal agitation will induce long wavelength fluctuations which will destroy the long-range crystalline order [21]. The existence of graphene was then debated until the discovery of a full set of 2D crystals in 2005 [1]. Since the beginning, it was clear that the structure of graphene was not perfectly flat.

Moreover, in freely suspended graphene sheets, TEM investigation showed that the surface of graphene is intrinsically rippled and undulated. Experiments show the evidence for undulations with a typical wavelength of the order of  $5 - 10 \text{ nm}$  and amplitude modulations of less than  $1 \text{ nm}$  [14, 25]. Further, a large amount of theoretical investigations have subsequently demonstrated that undulations and ripples are indeed intrinsic features of a 2D crystal. Deformations of the lattice in 2D crystals are responsible for the existence of long-range crystalline order, as these undulations stabilize the structure by minimizing the total elastic energy of the membranes [15].

The study of curvature in graphene is then of great interest, since through those structural features is possible to describe and understand the electronic properties of materials like CNTs and fullerenes. In addition, theory also predicts that surface undulations will induce novel magnetic properties as mid-gap states arise as an effective pseudo-magnetic field was acting locally [18]. Further, ripples have been shown to modulate the charge transport in graphene, due to induced electronic potentials which behaves as long-range Coulomb scatterers for the carrier itself [72]. Another possible effect on carriers is that smooth surface modulations couple with charge inhomogeneities, and selective hopping of electrons or holes, between valleys and hills of the membranes, creates puddles of electrons and holes [16, 17].

A detailed investigation of the three-dimensional structure of graphene membranes is crucial to fully understand their electronic properties. To date, only few experimental results indirectly provide information on the three-dimensional (3D) atomic structure of graphene from the investigation of peaks intensities in electron diffraction patterns [14, 25].

In this Chapter we will present a novel method to reconstruct the 3D waviness at the nanoscale of 2D crystal (i.e. graphene) from high-resolution transmission electron (HREM) images. Differently from other approaches, such as electron tomography [73], this method requires only one HREM micrograph of a crystal flake

and relies on the geometrical analysis of the spatial frequencies composing the image to recover 3D information [74]. The details of the reconstruction procedure will be thoroughly discussed and the technique will be applied to the simple case study of FGC to recover crystal surface bending at a folded border.

## 4.2 Mapping geometric distortions

### 4.2.1 Mapping 3D waviness of 2D membranes

In Chapter 2 we discussed the basics of HREM imaging at the TEM. The interference pattern recorded in a HREM image closely reflects the arrangement of crystal planes in the sample. It is far beyond the aim of this manuscript to provide a complete description of the HREM image formation process [75]. Here we want to point out that, although not universally true, in many cases it is possible to draw a direct relation between the contrast in the image and the atomic arrangement in the sample. Numerous imaging techniques exploit this correspondence to obtain quantitative information (i.e. strains, etc. . .) from an HREM image [74].

In the novel 3D reconstruction method presented here, we will make use of the information about the geometric distortion of the interference fringes, composing an HREM image, to quantify and reconstruct the 3D undulations of FGC membranes. Let's consider a one-dimensional lattice chain as shown in Figure 4.1 a). The atomic chain is bended in the  $z$ -direction, with the interatomic distance kept constant. We can imagine to look at such a sample in a TEM considering the direction of the electronic beam to be parallel to the  $z$ -axis.

In this simplified scenario, in the TEM image we will see the atomic positions projected in the direction of the beam over the  $x$ -axis. In the image of Fig. 4.1 a) these projections are represented by black circles on the  $x$ -axis. The distance between the projected positions in the image varies accordingly with the slope of the undulated atomic chain. Figure 4.1 b) shows a profile of the local strain as it would be calculated from the projected atomic positions. Using simple geometry, it is clear that a measure of the “*apparent strain*” in the image will provide an immediate measure of the local slope of the undulated chain, therefore providing a complete reconstruction of its 2D structure.

In this oversimplified model, we assumed that the interatomic distances between atoms of our mono-dimensional crystal do not change upon bending the chain. Our *real world* samples will be quasi-2D FGC membranes and it is impossible to bend

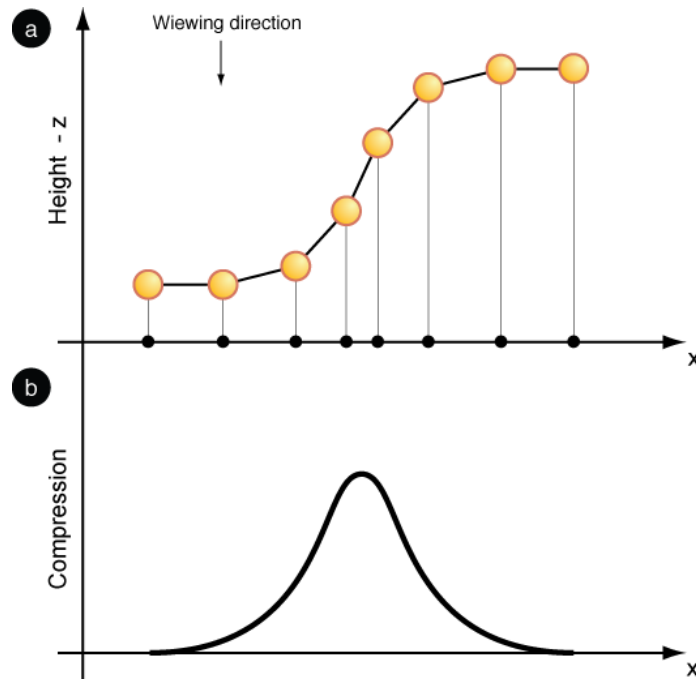


**Figure 4.1:** a) Schematics of an atomic chain undulated in the  $z$ -direction. The interatomic distances are kept constant, but, when viewed along the  $z$ -axis, the projected positions appear as strained due to the undulation of the chain. b) Plot of the compression as it appears from the projected positions.

a 2D crystal in both direction, without introducing some variation of the interatomic distances. Using the idea described above for FGC undulations and 3D deformations, the interatomic distances of projected positions in an HREM image will therefore be the result of both projection and mechanical strain.

Graphene extraordinary stiffness comes to help. The Young modulus of graphene membranes was recently measured to be of the order of 1  $TPa$  [76]. Theoretical calculations for two dimensional undulations predict that the change in interatomic distances will be less than 1% [15]. For larger measured variations in the projected interatomic distances, we will therefore neglect the contribution of mechanical compression in the reconstruction. As we will see further, we will deal with strains of the order of 5%. The above condition is therefore satisfied and all the measured compressions will originates from the projection of the 3D structure only.

The measurement of the strain from an HREM image of a undulated FGC can be done using the methods of Geometric Phase Analysis (GPA), which will be briefly described in the next Subsection.

### 4.2.2 Geometric phase analysis of HREM images

Geometric phase analysis is a technique that analyzes the geometric distortions in the HREM image of a crystal lattice. The technique relies on the Fourier analysis of the image, similarly to holographic reconstruction of the electronic phase, as discussed in Chap. 3. In this case the reconstructed phase is called “geometric” to avoid confusion with the electron holography one. In this Subsection, the meaning of the *geometrical phase* will be explained, and the information it contains about the geometric distortions of the image discussed. At this stage it is appropriate to introduce some formalism that will facilitate understanding the underlying mechanism of GPA strain reconstruction.

An HREM micrograph is a 2D image and a vector  $\mathbf{r}$  can be defined in order to indicate the position of a point. The intensity  $I(\mathbf{r})$  of the HREM image, as discussed in Chap. 2, is the superposition of interference fringes created by the various beams diffracted by the sample. Using the same formalism, we can identify the direction of these beams, and the direction of the relative system of fringes in the image, with the wave-vectors  $\mathbf{g}$  of the reciprocal space. If we consider the image of a perfect crystal, free from any deformation, its intensity  $I(\mathbf{r})$  can be expressed as a Fourier series over the frequencies  $\mathbf{g}$ , as:

$$I(\mathbf{r}) = \sum_{\mathbf{g}} I_{\mathbf{g}} e^{2\pi i \mathbf{g} \cdot \mathbf{r}} \quad (4.1)$$

where  $I_{\mathbf{g}}$  is a coefficient representing the *intensity* of the fringe system originating from that particular  $\mathbf{g}$ .

In the reciprocal space the Fourier transform of (4.1) becomes:

$$\tilde{I}(\mathbf{k}) = \sum_{\mathbf{g}} I_{\mathbf{g}} \delta(\mathbf{k} - \mathbf{g}) \quad (4.2)$$

where  $\delta$  is the Dirac delta function. For a perfect crystal, the reciprocal space is non-zero only at the positions of the  $\mathbf{g}$  vectors.

Deformations in the lattice of the specimen can be introduced with the displacement field  $\mathbf{u}(\mathbf{r})$  with the following transformation [77]:

$$\mathbf{r} \mapsto \mathbf{r} - \mathbf{u}(\mathbf{r}) \quad (4.3)$$

The effect of this displacement vector field is that the reciprocal lattice directions  $\mathbf{g}$  are not defined globally for the crystal, instead they are local, depending on the position  $\mathbf{g}(\mathbf{r})$ .

The Eq. (4.1) then becomes, for a deformed crystal:

$$I(\mathbf{r}) = \sum_{\mathbf{g}} I_{\mathbf{g}} e^{2\pi i \mathbf{g} \cdot \mathbf{r}} e^{-2\pi i \mathbf{g} \cdot \mathbf{u}(\mathbf{r})} \quad (4.4)$$

In real crystals lattice distortions are not the only imperfections present, since we need to take into account thickness variations and, as in the case of graphene membranes, possible undulations. All these effects impose to consider the intensity coefficients  $I_{\mathbf{g}}$  to be local function  $I_{\mathbf{g}}(\mathbf{r})$  of the position [74].

If we define the complex functions  $H_{\mathbf{g}}(\mathbf{r})$  as:

$$H_{\mathbf{g}}(\mathbf{r}) = I_{\mathbf{g}}(\mathbf{r}) e^{-2\pi i \mathbf{g} \cdot \mathbf{u}(\mathbf{r})} \quad (4.5)$$

then the Fourier transform of Eq. (4.4) becomes:

$$\tilde{I}(\mathbf{k}) = \sum_{\mathbf{g}} \tilde{H}_{\mathbf{g}}(\mathbf{k}) \otimes \delta(\mathbf{k} - \mathbf{g}) \quad (4.6)$$

In the case of a deformed crystal, in the reciprocal space there is now some dispersion of the intensity around the positions of the reciprocal vectors  $\mathbf{g}$ . The information about the deformations in the sample are encoded in the  $\tilde{H}_{\mathbf{g}}(\mathbf{k})$  functions. The amplitude term of these functions will give the modulation in intensity of the interference fringes in the direction of each  $\mathbf{g}$ , while the phase term describes the variations in the inter-fringe spacing around the image area. As already mentioned, the phase term is called “geometric phase” to prevent ambiguity with the phase of the electron wavefunction as reconstructed by electron holography.

The workflow of a GPA phase reconstruction is similar to that of electron holography reconstruction of the electronic amplitude and phase form an hologram, and represented in Fig. 3.5. The original HREM digital image is Fast Fourier Transformed and, instead of sideband as in electron holography, the pixels nearby a specific  $\mathbf{g}$  vector are selected using a circular mask mask. The distance between two nearby  $\mathbf{g}$  limit the diameter of the mask, and therefore it limits the resolution of the reconstructed maps, which is usually of the order of the nanometer. The effect of the shape of the mask is beyond the scope of this manuscript and the explicit expression of the mask will be omitted in the following calculations (see specific literature for details [75]).

Selecting the region of the reciprocal space around a particular  $\mathbf{g}$  we are selecting one specific  $\tilde{H}_{\mathbf{g}}(\mathbf{k})$  and setting the origin of the cartesian reference system to the position of  $\mathbf{g}$ . Inverse FFT will give you back the complex image:

$$FFT\left(\tilde{H}_{\mathbf{g}}(\mathbf{k})\right) = H_{\mathbf{g}}(\mathbf{r}) = I_{\mathbf{g}}(\mathbf{r}) e^{-2\pi i \mathbf{g} \cdot \mathbf{u}(\mathbf{r}) + \phi_{\mathbf{g}}} \quad (4.7)$$

When transforming back an additional phase constant  $\phi_g$  emerges. Mathematically the process should recover back  $H$  without any additional term, but the pixel nature of the image make impossible to determine exactly the position of the  $\mathbf{g}$ , which lies often in sub-pixel position. This error in the re-centering of the reciprocal space means that a  $\delta$ -like component is still present and will transform back to a constant phase in real space. The constant phase term  $\phi_g$  is removed from the reconstructed phase by re-normalizing the background over a reference area of the map [74].

The result of the reconstruction procedure is a complex image corresponding to one  $H_g(\mathbf{r})$ . Amplitude and phase terms will be calculated according to the equations:

$$\begin{aligned} I_g(\mathbf{r}) &= \Re\left(H_g(\mathbf{r})\right) \\ P_g(\mathbf{r}) &= \Im\left(H_g(\mathbf{r})\right) - \phi_g \end{aligned} \quad (4.8)$$

Where  $\Re$  and  $\Im$  stands respectively for real and imaginary parts. The displacement field  $\mathbf{u}(\mathbf{r})$ , is a two-dimensional vector field, and to recover it in every direction it is required to reconstruct the  $H_g$  of two non collinear  $\mathbf{g}_1$  and  $\mathbf{g}_2$ . Mathematically we need to find two vectors  $\mathbf{a}_1$  and  $\mathbf{a}_2$ , in the real space, solving the equation:

$$\mathbf{u}(\mathbf{r}) = -\frac{1}{2\pi} \left[ P_{\mathbf{g}_1} \mathbf{a}_1(\mathbf{r}) + P_{\mathbf{g}_2} \mathbf{a}_2(\mathbf{r}) \right] \quad (4.9)$$

From the displacement field  $\mathbf{u}(\mathbf{r})$  it is finally possible to calculate the strain tensor  $\epsilon$  [74]:

$$\epsilon = \begin{pmatrix} \epsilon_{xx} & \epsilon_{xy} \\ \epsilon_{yx} & \epsilon_{yy} \end{pmatrix} = \begin{pmatrix} \frac{\partial u_x}{\partial x} & \frac{\partial u_x}{\partial y} \\ \frac{\partial u_y}{\partial x} & \frac{\partial u_y}{\partial y} \end{pmatrix} \quad (4.10)$$

All these procedure are available as a series of script implementing numerically GPA reconstruction and strain calculation. The software gives you the strain tensor as separated components expressed as follows [74]:

$$\begin{aligned} \epsilon_{xx} &= \frac{\partial u_x}{\partial x} && \text{Symmetric strain Ex} \\ \epsilon_{yy} &= \frac{\partial u_y}{\partial y} && \text{Symmetric strain Ey} \\ \epsilon_{xy} &= \frac{1}{2} \left( \frac{\partial u_x}{\partial y} + \frac{\partial u_y}{\partial x} \right) && \text{Symmetric strain Exy} \\ \Delta_{xy} &= \frac{1}{2} \left( \frac{\partial u_x}{\partial x} + \frac{\partial u_y}{\partial y} \right) && \text{Mean dilatation Dxy} \\ \omega_{xy} &= \frac{1}{2} \left( \frac{\partial u_y}{\partial x} - \frac{\partial u_x}{\partial y} \right) && \text{Rotation Rxy} \end{aligned} \quad (4.11)$$

The definition of the  $x$  and  $y$  reference axis are chosen by the user at its own convenience.

Geometric phase analysis provides the instruments to reconstruct lattice deformations starting from the HREM image of a crystalline sample. All the limits of the technique are due to this specific image-based approach. As already said, the image is representative of the lattice structure of the sample. Intensity features in the image, however, will be directly connected to the arrangement of planes in the sample only under restrictive conditions. A set of constraints is imposed by the HREM technique itself and others lie in the sample structure. It is beyond the scope of this manuscript to examine all the parameters determining the limits and the precision of the reconstructed strain maps [75]. I will point out specific limitations directly as they will emerge in the discussion of the the experimental images in the following sections.

Here it is important to notice that the objective lens, and other imaging parameters, can strongly affect the result of the analysis. Most of the problems arising from the way the microscope transfer the spatial information from the specimen to the imaging plane, can be minimized by the usage of aberrations-corrected microscopes (see Chap 2). The corrected microscope transfer function provides a faithful transfer of spatial frequency within a large range. The remaining geometric distortions induced by the lenses are removed by subtracting from the resulting phase images a reference deformation map specific of the microscope used.

The sample itself can presents some important problems in the analysis of the HREM images. Variation in the thickness of the sample in the area under investigation generates an additional geometric phase displacement that will be impossible to distinguish from that of changes in the interatomic distances. Strong contrast variations in the intensity of the fringes, and in the limiting case a contrast inversion, will be interpreted by the numerical routine as an additional phase displacement not related to any physical strain.

Graphene membranes resolve or minimize many of the above problems. The most important limitation in TEM sample preparation is the control over the thickness of the specimen. In the case of FGC membranes the thickness is ideally uniform, and it can be experimentally determined at atomic level without error and is normally constant over a large area. In our analysis we will concentrate on the determination of the apparent compression induced by the vertical geometrical projection of the

bended membrane. As already discussed, physical elastic strains will be present, but with an intensity that will be negligible compared to the geometrical effect. We have thus a quasi-perfect sample to investigate with GPA technique.

## 4.3 Experimental results

### 4.3.1 Experimental set-up and sample preparation

Particular care was used in setting up the experimental conditions for HREM imaging. The experiment was performed using an aberrations-corrected Tecnai F20 TEM. Beam acceleration voltage was reduced to 100 *kV* to avoid structural damage of the carbon lattice. The optical alignment of the microscope and of the corrector in particular, was finely tuned to ensure correction of all aberrations up to the fifth order.

The sample was chosen according to the following criteria: the sample must have an explicit geometrical distortion, where the effect of projection induced apparent strain and real mechanical strain could be easily separated.

Mechanically exfoliated graphite flakes fulfill all these constraints. Thin electron transparent flakes are easily obtained with thin borders composed of few-layers, typically folded over themselves. Natural graphite powder was exfoliated using a mortar and a pestle and successively sonicated in isopropanol for additional exfoliation and dispersion. The resulting solution was drop-casted over standard 3 *mm* TEM holey carbon grids.

### 4.3.2 HREM imaging

Different flakes were imaged under the conditions above described. A preliminary GPA analysis was performed looking for sufficiently large localized strains. Most of the flakes produced by the aforementioned method are relatively thick and therefore they are less affected by geometrical distortions. Nevertheless few suitable flakes were present and one of them is shown in Figure 4.2. The flake is folded over itself along two borders. From an analysis of the borders (0002) fringes it is possible to state that the flake is composed of three superimposed graphene layers (six total layers).

By looking closer at the edges, like in the inset a) of Figure. 4.2 it is possible to determine the stacking order of the composing graphene sheets. The series of intensity peaks corresponding to the position of benzene rings in the stacked layers

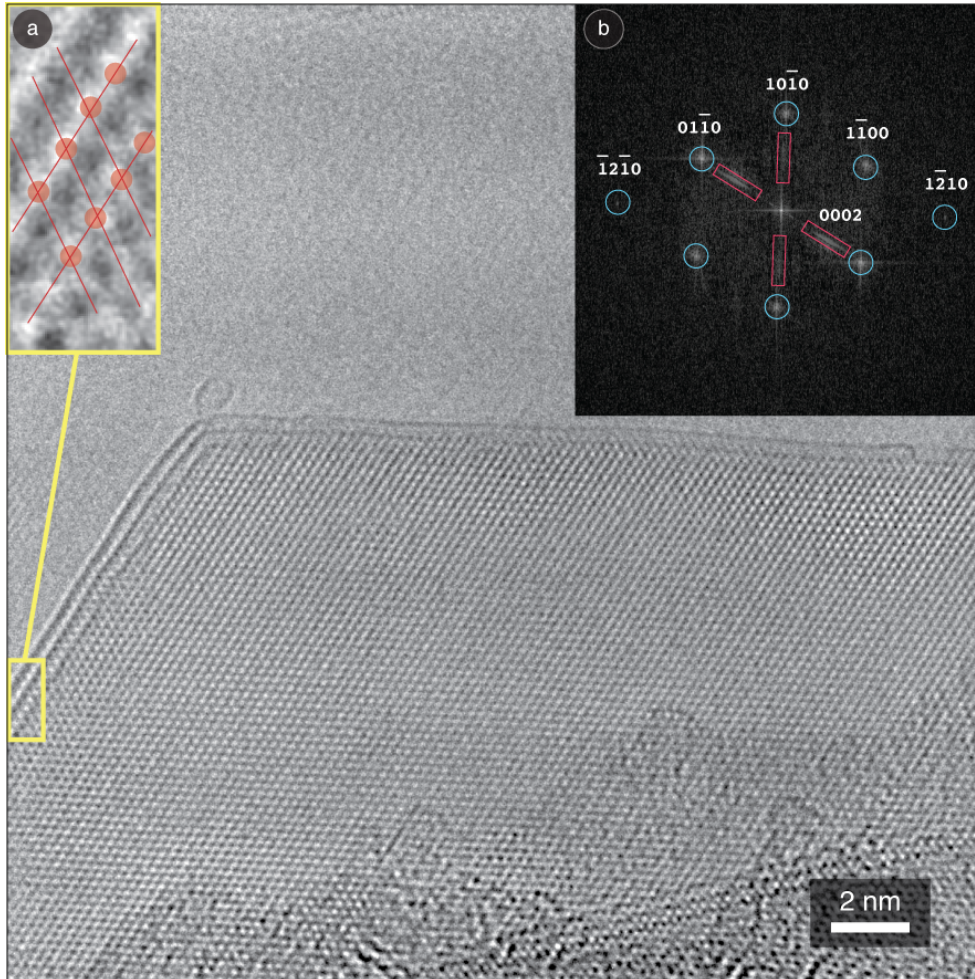


**Figure 4.2:** HREM image of the border of a FGC flake. The membrane is folded over itself on two sides, exposing (0002) fringes, which makes possible to determine the number of layers in the membrane as 3. The inset a) shows a close-up of the (0002) folded zone in the yellow rectangle. From the disposition of the intensity peaks it is possible to determine that the flake has *ABA* stacking sequence. The inset b) shows the FFT of the HREM image. Graphite reflections are marked for easier view (blue circles) and (0, 0, 0, 2) reflections of the two borders are clearly visible (red rectangles).

is highlighted by red circles.

Their alignment along lines not perpendicular to the flake edge is characteristic of *ABAB* stacking. The inset b) of the same figure shows the FFT spectrum of the image. Graphite principal reflections are highlighted (blue circles) as long as folded borders (0, 0, 0, 2) reflections (red rectangles).

An important feature of the image is the defocus difference which is possible to appreciate between the left-side and upper borders. Left border shows some evident Fresnel fringes due to under-focus, while the upper border is almost at focus, with no Fresnel fringe visible. This suggest that there is some height difference between the two regions.

The height difference is also confirmed by the contrast variations of the HREM fringes. To partially explain this phenomenon it is important to notice that in aberrations-corrected microscopy the Scherzer defocus [54] for optimal imaging conditions is zero, since zero is the value of the spherical aberration coefficient. Slight changes in the defocus value therefore reflects in a significant change of the contrast associated to HREM fringes.

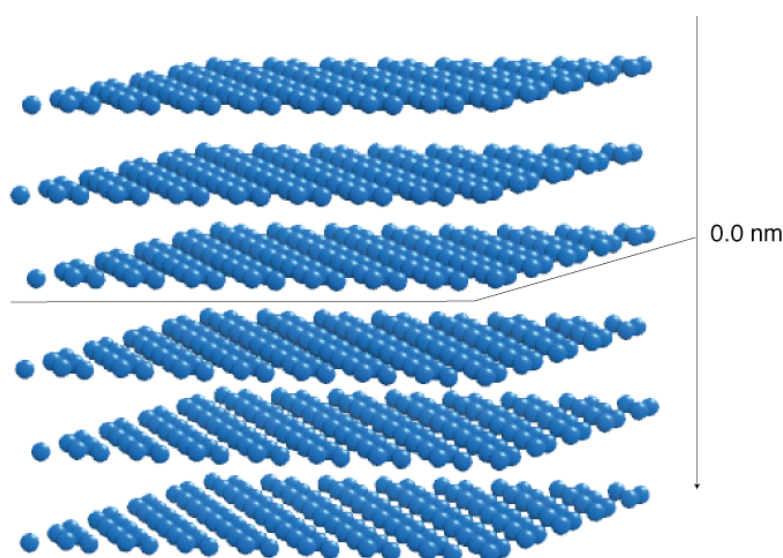


**Figure 4.3:** Schematics of the simulated structure. In the image is indicated the reference for the zero of defocus used for the calculations.

The effect of defocus in contrast will be clear from the comparison between image simulations of a FGC composed of six graphene layers as the experimentally observed one. Figure 4.3 shows a schematics of the simulated structure. In the image is indicated the reference for the zero of defocus used for the calculations.

Simulations were performed using JEMS multi-slice routine with imaging conditions identical to the one of the acquired image. To account for depth effects, the structure was sliced perpendicularly to  $z$  in 10 parts. For each part it has been calculated the projected atomic potential and the interaction of the beam electron with this potential. The exiting electron wave from each slice is propagated to next

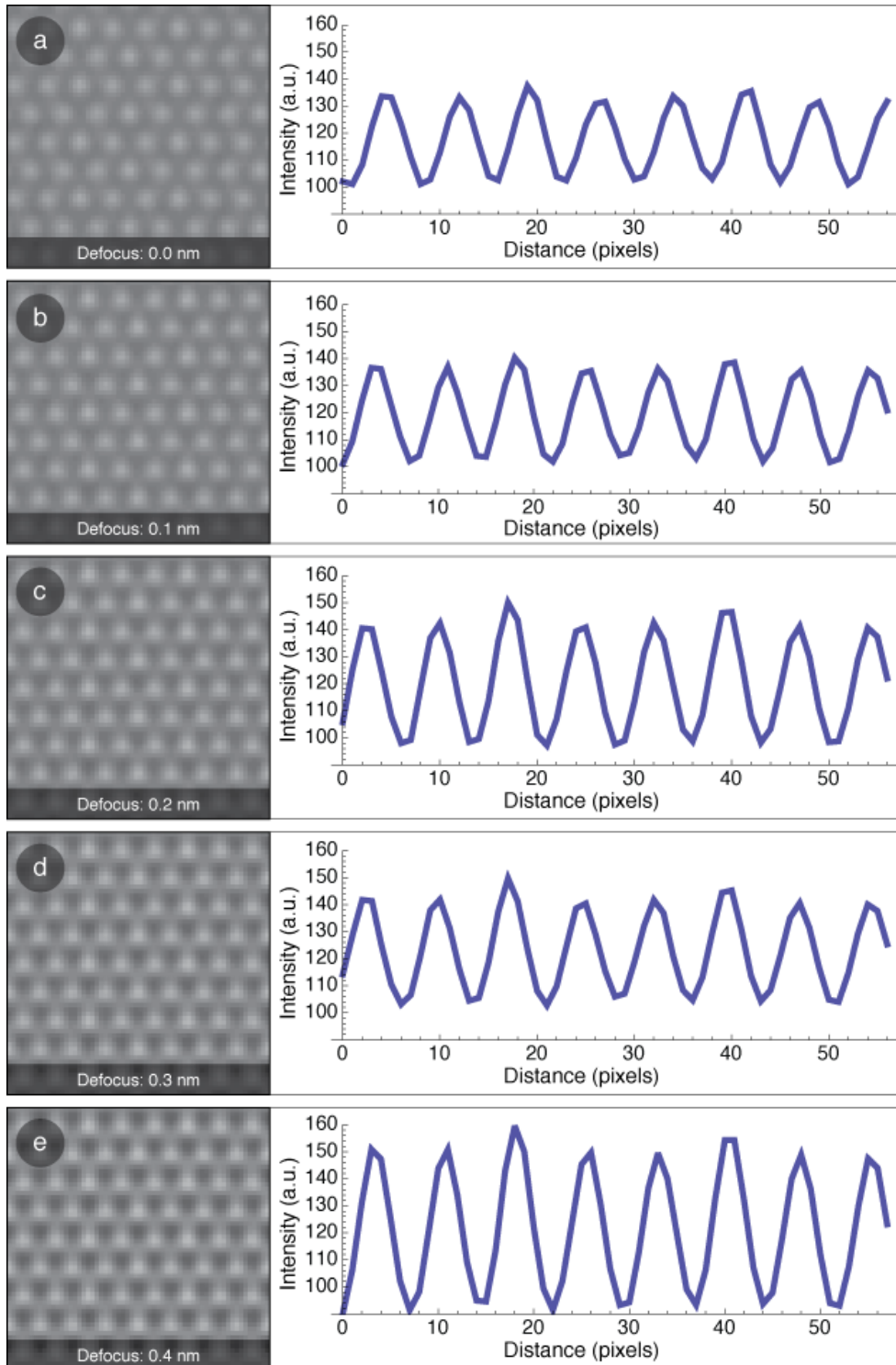


**Figure 4.4:** Results of the HREM image simulations for the structure of Fig. 4.3. A profile of the intensity along a horizontal line in the center of the image is plotted for each simulated image.

one where it will interact with the successive layer of projected atomic potentials.

Figures ?? a) to e) shows the results of the simulations. For each value of the defocus a different simulation was performed. For each simulated HREM image is plotted the intensity of the peaks along a horizontal line in the middle of the image.

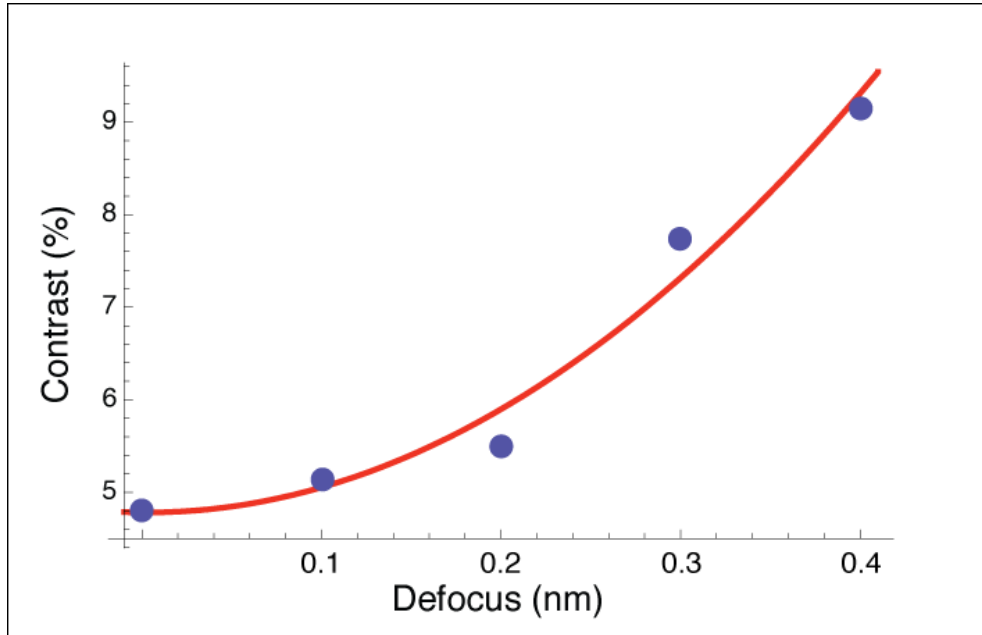


**Figure 4.5:** Plot of the values of the contrast computed for the image simulations. The red line is just a guide for the eyes.

For each value of the defocus, an average value for the contrast of the peaks was calculated according to the simple definition:

$$c = \frac{I_{max} - I_{min}}{I_{max} + I_{min}} \quad (4.12)$$

The values of the contrast of the HREM peaks for each different defocus is plotted in Figure 4.5. We have chosen slight defocus variations, which are impossible to experimentally achieve at the TEM, since the minimum defocus step for the objective lens is of the order of 1 *nm*. Nevertheless it is clear that even 0.1 *nm* steps give appreciable changes in the contrast of peaks.

The hypothesis that the membrane bends near the border, inducing a compression of the projected atomic positions, is confirmed by the reported smooth contrast variations. It is well known that FGCs membranes folds and scrolls at the borders, so we can guess the 3D structure of a folded border as shown in Figure 4.6. The three-

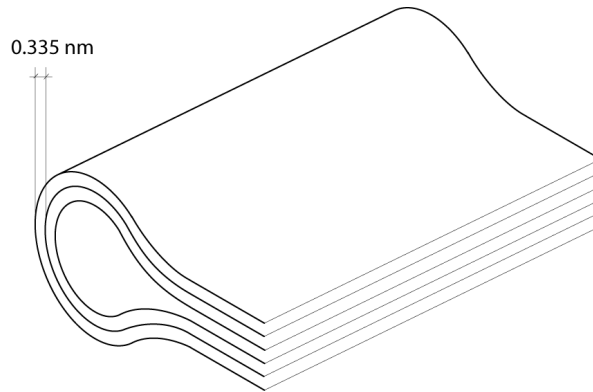


**Figure 4.6:** Proposed schematics for the structure of the folded flake under investigation.

layers flake starts to bend, makes a curve and folds over itself forming six stacked layers.

This flake is folded along particular directions. Looking at the FFT spectrum of the image we notice that the upper and left border are folded respectively perpendicularly to  $(01\bar{1}0)$  and  $(10\bar{1}0)$  lattice directions. This means that when the three layers superimpose after the border bending they will stack over the original three matching lattice positions and, eventually, preserving overall ABAB... stacking.

What is important for us is that in this case the bending, and therefore the apparent strain in the projected lattice image, will be only in one direction. The sample is therefore in a suitable configuration to test GPA 3D reconstruction. It is important to stress here that an hypothesis of 3D structure of the flake, as shown in the schematics of Fig. 4.6, can be made from basic knowledge of the material and from a careful inspection of HREM image itself (geometry, defocus variations, etc...). However, it is not possible in any way to *quantify* the surface height variation from a standard analysis of HREM image. In the next Section the methodology, to retrieve *directly* this information from the map of the strain, will be discussed.

### 4.3.3 GPA deformation reconstruction

The first step in GPA is the reconstruction of the phase displacement maps relative to at least two non collinear  $\mathbf{g}$  vectors. In the case of the flake under investigation we selected  $(01\bar{1}0)$ ,  $(10\bar{1}0)$  and  $(1\bar{1}00)$  reflections of the reciprocal lattice. Figure 4.7 shows the results of the reconstruction. To select the  $\tilde{H}_g(\mathbf{k})$  coefficients a numerical mask has been used, with an aperture corresponding to a final resolution of about  $0.5\text{ nm}$  in the reconstructed phase maps.

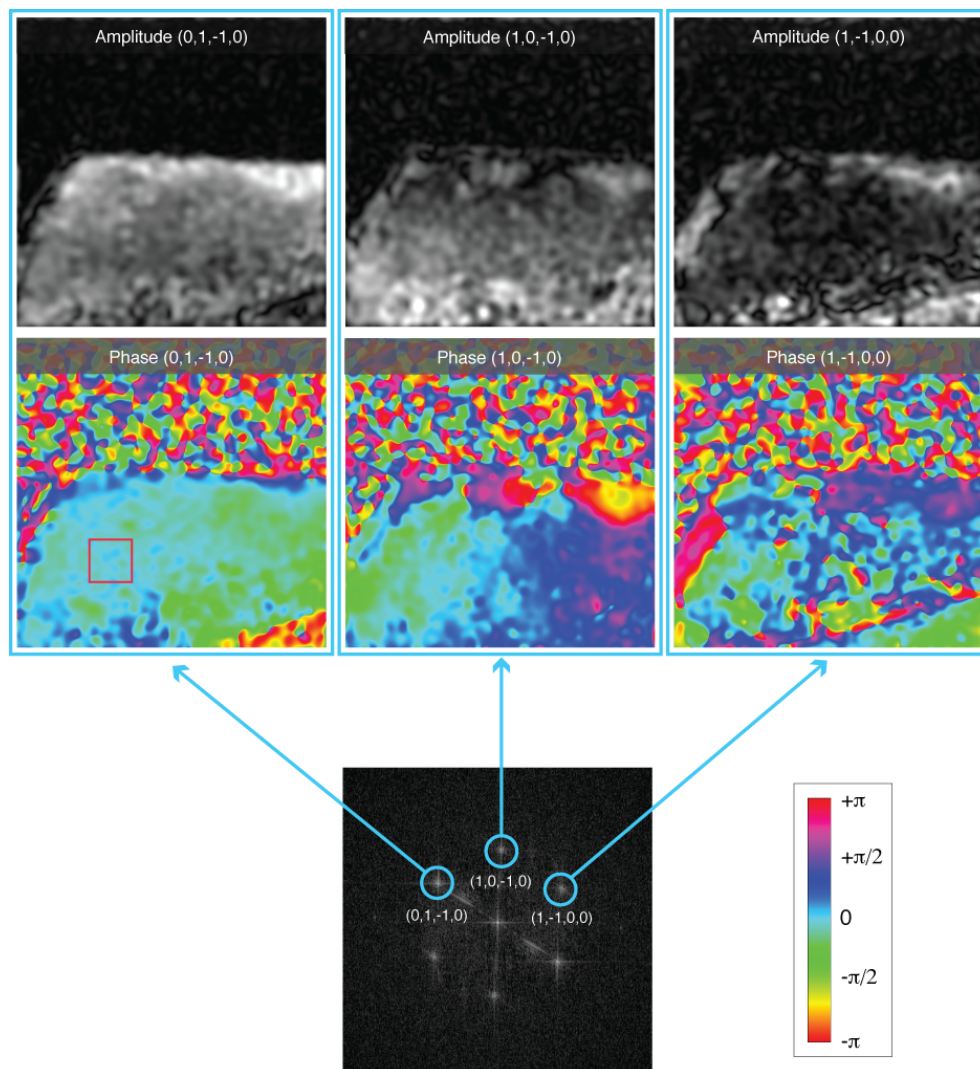


**Figure 4.7:** Reconstructed amplitude and phase maps for the graphite reflections indicated by blue circles in the FFT of the image of Fig. 4.2. Variations in the phase values are mapped with a color scale. Large phase variations are visible nearby the upper border in the reconstructed phase map from  $(1, 0, \bar{1}, 0)$   $g$  vector. Reference areas to re-normalize the phase backgrounds were taken in the regions corresponding to the one marked by the red rectangle in the  $(0, 1, \bar{1}, 0)$  phase map. The lateral dimension of the reconstructed phase maps is identical to that of the original HREM image ( $27.60 \text{ nm}$ ).

The first noticeable feature of phase maps of Fig. 4.7 is that large phase displacements can be seen in the  $(10\bar{1}0)$  direction, near the upper border. Figure 4.8 shows the phase map for the  $(10\bar{1}0)$  direction. Three triangular regions of significant phase displacement are aligned over the border and indicated by white

arrows. The right one is the larger one and the most intense. A slight phase displacement is noticeable in correspondence to these region in the  $(1\bar{1}00)$  direction also, while along the  $(01\bar{1}0)$  direction phase is almost flat all over the flake.

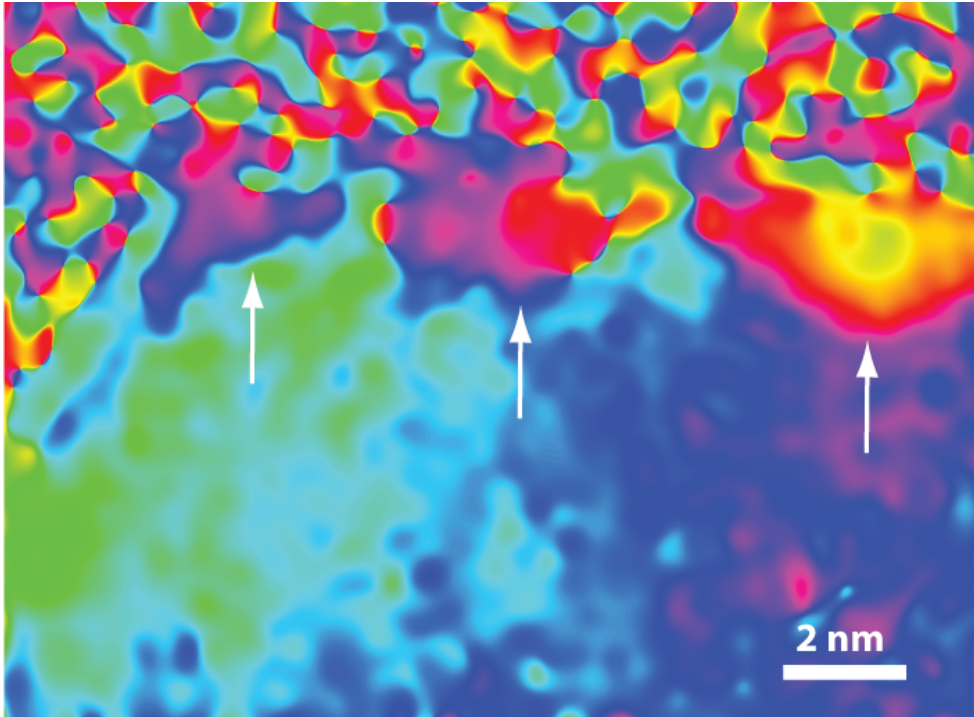


**Figure 4.8:** Phase map reconstructed for the  $(10\bar{1}0)$  direction. arrows indicated large phase variations at the border of the flake.

The apparent compression we are looking for is therefore acting displacing  $(10\bar{1}0)$  and  $(1\bar{1}00)$  fringes, leaving almost unmodified the  $(01\bar{1}0)$  direction. To calculate strain maps, we need to define a reference axis to project their components. A possible choice is the direction  $(2\bar{1}\bar{1}0)$ , assuming the flake is bended with a slope in that direction.

Figure 4.9 shows a close-up of the border region in HREM imaging and in the  $(10\bar{1}0)$  phase map. The plot of Fig. 4.9 c) is taken in the marked region and shows that a large phase variation is locally along the direction of  $(2\bar{1}\bar{1}0)$  lattice planes. We can make an hypothesis for the model of the atomic structure of the flake in this region as shown in d). According to the scheme of Fig. 4.6, three layers bend in the positive  $z$  direction while the other three bend in the opposite direction, creating

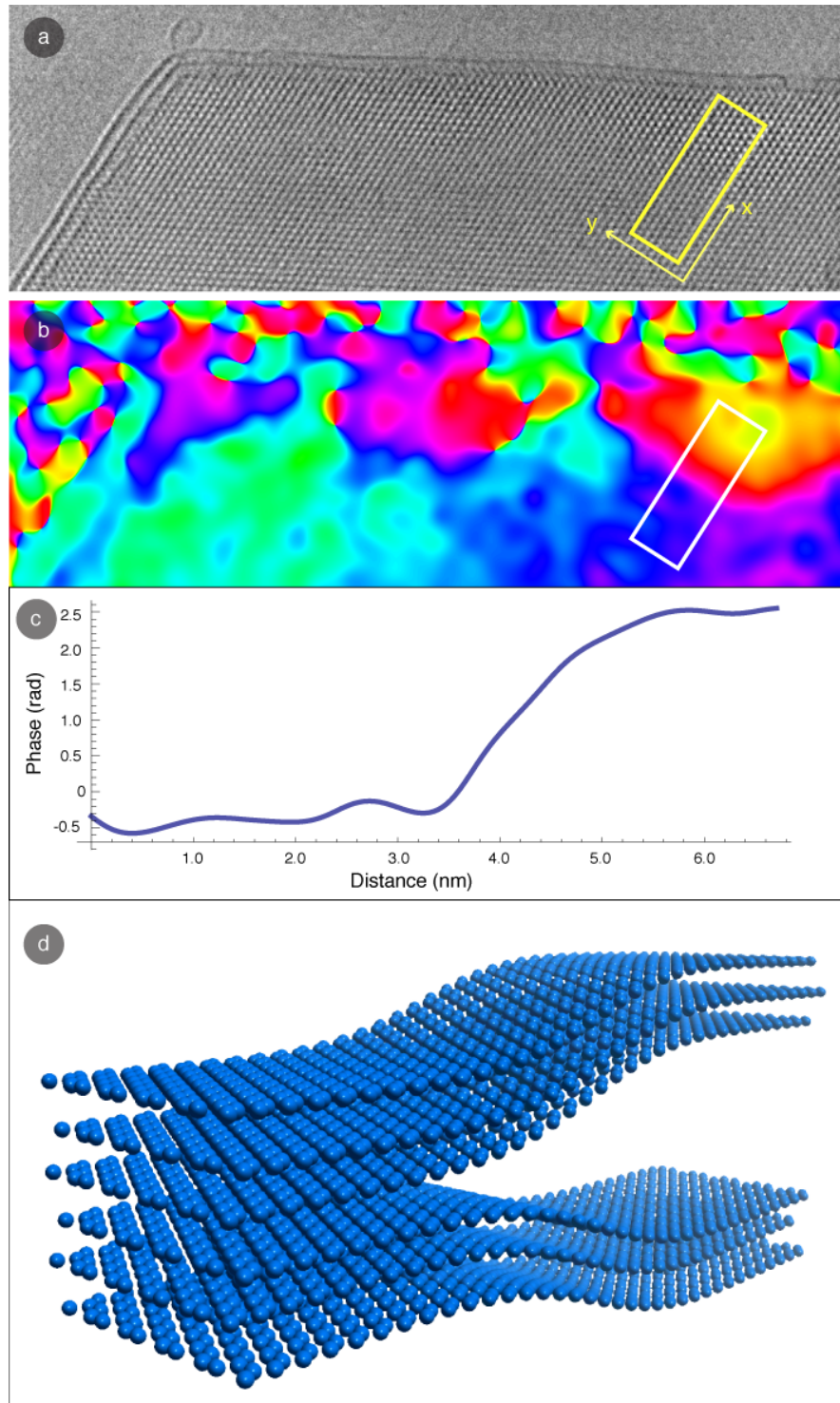


**Figure 4.9:** a) HREM image of the flake near the upper border. The region of interest (ROI) is marked by the rectangle and the cartesian reference system for further analysis is indicated. b) Corresponding region of the  $(01\bar{1}0)$  phase map. The same ROI of (a) is reported. c) Plot of the phase profile along the  $x$ -axis in the region of interest. d) Schematics of the atomic structure of the flake in the ROI.

a hollow space nearby the border curvature.

The calculated amplitude maps are generally slowly-varying, except for some localized regions for  $(1\bar{1}00)$  and  $(01\bar{1}0)$ . Between the large phase bumps of the  $(1\bar{1}00)$  map, localized contrast inversions will be like to generate artifacts during strain calculations [75]. The same problem is present in the marked region of  $(01\bar{1}0)$  amplitude map, nearby the left border. We will stay far from these regions during analysis of the calculated strain maps.

This structural hypothesis will be verified by calculating the strain field map choosing the cartesian reference system indicated in Fig. 4.9 a), i.e. with the  $x$ -axis in the  $(2\bar{1}\bar{1}0)$  direction. As already discussed, we need two phase maps calculated for two non collinear directions to recover the 2D strain field. Every couple of  $\mathbf{g}$  vectors is mathematically equivalent, so a good criterion will be to choose the couple resulting in the higher signal-to-noise-ratio. We checked different combinations and all the results were consistent. In the end, the best results have been obtained using the  $(01\bar{1}0)$  and the  $(10\bar{1}0)$  directions.

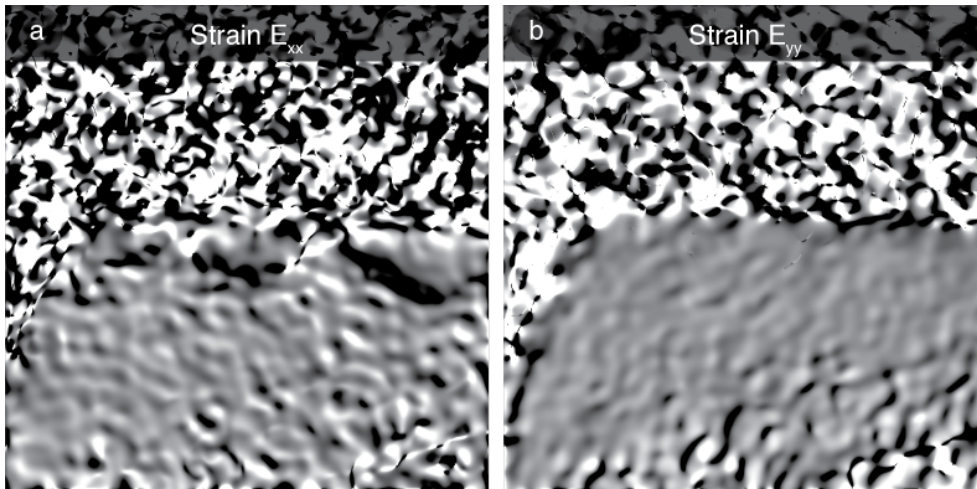


**Figure 4.10:** Calculated strain field maps. a) Components of the strain field along the  $(2\bar{1}\bar{1}0)$  x-direction and b) along the  $(01\bar{1}0)$  perpendicular y-direction.

Figure 4.10 shows the results for the strain maps  $\epsilon_{xx}$  and  $\epsilon_{yy}$ . They significantly more affected by noise than the phase images. This is due to the numerical process of calculating the derivative of the phase [78]. Nevertheless, the main features of the maps can be easily identified.

The central part of the flake is almost strain free in both the  $x$  and  $y$  components. Along the  $x$ -direction we recognize some strain change associated to the borders

of the three regions already noticed nearby the upper border. Consistently with the choice of the axes, the largest strain variation is associated to the zone highlighted in Figures 4.9 a) and b).

## 4.4 3D reconstruction

### 4.4.1 Modeling deformations

To recover the local deformation of the membranes from the strain maps we retrieve the local slope value from the measured strain. In the beginning of this chapter we discussed the effects of projection for a one-dimensional chain. To apply this very simple model to our case we need to find a zone where the apparent compression can be assumed to be along one direction only.

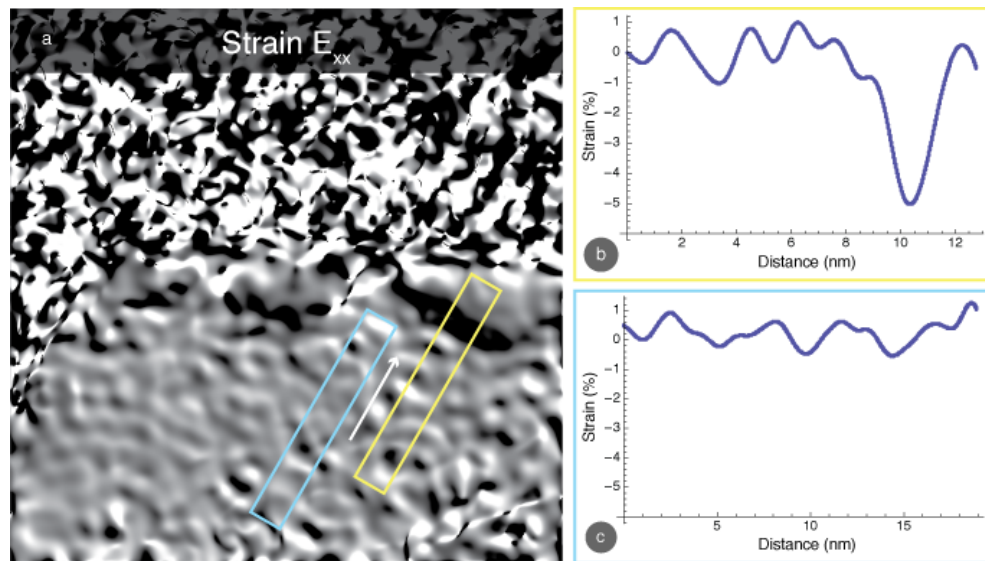


**Figure 4.11:** a) Calculated strain map  $E_{xx}$  in the  $(2\bar{1}\bar{1}0)$  direction. b) Profile of the strain intensity along the yellow ROI. c) Profile of the strain intensity for the blue ROI. Profiles are acquired in the direction indicated by the white arrow.

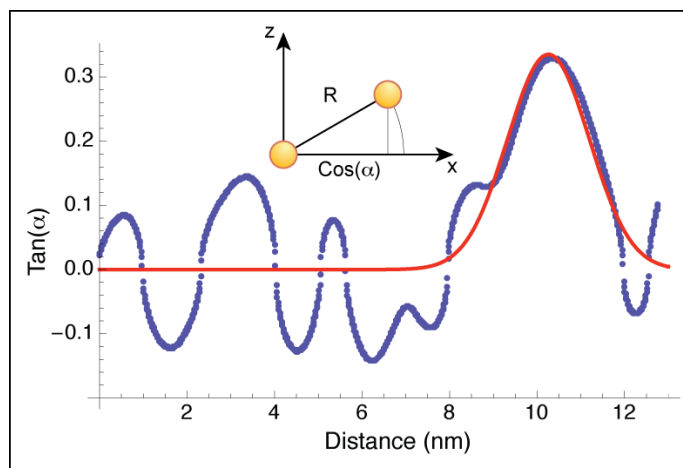
Recalling Figure 4.9, it is possible to identify a region showing a local uniaxial strain due to the geometric projection of the bended 3D atomic structure. The zone corresponds to the region marked with the yellow rectangle of Fig. 4.11 a). According to the one-dimensional model previously discussed, we should find the peak of the compression associated to the position of the curvature inversion point in the bended flake.

Fig. 4.11 b) shows the profile of the strain along the yellow rectangle. The plot indeed shows a localized peak in the strain corresponding to the middle region of the phase ramp of Fig. 4.9 c). The measured compression is about 5%. Such a value is extremely high for a pure mechanical in-plane compression of the crystal lattice.

As previously mentioned, graphene has a Young modulus of about 1 *TPa*. This would imply, for a 5% compression, a stress of about  $10^{28} \text{ N/nm}^2$ . Even if graphene should resist such a force without breaking the interatomic bonds, a compression like this would result in a three-dimensional deformation. Thus, once more, we consider that such a strain is apparent, and due to the effect of projection of the bended flake on the *xy*-plane.

The profile of the unstrained central area (blue rectangle of Fig. 4.11 (c)) allows us for an analysis of the noise of the image. The two plots of Fig. 4.11 are obtained using the same intensity scale to easily appreciate background oscillations. An average of the strain free area background shows noise oscillations of about 0.6%.

Such oscillations are mainly due to the poor contrast of the graphite fringes in the HREM image. This noise is amplified by the numerical calculations performed by the GPA to obtain the derivative maps, and it is the first limitation of this technique. Nevertheless, in this case, a relatively good signal-to-noise ratio, with a few percents strain, is still present.



**Figure 4.12:** Plot of the slope of the flake, calculated from the strain profile of Fig. 4.11 b). The red curve represent a gaussian fit of the data. In the inset a schematics of the geometry used to calculate the slope.

The next step will be the calculation, for each value of the position of the map, of a value for the slope of the surface of the flake. Simple trigonometry defines

immediately the local angle  $\alpha$  between the flake surface and the  $xy$ -plane in terms of the strain  $\epsilon$  as:

$$\cos(\alpha) = (1 - \epsilon) \quad (4.13)$$

From the value of alpha it is straightforward to calculate its tangent for each value of the strain. Fig. 4.12 shows the value of  $\tan \alpha$  for the region of the flake in Fig. 4.11 a). In the plot is superimposed the value of the calculated fit. In our simple model we decided to fit the tangent with a Gaussian type function, representing the peak at the center of the bend.

The calculus of the tangent makes sense only when the strain has negative values, corresponding to a compression. In the plot of the strain it is possible to notice that background oscillations due to noise varies from negative to positive values. Positive has no geometrical sense, but nonetheless they represent correctly the noise. Therefore we made the assumption of assigning negative slope value to these points, just to reflect the oscillatory behavior of noise around zero. From the plot of Fig. 4.12 it is clear that the signal is even more noisy and we can calculate a final signal-to-noise ratio of 3.

#### 4.4.2 Structure simulation

Reconstruction of the three-dimensional atomic structure of the graphite flake is straightforward from the fit of the local slope. The slope is the first derivative of the height displacement of the flake surface and a straight integration gives directly the atomic positions. Fig. 4.13 shows the results of the structure simulation.

In the inset of Fig. 4.13 a) is plotted the integrated height as a function of the distance, and the three dimensional model is calculated accordingly. Each stacked layer change its  $z$  position of about  $0.8 \text{ nm}$ , as indicated in the lateral projection of b).

To test the self-consistency of our methodology we simulated the resulting HREM image of the modeled structure, under the same imaging condition of the experimental image. Fig. 4.14 shows the results of the comparison between the experimental and simulated HREM image for the area in the rectangle of Fig. 4.9 a).

The simulation was performed using JEMS multi-slice algorithm. The atomic structure was sliced perpendicular to  $z$  into 30 planes and the interaction with the electron beam computed according to the previously described procedure. It is worth to notice that the flake is continuously undulated. There is no region completely flat and parallel to the  $xy$ -plane and the overall structure is no more centrosymmetric.

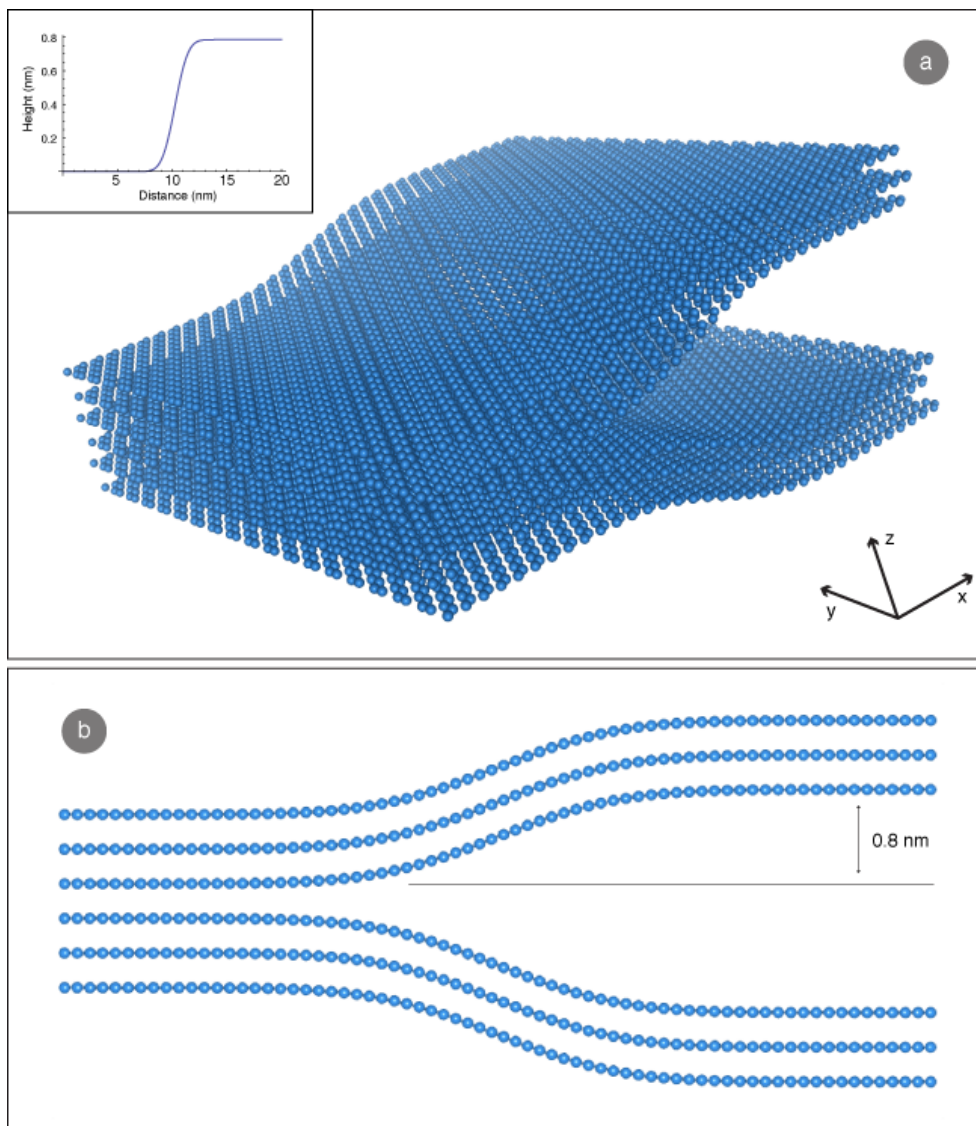


**Figure 4.13:** Schematics of the reconstructed structure of the flake. a) Perspective view. In the inset a plot of the elevation of each graphene layer. b) Lateral view of the structure.

The first important feature to notice in Fig. 4.14 is that the trend in the contrast variation of the experimental image is qualitatively reproduced by the simulation. As discussed above a contrast modulation is expected due to the different height of the regions of the flake.

Comparison of intensity between experimental and simulated HREM images can only be qualitative. Quantitative agreement is well known to be impossible due to too many unknown effects intrinsic in the digital recording of electron images

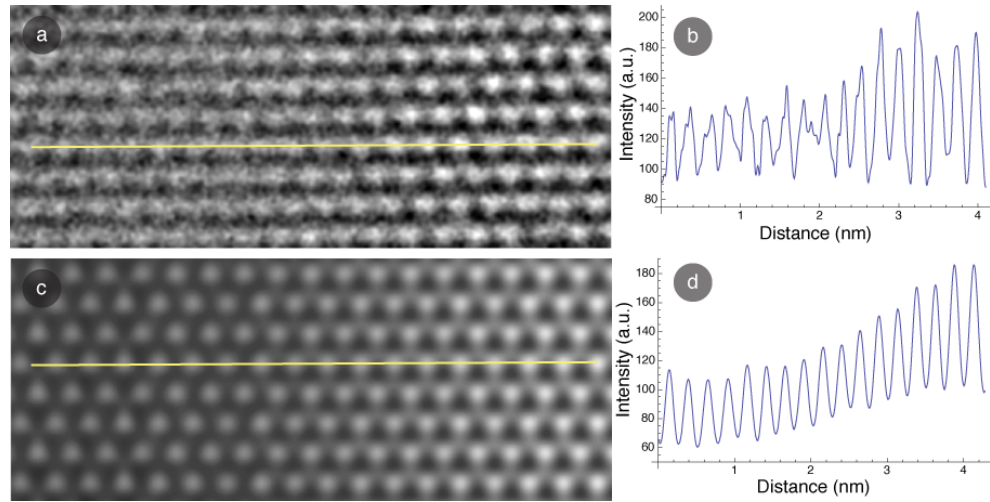


**Figure 4.14:** Comparison of the contrast between experimental and simulated HREM images. a) Experimental image in the ROI of Fig. 4.9 (a): left part of the image corresponds to the region where the six layers are superimposed; on the right part the height has changed and there is a hollow space in the middle flake (see 4.9 (d)). b) Intensity profile along the yellow line. c) Simulated HREM image. d) Intensity profile along the yellow line in the simulated image.

[79]. Nevertheless, the increasing contrast trend from regions where the six layers are stacked (left in the HREM image) and the elevated part (right) is clearly visible in the plots of Fig. 4.14 b) and d).

### 4.4.3 Discussion of the results

The final check of the proposed approach was done by applying GPA on the simulated image, to compare calculated strain with the experimental one. Fig. 4.15 shows the results of GPA strain calculation over the simulated HREM image. Fig. 4.15 a) shows the HREM map, where the flake slope increase from left to right, with the flex point in the middle of the image. Fig. 4.15 b) shows the calculated strain map.

The parameters for the GPA reconstruction are the same used for the analysis of the experimental image previously shown. The direction of the reference  $x$ -axis of the strain field is the  $(2\bar{1}\bar{1}0)$ . In the simulated image shown in Fig. 4.15 a) this direction corresponds to the horizontal axis.

The strain profile acquired for the map of Fig. 4.15 b), has been plotted in c) superimposed to the experimental one. The two profile show excellent agreement, confirming that the structure was faithfully reproduced in the simulation. Some oscillations in the profile from the simulated image are due to artifacts induced by

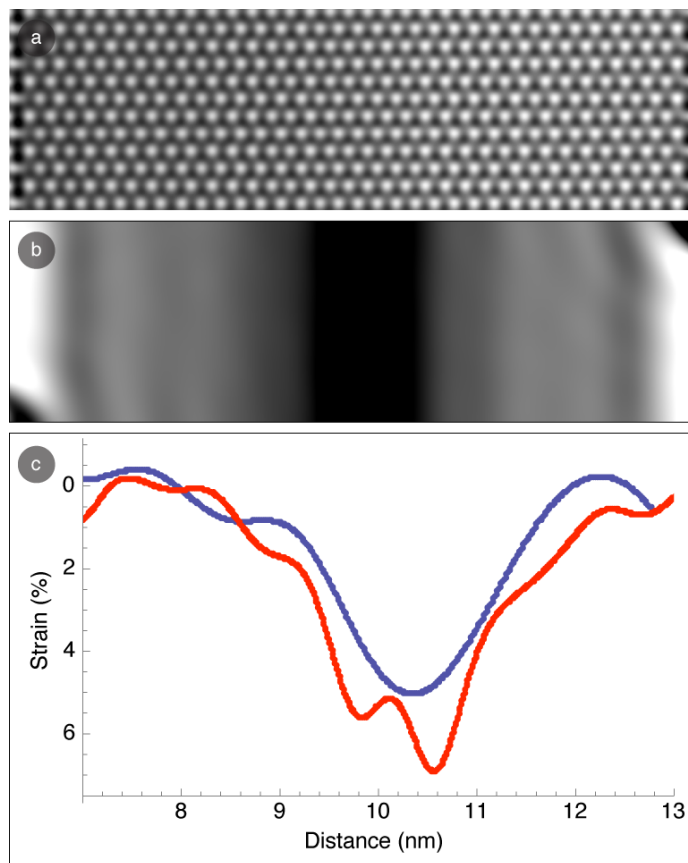


**Figure 4.15:** a) HREM image simulation of the reconstructed structure. b) Calculated strain map with the same parameters of the experimental one. c) Plot of the strain profile from the simulated strain map (red curve) and of the experimental one (blue curve).

the finite slices thickness used for the simulation.

The sensitivity in height variations of the method proposed, is set by the noise in the calculated strain maps, which is, ultimately, inversely proportional to the contrast of the HREM fringes in the experimental image. HREM simulations provides a high contrast, which can never be obtained in experimental micrographs. 3D reconstruction was performed successfully over simulated height variations of  $0.2 \text{ nm}$  over a distance of  $4 \text{ nm}$ . On experimental HREM images, it is therefore reasonable to expect that height variations of about  $0.4 \text{ nm}$ , over similar distances, will represent the current limit in the sensitivity of this technique.

## Conclusions

In this chapter, a novel methodology for the 3D reconstruction of the waviness of a 2D crystal membrane has been presented. Unlike other available TEM reconstruction methodologies, like tomography, this one requires processing of a single HREM micrograph. The reconstruction procedure relies on the analysis of the geometrical distortions present in the fringe system composing the HREM image of a waved crystal. Using GPA, a complete map of these distortions can be retrieved, with sub-nanometric lateral resolution. 3D crystal deformation will be directly reconstructed from apparent inter-planar distances modifications.

This work is motivated by the challenge of understanding the relation between the 3D structure of graphene membranes and their extraordinary electronic properties. The intrinsic undulations of 2D crystal membranes are expected to have a profound effect on the electric properties of this material, inducing localized electro-magnetic potentials acting as long-range scatterers for the charge carriers.

The proposed technique promises to be a valuable instrument in the 3D reconstruction of 2D graphene membranes and FGC flakes. For these materials, other nanoscale 3D reconstruction techniques like STEM tomography, are limited by the intrinsic geometry of these samples. The proposed method enables simultaneous HREM imaging of the structure and its 3D reconstruction, with high spatial resolution and sub-nanometric height resolution.

The preliminary research assessed the reliability of the reconstruction technique testing the methodology on the simple case study of a FGC flake. The surface height variation of  $0.8 \text{ nm}$  nearby a folded edge of the crystal has been successfully reconstructed. The direction of future research will be to use the proposed technique to map the expected waviness of an individual graphene crystal, combining three-dimensional structural information retrieved, with local probing of the electronic properties by means of electron holography.



# **GRAPHENE MEMBRANES AS NANOSCOPIC TANGENTIAL SIEVES**

Read the directions and directly you  
will be directed in the right  
direction.

*(Lewis Carroll, "Alice in  
Wonderland")*

## Introduction

In the first chapter of this manuscript I discussed how the different orientation of the lattice in SWCNTs dramatically affects their electronic properties. SWCNTs chirality determines whether the tube is metallic or semiconducting. Thus, especially for electronic applications, it is crucial to find a way to select either metallic or semiconducting SWCNTs out of a mix of different chiralities.

The most natural way to accomplish this task would be to control growth during the synthesis of the tubes. Unfortunately, current techniques produce a mixture of tubes with different chiral indexes. It has been suggested that the control over the structure of the resulting tube can be achieved by controlling the interaction between the growing carbon caps and the catalytic cluster [80]. Unfortunately CNTs growth depends on too many experimental parameters, like carbon precursor type, ambient growth conditions, type of catalyst used and the kind of substrate employed [81]. An atomic level control during the growth is therefore far from being achieved.

For all of the above reasons, and the relative simplicity of producing large quantity of mixed tubes, chirality control and selection are more commonly addressed in post-grown. A large quantity of works is coming out, presenting different approaches for an effective control of the chirality. These methods can be divided according to two main strategies: the elimination (partial or total) of tubes with specific chirality or the selection of only one family of tubes from a solution. Eliminating tubes of specific chirality from a mixture can be performed either by selective oxidation or by heating up specific tubes using radiation of a particular wavelength to match resonances in specific SWCNTs [82, 83].

A different approach investigates the specific interaction between SWCNTs and the atomic structure of poly-aromatic molecule. Under certain relative orientations both the lattice of SWCNTs and the one of those molecules are commensurable. In fact, SWCNTs tend to be selectively locked to a specific molecule, if there is a match in the two lattice orientations. A successive treatment will remove all the tubes that did not locked [84].

In our researches, following the above approach, we investigate the locking of SWCNTs to the biggest aromatic molecule: graphene. This Chapter will presents the experimental details of the experiment performed. Shortened tubes has been deposited over the surface of FGCs, and the mixture analyzed using TEM. A combination of electron diffraction and HREM imaging has been used to verify the relative lattices orientation between tubes and the underlying FGC.

## 5.1 Alignment of SWCNT over FLG

### 5.1.1 Samples preparation

SWCNTs and graphene lattice matching involves only the surface of these structures. For this reason in this experiment, we did not need true single-layer graphene membranes. We will use the surface layer exposed by each thin graphite flake, independently of its thickness. The only requirement was to obtain electron transparent flakes for imaging with TEM.

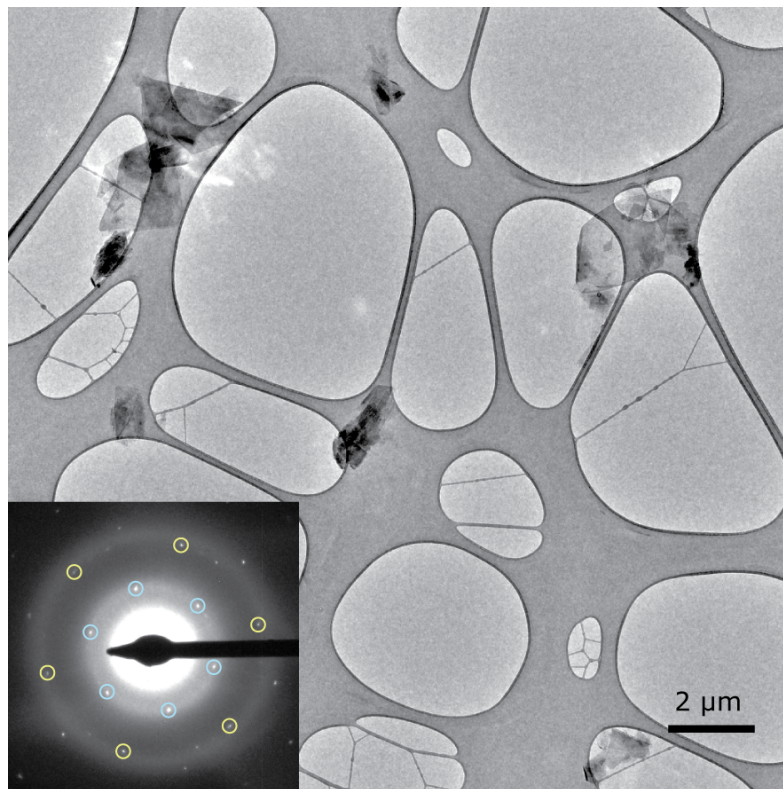
Natural graphite powder was then mechanically exfoliated by means of a jade mortar and a pestle. Grain size is reduced slowly but gently using this procedure, without fragmenting the flakes. Adding few drops of isopropanol and grinding for 30 minutes the dense paste so-obtained produces large, defect-free thin flakes, of few microns in dimension.

Figure 5.1 shows a representative view of the dispersion of the flakes over a standard holey carbon TEM grid. To disperse the flake the ground graphite was suspended in isopropanol with the aid of sonication for 15 minutes, process that also provide additional exfoliation of the flakes. Suspended large and thick graphite pieces were sedimented using centrifugation.

We have to underline that the method used is not valuable for the synthesis of large graphene crystals. According to Coleman's work [39], isopropanol and/or ethanol are not suitable solvents to induce an effective exfoliation with the only aid of ultrasonic agitation. The only single-layer crystallites were found lying over the amorphous carbon film and their dimension did not exceed  $\sim 100$  nm. Nevertheless this method results to be suitable for the production of FLG flakes for TEM characterization.

The borders of the dispersed flakes are mostly constituted by really thin FLG membranes, which can provide a suitable substrate to deposit SWCNTs. As shown in Figure 5.2, the analysis of the border of the flakes reveals the number of layer, which were nine in this case. Those will be the zones of interest when SWCNTs will be later deposited.

SWCNT were produced by arc-discharge method and used as provided by the commercial supplier. Arc-discharge synthesis is well known to produce highly ordered crystalline SWCNT, with a broad range of chiral angles distribution. Figure 5.3 shows the pristine tubes as they are simply dispersed from powder form in isopropanol with aid of mild sonication.



**Figure 5.1:** TEM image of the produced thin FLG flakes as dispersed over a standard 3 mm TEM copper grid covered by a perforated amorphous carbon membrane. FLG flakes are the lighter, and graphene edges can be found at their borders. Average flake dimension is about few microns and with usually tens of graphene layers.

It is known that highly energetic and long lasting (several hours) sonication of SWCNT in almost any liquid medium produces a shortening of the tube length. Due to agitation the tubes boucle and fragment. We used this method to produce extremely short SWCNTs. The small longitudinal dimension of the fragments reduce the energy necessary for them to possibly accommodate to the underlying graphene network once dispersed over graphene flakes.

The suspension of shortened nanotubes was gently centrifuged to remove larger bundles and catalyst particles residues. Part of the lighter solution was used to wet graphite powder during grinding (instead of pure isopropanol), the remaining was used to suspend ground graphite. As described above for FLG suspension, the resulting suspension of graphite and tubes undergoes an additional step of centrifuge to remove larger graphite particles. Drop-casting over standard holey carbon film grids concludes sample preparation, now ready for TEM investigation.

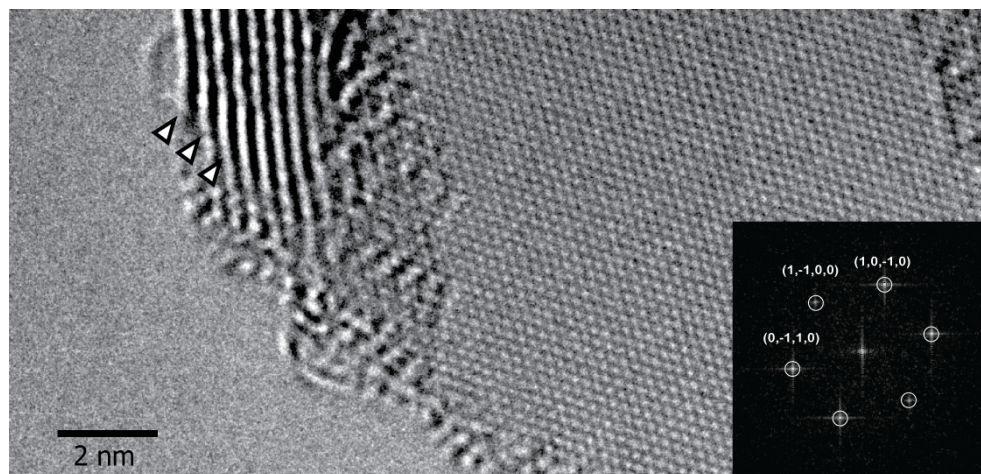


**Figure 5.2:** TEM HREM micrograph showing the border of the deposited flakes. (Inset) FFT of the TEM micrograph, where some honeycomb lattice directions indicated. HREM allows, in this case, to count the number of folded layers by counting (0002) lattice fringes, as indicated by arrows.

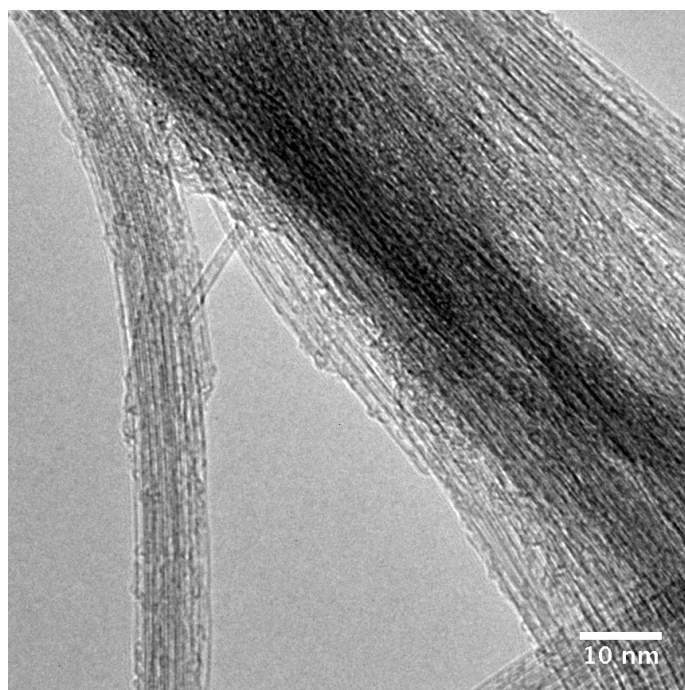


**Figure 5.3:** TEM micrograph showing the dispersion of bundles of SWCNT before shortening sonication. SWCNTs stick together to form bundles. Nanotubes surface is often covered by amorphous carbon impurities.

### 5.1.2 Electron diffraction investigation

The electron diffraction patterns were acquired with the energy of the electron beam lowered to  $80\text{ keV}$ , in order to prevent structural modifications during the observation. Electron diffraction patterns were acquired using either a Philips CM20FEG or a FEI Tecnai F20 TEM. The area of the sample illuminated uniformly with a parallel beam of electrons in electron diffraction had a diameter of few hundreds nanometers in both microscopes.

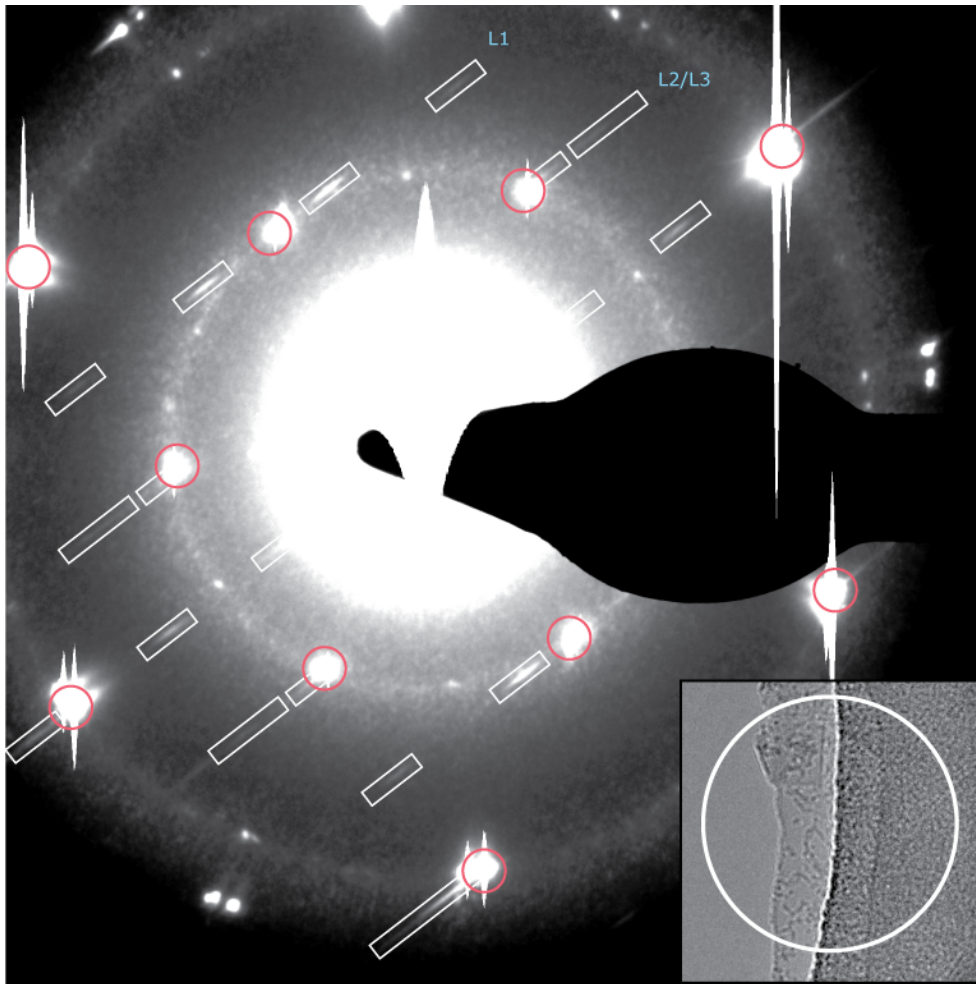


**Figure 5.4:** Electron diffraction pattern acquired using nanoarea diffraction over the tip of a graphite flake. In the inset illuminated region of the flake. Striking in ED pattern is due to oversaturated graphite reflections to show the feeble CNTs spots. Intensity modulations due to SWCNTs were highlighted (rectangles) as well as the graphite reflections along which they are aligned (circles).

Figure 5.4 shows one of the electron diffraction patterns obtained. The inset shows a TEM micrograph of the flake under investigation and the circle marks the area illuminated by the electron beam to acquire the diffraction pattern. In the pattern, the hexagonal of spots of the honeycomb lattice are clearly visible and a set has been highlighted with red circles. The flake was folded over itself and the superimposed honeycomb lattice with a different orientation originates the other set of lighter spots visible in the pattern.

The diffraction pattern has been intentionally over-exposed to increase visibility of the lighter features. White rectangles in Fig. 5.4 highlight a series of intensity modulated features aligned along parallel lines. This pattern has striking similarities with the electron diffraction pattern of a carbon nanotube, as shown in Fig. 2.16. The superposition of layer lines  $L_2$  and  $L_3$  determines a rolling angle  $\alpha = 0^\circ$  and the structure is therefore zig-zag.

The pattern highlighted by the white rectangles presents some differences with the simulated one of an individual SWCNT shown in Fig. 2.16 or the experimental one of Fig. 2.18. The spacing between the features along each line is inversely proportional to the diameter of the tube. In this case the periodicity is not present and the pattern is more compatible with the superposition of intensities from different tubes, all with the same lattice orientation but different diameters.

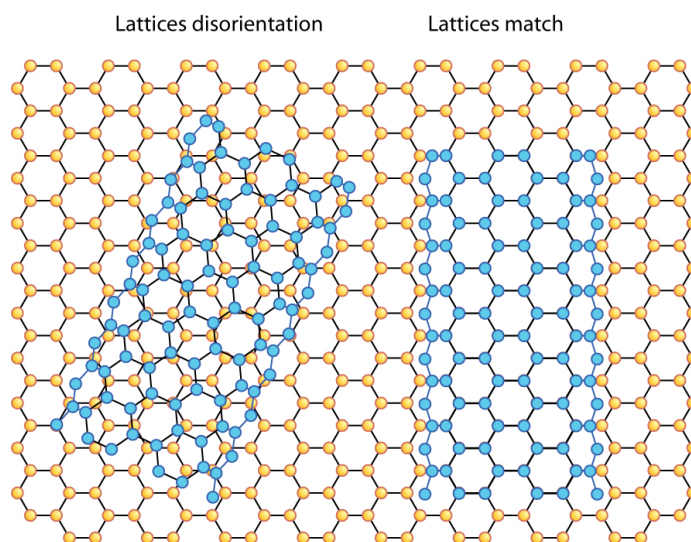


**Figure 5.5:** Schematics of two zig-zag tubes sitting on the surface of a FGC. The axis of the tube on the left is disoriented with respect to the underlying honeycomb lattice, while the right one lattice perfectly match the orientation of the FGC one.

It is remarkable that the pattern of the tubes is perfectly aligned with the hexagonal honeycomb pattern marked by the red circles. The axis of the tubes are oriented along the  $(2, -1, -1, 0)$  vector of the FGC reciprocal lattice. Figure 5.5 shows a schematic of the lattice orientation of a zig-zag tube with respect to the surface of a FGC. The tube on the left is disoriented with respect to the underlying lattice while the positions of the atoms of the right one match perfectly that of the FGC surface. When such a lattice match is verified, the orientation of the diffraction patterns will correspond to that that observed in Fig. 5.4.

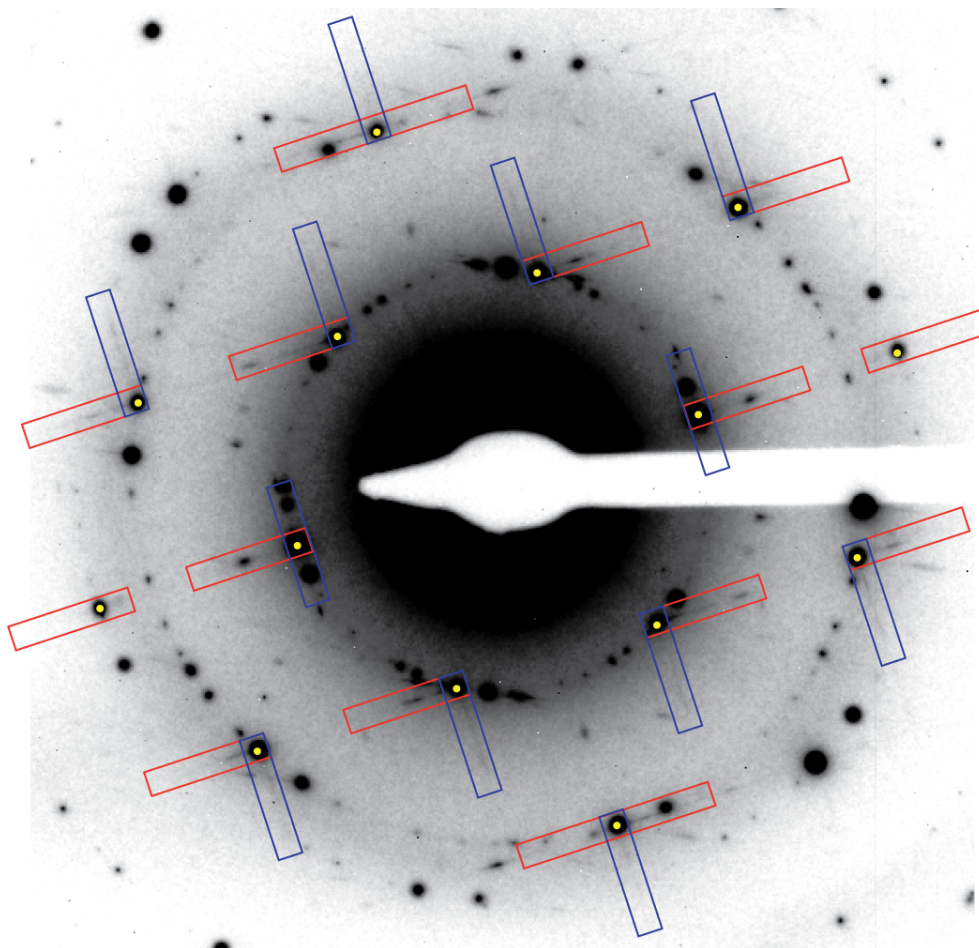


**Figure 5.6:** Electron diffraction pattern of a aligned CNTs over graphite. (Intensity has been inverted for displaying purposes) Intensity has been inverted. There is evidence of SWCNTs diffraction patterns crossing at  $90^\circ$ . Red rectangles Highlighted diffraction pattern of armchair tubes, while blue rectangles mark diffraction pattern from zig-zag tubes. Both diffraction patterns from tubes are aligned to the same underlying pattern from graphite marked by the yellow circles.

A similar perfect match between lattice orientations is expected in the case of the armchair nanotube. Figure 5.6 shows the electron diffraction pattern obtained from a different FGC flake. Blue rectangles highlight areas of the pattern where there are intensity strikes, as the ones in Fig. 5.4, originating from a zig-zag collection of tubes of different diameters. In the pattern multiple series of intensity strikes are present. Areas marked in red corresponds to the diffraction pattern of a collection of armchair tubes. Both the patterns are aligned to the same honeycomb reflections marked by the yellow circles.

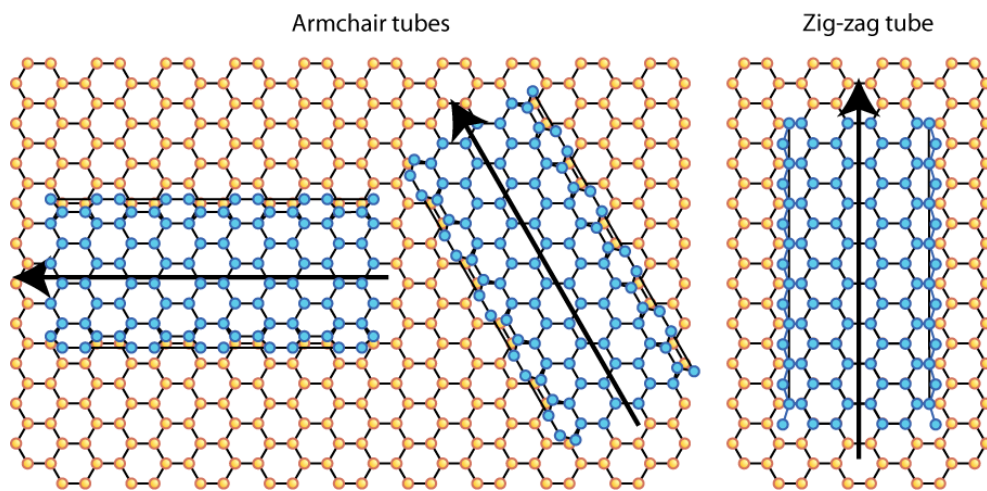


**Figure 5.7:** Schematics of an armchair (left) and a zigzag (right) tube matching the underlying FGC lattice. Arrows indicate the direction of the tubes axis. With respect to the direction of the zig-zag tube, the axis of the arm-chair matching the underlying lattice can form angle of either  $30^\circ$  or  $90^\circ$ .

An interesting feature is that the pattern from armchair tubes is rotated by  $90^\circ$  with respect to the one from zig-zag. If the two types of tubes are oriented matching the same underlying lattice of the FGC, due to the different chiral angle of the two structures, the axis of zig-zag tubes will be rotated by either  $30^\circ$  or  $90^\circ$  with respect to that of armchair ones. Figure 5.7 shows a schematics of the relative orientation of armchair and zig-zag tubes, when both structures lattices match the direction of the underlying FGC lattice. When both tubes are oriented, the right arrows indicating the direction of tubes axis are rotated by either  $30^\circ$  or  $90^\circ$ .

Electron diffraction patterns refers to a relatively large area of the flakes, as the electron beam illuminates over an area of several hundreds of nanometers. The electron diffraction patterns of Fig. 5.4 and Fig. 5.6 provide the evidence that multiple zig-zag and armchair SWCNTs are present over the surface of the flakes

and that those tubes are aligned with respect to the lattice of the flakes. From the diffraction pattern there is no evidence of chiral tubes, as if they were effectively eliminated from the surface of the FGCs.

### 5.1.3 HREM imaging

The same samples were also investigated on a local scale by using HREM. The HREM micrograph of the samples showed a dispersion of very short tubes over the electron transparent graphite membranes. Figure 5.8 shows HREM images of short SWCNT over the surface of a FGC. a) shows a tube of  $1.6\text{ nm}$  of diameter and with a length of  $\sim 12\text{ nm}$ .

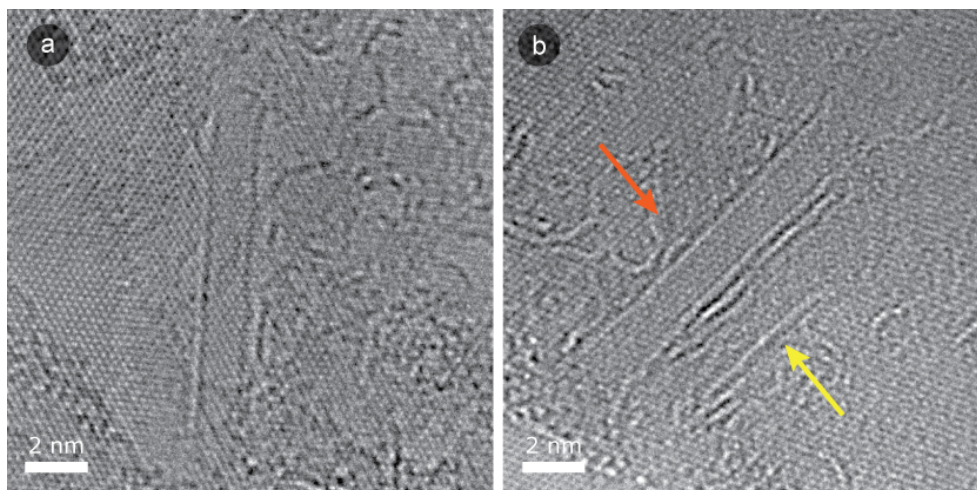


**Figure 5.8:** HREM image of two shortened single-walled carbon nanotubes. Tube length usually of several microns, is, as an example, reduced down to few nanometers. a) HREM image of a short nanotube of  $12.5\text{ nm}$ . b) Two small nanotubes side by side. The bigger one, indicated by a red arrow, is long approximately  $10.7\text{ nm}$  while the smaller (yellow arrow), very damaged and defective, is just  $\sim 4\text{ nm}$ .

Tubes length is reduced by the sonication cutting procedure. This procedure, however, is quite crude and the tubes are often badly damaged. Figure 5.8 b) shows two small fragments of SWCNT, the one indicated by the red arrow is approximately  $10\text{ nm}$  long, while the smaller one, indicated by the yellow arrow is just  $4\text{ nm}$ . Both the tubes have open caps and the area nearby both ends is irregular and highly defective.

Using HREM, a direct visualization of the lattice orientation between individual SWCNTs and the underlying FGC is possible. Figure 5.9 a) shows the experimental HREM image of two zig-zag tubes. The tubes run parallel to the folded border of

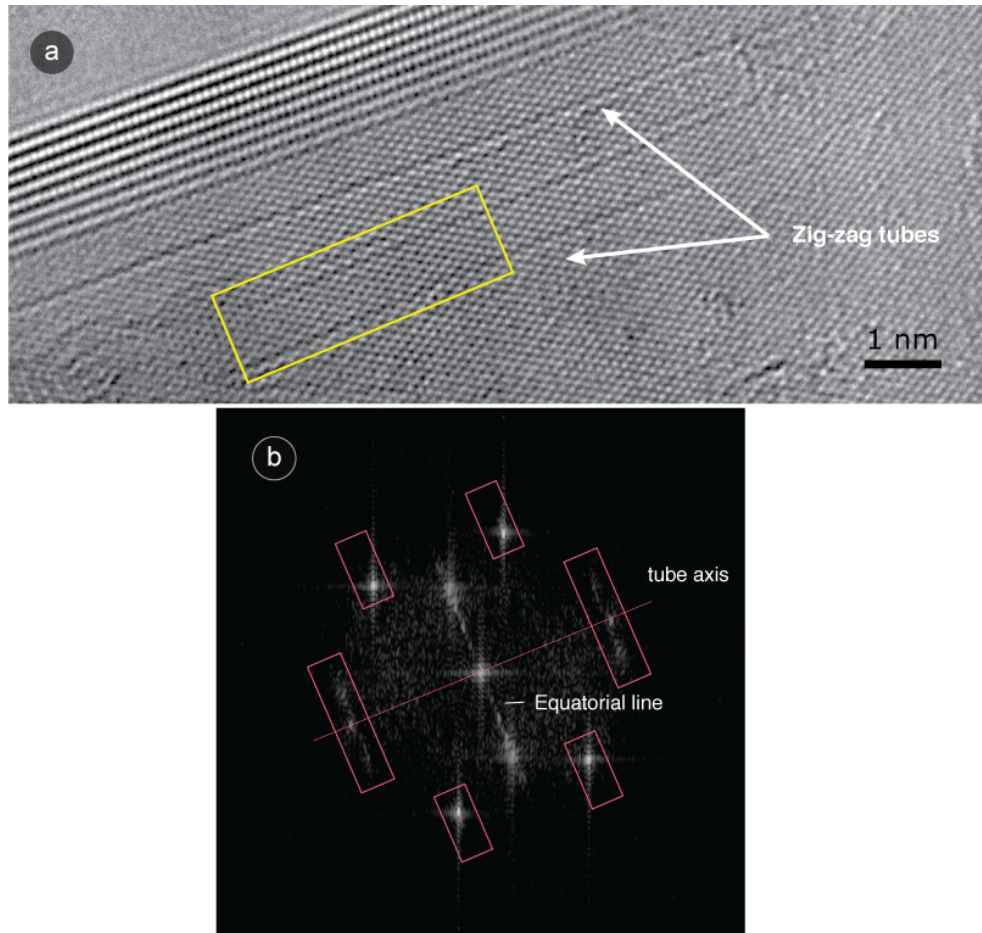


**Figure 5.9:** HREM image of two aligned zigzag carbon nanotubes. a) HREM image of the two tubes near a folded border of the graphite flake. b) FFT of the lower tube showing the alignment of the tube structure along the honeycomb lattice.

the FLG flake. They have similar diameter and both are perfectly aligned along the direction of the honeycomb lattice.

Figure 5.9 b) shows the FFT of the region in the yellow rectangle. In the spectrum, the modulated intensity along lines (regions marked by red rectangles), and the presence of an equatorial line are specific features of the curvature of the lattice of the tube, and the geometry of the pattern corresponds to that of a zig-zag tube. The alignment of the layer lines with respect to the hexagonal pattern from the honeycomb lattice of the FGC confirms that tube lattice orientation match the one of the underlying FGC.

Figure 5.10 shows another example of aligned SWCNTs. In the HREM

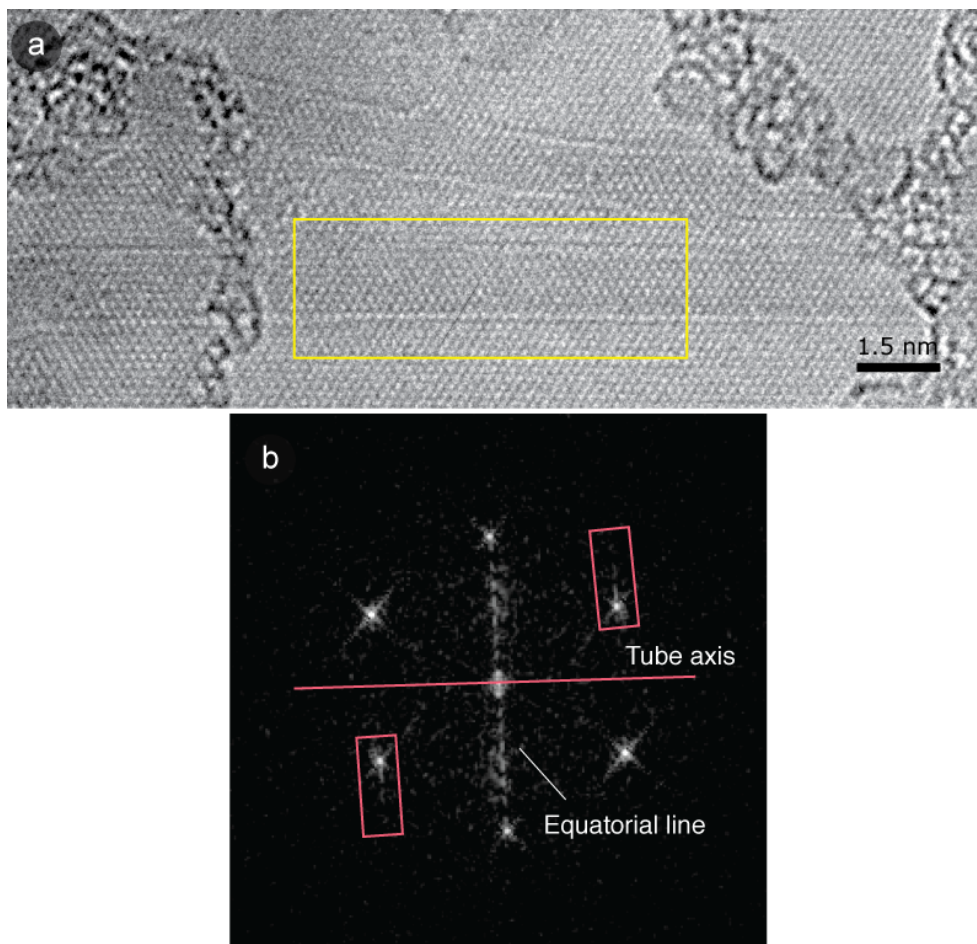


**Figure 5.10:** HREM image of two armchair carbon nanotubes. a) HREM image of the two tubes. The tubes are both aligned to the underlying honeycomb lattice. b) FFT of the lower tube region, showing the alignment of the tube structure along the honeycomb lattice.

micrograph of Fig. 5.10 a) two armchair tubes are visible sitting on the surface of a FGC. The upper one in the image is partially bended to continue parallel to the lower one. Fig. 5.10 b) shows the FFT of the region of the image corresponding to the yellow rectangle. Low contrast in the HREM image reflects in the low contrast of FFT spots. Nonetheless specific features of the non-chiral structure of armchair reflections are clearly visible and marked by red rectangles. The tube axis, indicated by the red line in the image, is perfectly oriented with respect to the underlying FGC lattice.

We run an extensive investigation of the samples combining electron diffraction and HREM imaging. Almost all tubes found were either zig-zag or armchair and aligned with graphite surface. Figure 5.11 a) shows the HREM image of one of the

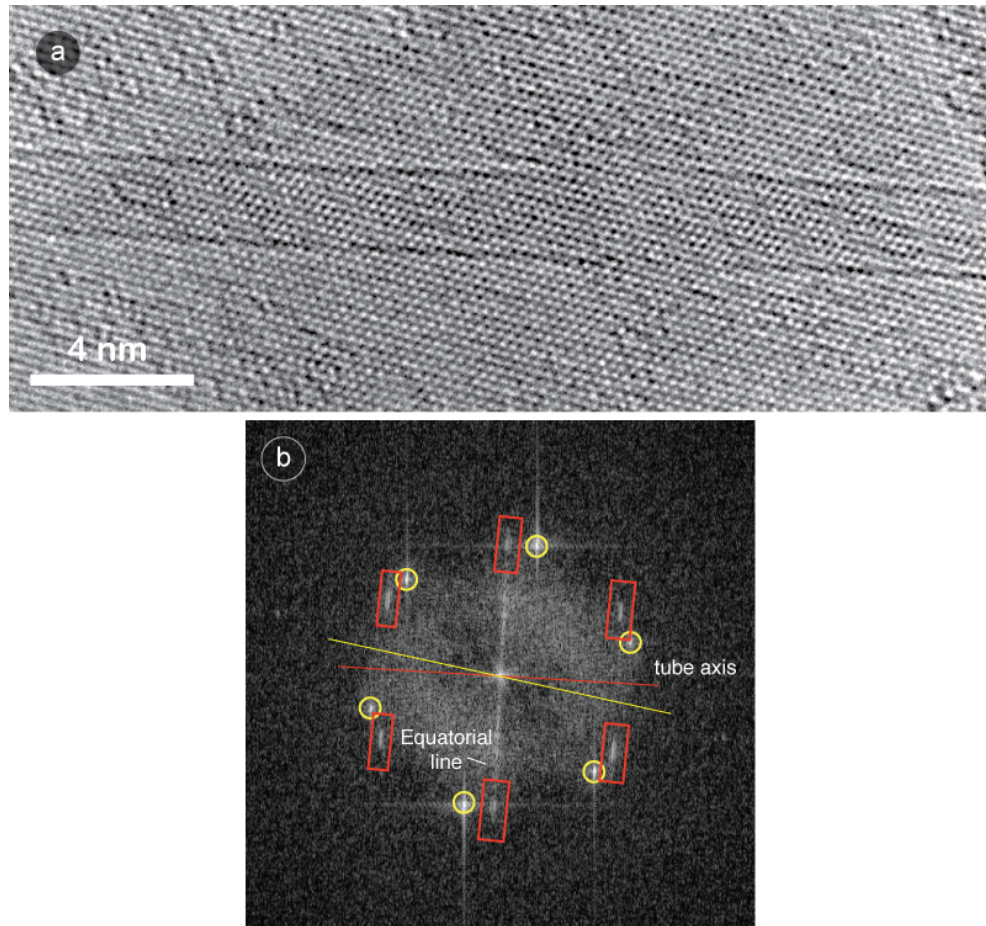


**Figure 5.11:** (a) HREM image of armchair tube over graphite. There is a misalignment of  $\sim 14^\circ$  between the tube axis and the underlying graphene network. (b) FFT of the image, showing hexagonal pattern from graphene lattice (yellow circles) and elongated spots of armchair tube (red rectangles). The tube axis is marked in red, while the relative orientation of the honeycomb pattern in yellow.

few tubes not oriented, while b) shows the FFT of the imaged region. In the spectrum, the pattern of the tube is highlighted by red rectangles, and its geometry corresponds to that of a armchair one. The axis of the tube (red) is rotated by about  $14^\circ$  with respect to the orientation of perfect match with the hexagonal pattern from the FGC lattice (in yellow the direction of the  $g = (2, \bar{1}, \bar{1}, 0)$ ).

Besides being an example of a tube disoriented with respect to the FGC surface, the SWCNT of Figure 5.11 allows to verify that the signal from the lattice of the tubes and that of the FGC both contributes to the pattern of HREM image. In the spectrum of the HREM images of perfectly oriented tubes and graphene, the hexagonal pattern

of strike features of the tube is perfectly superimposed to the spots of the underlying lattice. In this case it is clear that two distinct set of pattern are present.

## 5.2 FGCs acting as tangential nano-sieves for SWCNTs

### 5.2.1 Nanoscopic tangential sieves

In the experiment performed we investigated with HREM 31 tubes lying on the surface of a FGC. In most of the cases the tubes were superimposed to relatively thick parts of the flakes, where the elevated number of layers in the crystal made almost impossible to distinguish in the HREM image the features originating from the tubes lattice. Moreover, in many cases the flake was folded and scrolled several times and several hexagonal patterns of graphene reflection were present with different orientations in the FFT spectrum of the image. In these cases it was impossible to determine the relative orientation of the tube lattice.

Only few tubes, eleven, were lying over a a single crystal domain orientation and only for those we proceeded to determine their relative orientation. Among these 11 tubes, 7 resulted to be zig-zag, matching the direction of the FGC lattice; 2 tubes were of armchair type and oriented with the underlying lattice; only 1 was an armchair not oriented with the lattice of the FGC flake (the one of Fig. 5.11).

We found only 1 chiral tube lying on the flakes. Figure 5.12 shows this chiral tube; a) shows the experimental HREM image, while b) shows the FFT spectrum of the area imaged. Unfortunately uncertainty in the determination of the distances between the layer lines in the spectrum did not permit to determine the chiral indexes of this tube.

The combination of electron diffraction and HREM analysis provides the evidence for the surface of the flake to act as an effective selector for the non chiral zig-zag and armchair tubes. We observed that almost only those tubes without helical lattices remain grafted to the surface of the flakes after the sonication procedure of sample preparation. The results envisage the exploitation of the plain surface of FGCs therefore to be used as an effective tangential nano-sieve to select non helical tubes.

### 5.2.2 Graphene nano-tribology

The interaction between two bodies is ultimately regulated by the interactions between atoms. The arrangement of atoms between the interacting surfaces strongly

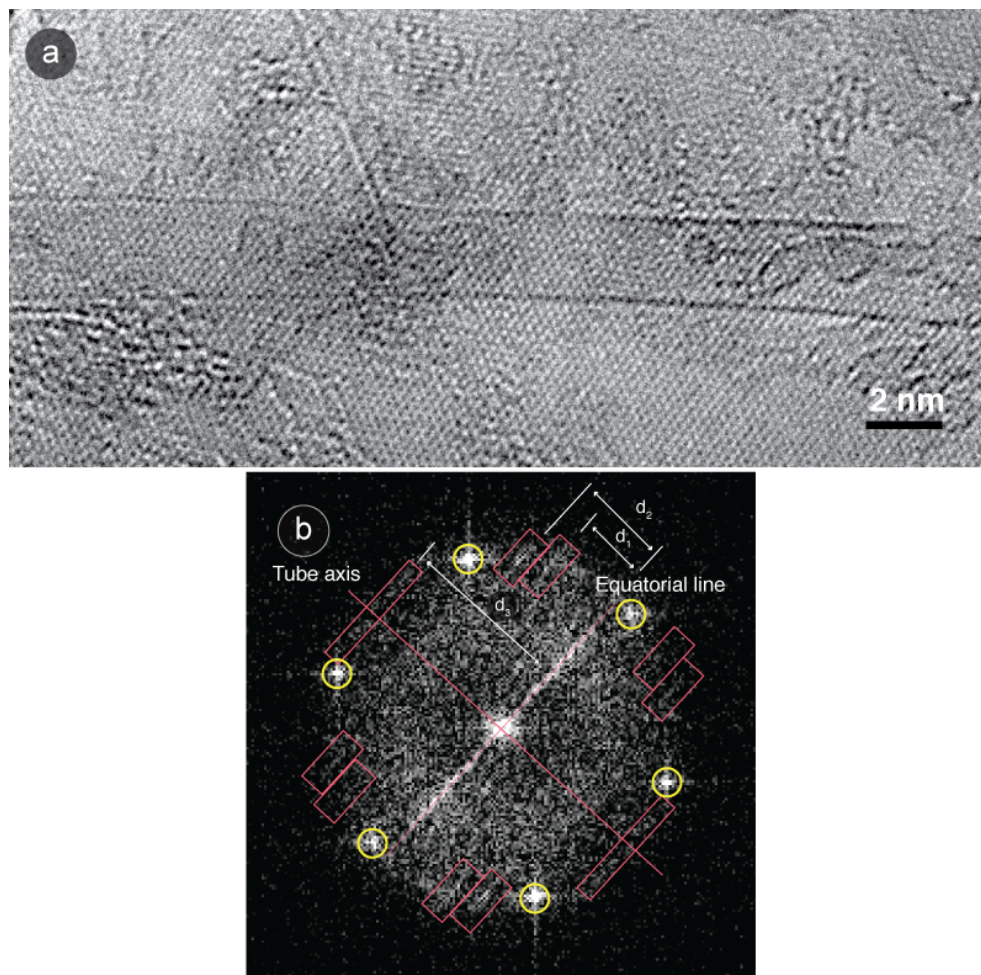


**Figure 5.12:** (a) HREM image of a chiral tube over graphite surface. (b) FFT, showing layer lines intensity (red rectangles) and honeycomb reflections (yellow circles).

affects the energy lost in friction. In the case of two contacting crystals, the commensurability between the two lattices makes the energy to depend on relative orientation.

SWCNTs and graphite share the same underlying structure: a honeycomb lattice of carbon atoms. The interaction between carbon nanotubes and the surface layer of graphite can be assumed to be reasonably similar to the one between graphite layers. Thus the coupling should be a weak van der Waals potential and the tubes should be relatively free to roll or slide over graphite surface almost friction-free.

The first experiments on the interaction between CNTs and graphite surface were done using atomic force microscopy at low-temperature which demonstrated

that carbon nanotubes can be easily manipulated over graphite layers. Researchers found that the lateral force applied to the cantilever to rotate in-plane a tube was not continuous, indeed it presented peaks at specific orientations of the tube. The CNT locked at minima of the interacting energy every  $60^\circ$  [85]. High-resolution STM imaging demonstrated atomic alignment between the lattices of the CNTs and graphite in these locking positions [86].

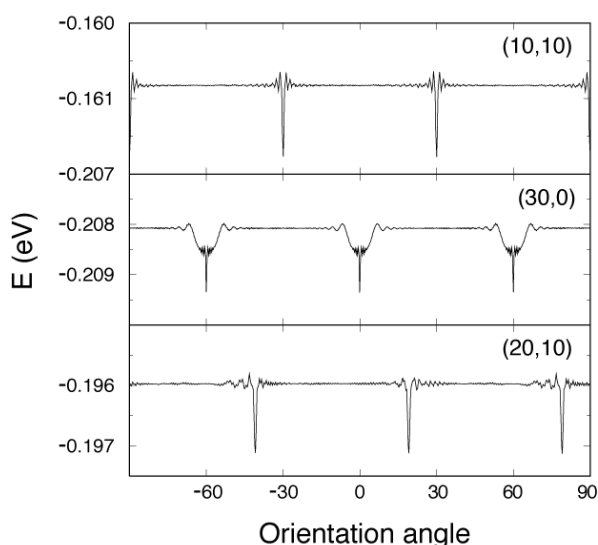


**Figure 5.13:** Interaction energy between SWCNTs and graphene, as a function of the orientation between tube axis and graphene lattice [Adapted from [87]].

These results confirmed simulations of the interaction energy between tubes and graphene performed few years before [87]. In figure 5.13, it is plotted the interaction energy between graphite surface and SWCNTs of three different chiral indexes. From the simulations each nanotube has specific equilibrium minima repeating every  $60^\circ$  reflecting the underlying symmetry of graphene lattice. The minima of the energy are very sharp, explaining the atomic-scale locking of the nanotube over graphene surface. Outside the equilibrium positions, the energy of different orientation is nearly flat, confirming the low friction expected out of locking positions.

In our experiment we did not observe specific equilibrium orientations for chiral tubes lying over FGC surface. Indeed we found the evidence for an effective removal of the chiral tubes from the surface of the flakes. Non chiral tubes were almost the only ones present over the dispersed flakes, with evidences for a more favorable grafting of zig-zag type tubes.

## Conclusions and outlooks

In this chapter we discussed the experimental details of the TEM investigation of the spontaneous alignment between SWCNTs and graphene lattice. The interest in this subject is motivated by the need to find a way to select SWCNTs of specific chirality. Since the electronic properties of these structures strongly depend on their structural orientation, understanding its interaction with the surfaces of various substrates is mandatory.

The experiments we performed demonstrated that a high degree of chiral selectivity is achievable using graphene as nanoscopic sieves for SWCNTs. SWCNTs of mixed chiral indexes were shortened and mixed to FGC membranes. Electron diffraction and HREM analysis showed that the sonication and successive centrifugation prevented the adhesion of the vast majority of chiral tubes to the surface of the graphite flakes. Remaining zig-zag and armchair tubes aligned to the underlying honeycomb lattice. The spontaneous atomic match between the two lattices was directly imaged using HREM.

We want to underline that this experiment investigated relative orientation of SWCNTs deposited over graphene, using TEM, for the first time. Previous investigations were performed using cryogenic AFM microscopy. The low temperature is mandatory to prevent the tip of the machine to drag the tubes while imaging. This poses a major limitation to these techniques as room temperature equilibrium investigation is impossible. TEM versatility results in the possibility to achieve an atomic level structural characterization at room temperature, preserving the structure of the observed sample.

This result opens up to the possibility to employ this spontaneous alignment and lock to successfully control the chirality of a SWCNTs mixture. Additional characterization is needed to evaluate the efficacy and ultimate yield of the process in removing chiral tubes. Further a controlled way to release the locked tube back in a suspension must be investigated for actual exploitation.



# **Conclusions**

Transmission electron microscopy is mandatory to obtain the structural properties which determine the remarkable electronic behavior of carbon nanostructures such as graphene and single-walled carbon nanotubes. We showed that the resolution of conventional TEM is not sufficient to image these structures with the required atomic detail, due to lens aberrations. Therefore, a key condition to achieve the goals of this research was the possibility of working with the facilities at the CNRS CEMES Toulouse laboratory, where a state-of-the-art aberrations-corrected TEM is available.

A first requirement to investigate carbon-based nanostructures is to lower the beam voltage (from standard 200 *kV* to 80 – 100 *kV*), in order to reduce radiation damage effects. To this purpose, a new calibration of the optical elements of the TEM was needed. The investigation of the structural and electronic properties which are the subject of this work, required the use of advanced techniques, like electron holography and Geometric Phase Analysis. Moreover, to investigate the 3D waviness of FGC flakes, a new 3D reconstruction methodology was developed.

The main results of this research can be summarized as follows.

- The mean electrostatic potential of an isolated SWCNT and that of a mono-atomically thin graphene crystal were successfully measured, by means of electron holography. The high accuracy achieved in the phase determination, made it possible to measure, for the first time, the valence-charge redistribution induced by the lattice curvature in an individual SWCNT.
- A novel methodology for the 3D reconstruction of the waviness of a 2D crystal membrane has been developed. Unlike other available TEM reconstruction techniques, like tomography, this new one requires processing of just a single HREM micrograph. The modulations of the inter-planar distances in the HREM image are measured using Geometric Phase Analysis, and used to recover the waviness of the crystal. The method was applied to the case of a folded FGC, and a height variation of 0.8 nm of the surface was successfully determined with nanometric lateral resolution.
- The adhesion of SWCNTs to the surface of graphene was studied, mixing shortened SWCNTs of different chiralities and FGC membranes. The spontaneous atomic match of the two lattices was directly imaged using HREM, and we found that graphene membranes act as tangential nano-sieves, preferentially grafting achiral tubes to their surface.

## BIBLIOGRAPHY

# Bibliography

- [1] Novoselov, K., Jiang, D., Schedin, F., Booth, T., Khotkevich, V., Morozov, S., and Geim, A. Two-dimensional atomic crystals. *P Natl Acad Sci Usa* **102**, 10451–10453 (2005).
- [2] Novoselov, K., Geim, A., Morozov, S., Jiang, D., Zhang, Y., Dubonos, S., Grigorieva, I., and Firsov, A. Electric field effect in atomically thin carbon films. *Science* **306**, 666–669 (2004).
- [3] L V Radushkevich, V. M. L. O strukture ugleroda, obrazujucesja pri termiceskom razlozenii okisi ugleroda na zeleznom kontakte. *Zurn Fistic Chim* **26**, 88–95 (1952).
- [4] Monthieux, M. and Kuznetsov, V. L. Who should be given the credit for the discovery of carbon nanotubes? *Carbon* **44**, 1621–1623 (2006).
- [5] Iijima, S. and Ichihashi, T. Single-shell carbon nanotubes of 1 nm diameter. *Nature* **363**, 603–605 (1993).
- [6] Geim, A. K. and Novoselov, K. S. The rise of graphene. *Nat. Mater.* **6**, 183–191 (2007).
- [7] Blake, P., Hill, E. W., Neto, A. H. C., Novoselov, K. S., Jiang, D., Yang, R., Booth, T. J., and Geim, A. K. Making graphene visible. *Appl Phys Lett* **91**, 063124 (2007).
- [8] Wallace, P. The band theory of graphite. *Phys Rev* **71**, 622–634 (1947).
- [9] McClure, J. Band structure of graphite and de haas-van alphen effect. *Physical Review* **108**, 612–618 (1957).
- [10] Slonczewski, J. and Weiss, P. Band structure of graphite. *Phys Rev* **109**, 272–279 (1958).

- [11] Zhang, Y., Tan, Y.-W., Stormer, H. L., and Kim, P. Experimental observation of the quantum hall effect and berry's phase in graphene. *Nature* **438**, 201–204 (2005).
- [12] Novoselov, K. S., Jiang, Z., Zhang, Y., Morozov, S. V., Stormer, H. L., Zeitler, U., Maan, J. C., Boebinger, G. S., Kim, P., and Geim, A. K. Room-temperature quantum hall effect in graphene. *Science* **315**, 1379–1379 (2007).
- [13] Naeemi, A. and Meindl, J. D. Electron transport modeling for junctions of zigzag and armchair graphene nanoribbons (gnrs). *Ieee Electr Device L* **29**, 497–499 (2008).
- [14] Meyer, J. C., Geim, A. K., Katsnelson, M. I., Novoselov, K. S., Booth, T. J., and Roth, S. The structure of suspended graphene sheets. *Nature* **446**, 60–63 (2007).
- [15] Fasolino, A., Los, J. H., and Katsnelson, M. I. Intrinsic ripples in graphene. *Nat Mater* **6**, 858–861 (2007).
- [16] Martin, J., Akerman, N., Ulbricht, G., Lohmann, T., Smet, J. H., Klitzing, K. V., and Yacoby, A. Observation of electron-hole puddles in graphene using a scanning single-electron transistor. *Nat Phys* **4**, 144–148 (2008).
- [17] de Juan, F., Cortijo, A., and Vozmediano, M. A. H. Charge inhomogeneities due to smooth ripples in graphene sheets. *Phys Rev B* **76**, 165409 (2007).
- [18] Guinea, F., Katsnelson, M. I., and Vozmediano, M. A. H. Midgap states and charge inhomogeneities in corrugated graphene. *Phys Rev B* **77**, 075422 (2008).
- [19] Iijima, S. Helical microtubules of graphitic carbon. *Nature* **354**, 56–58 (1991).
- [20] Kroto, H., Heath, J., O'Brien, S., RF Curl, R., and Smalley, R.  $c_{60}$  - buckminsterfullerene. *Nature* **318**, 162–163 (1985).
- [21] Mermin, N. Crystalline order in two dimensions. *Phys Rev* **176**, 250–254 (1968).
- [22] Neto, A., Guinea, F., and Peres, N. Drawing conclusions from graphene. *Phys World* (2006).
- [23] Frank, F. C. On miller-bravais indices and four-dimensional vectors. *Acta Crystallogr A* **18**, 866 (1964).

- [24] Landau, L. D. and Lifshits, E. M. *Statistical Physics Part I*, volume 5. Pergamon Press, Oxford, (1980).
- [25] Meyer, J., Geim, A., Katsnelson, M., Novoselov, K., Oberfell, D., Roth, S., Girit, C., and Zettl, A. On the roughness of single- and bi-layer graphene membranes. *Solid State Comm* **143**, 101–109 (2007).
- [26] Liu, Z., Suenaga, K., Harris, P. J. F., and Iijima, S. Open and closed edges of graphene layers. *Phys Rev Lett* **102**, 4 (2009).
- [27] Geim, A. K. and MacDonald, A. H. Graphene: Exploring carbon flatland. *Phys Today* **60**, 35–41 (2007).
- [28] Ashcroft, N. W. and Mermin, N. D. *Solid State Physics*. Holt, Rinehart, and Winston, New York, (1976).
- [29] Haldane, F. Model for a quantum hall effect without landau levels: Condensed-matter realization of the “parity anomaly”. *Phys Rev Lett* **61**, 2016–2018 (1988).
- [30] Novoselov, K. S., Mccann, E., Morozov, S. V., Falko, V. I., Katsnelson, M. I., Zeitler, U., Jiang, D., Schedin, F., and Geim, A. K. Unconventional quantum hall effect and berry’s phase of  $2\pi$  in bilayer graphene. *Nat Phys* **2**, 177–180 (2006).
- [31] Gusynin, V. and Sharapov, S. Magnetic oscillations in planar systems with the dirac-like spectrum of quasiparticle excitations. ii. transport properties. *Phys Rev B* **71**, 125124 (2005).
- [32] Novoselov, K. S., Geim, A. K., Morozov, S. V., Jiang, D., Katsnelson, M. I., Grigorieva, I. V., Dubonos, S. V., and Firsov, A. A. Two-dimensional gas of massless dirac fermions in graphene. *Nature* **438**, 197–200 (2005).
- [33] Novoselov, K. S., Morozov, S. V., Mohinddin, T. M. G., Ponomarenko, L. A., Elias, D. C., Yang, R., Barbolina, I. I., Blake, P., Booth, T. J., Jiang, D., Giesbers, J., Hill, E. W., and Geim, A. K. Electronic properties of graphene. *Phys Stat Sol B* **244**, 4106–4111 (2007).
- [34] Nakada, K., Fujita, M., Dresselhaus, G., and Dresselhaus, M. Edge state in graphene ribbons: Nanometer size effect and edge shape dependence. *Phys Rev B* **54**, 17954–17961 (1996).

- [35] Deheer, W., Berger, C., Wu, X., First, P., Conrad, E., Li, X., Li, T., Sprinkle, M., Hass, J., and Sadowski, M. Epitaxial graphene. *Solid State Comm* **143**, 92–100 (2007).
- [36] Geim, A. K. and Kim, P. Carbon wonderland. *Sci Am* **298**, 90–97 (2008).
- [37] Dikin, D. A., Stankovich, S., Zimney, E. J., Piner, R. D., Dommett, G. H. B., Evmenenko, G., Nguyen, S. T., and Ruoff, R. S. Preparation and characterization of graphene oxide paper. *Nature* **448**, 457–460 (2007).
- [38] Dresselhaus, M. and Dresselhaus, G. Intercalation compounds of graphite. *Adv Phys* **51**, 1–186 (2002).
- [39] Hernandez, Y., Nicolosi, V., Lotya, M., Blighe, F. M., Sun, Z., De, S., McGovern, I. T., Holland, B., Byrne, M., Gun'Ko, Y. K., Boland, J. J., Niraj, P., Duesberg, G., Krishnamurthy, S., Goodhue, R., Hutchison, J., Scardaci, V., Ferrari, A. C., and Coleman, J. N. High-yield production of graphene by liquid-phase exfoliation of graphite. *Nature nanotech* **3**, 563–568 (2008).
- [40] Vallés, C., Drummond, C., Saadaoui, H., Furtado, C., He, M., Roubeau, O., Ortolani, L., Monthieux, M., and Pénicaud, A. Solutions of negatively charged graphene sheets and ribbons. *Journal of the American Chemical Society* **130**, 15802–15804 (2008).
- [41] Saito, R. and Dresselhaus, G. *Physical Properties of Carbon Nanotubes*. Imperial College Press, (1998).
- [42] Tans, S., Verschueren, A., and Dekker, C. Room-temperature transistor based on a single carbon nanotube. *Nature* **393**, 49–52 (1998).
- [43] Yao, Z., Postma, H., Balents, L., and Dekker, C. Carbon nanotube intramolecular junctions. *Nature* **402**, 273–276 (1999).
- [44] Bachtold, A., Hadley, P., Nakanishi, T., and Dekker, C. Logic circuits with carbon nanotube transistors. *Science* **294**, 1317–1320 (2001).
- [45] Qin, L.-C. Electron diffraction from carbon nanotubes. *Rep Prog Phys* **69**, 2761–2821 (2006).
- [46] Heyd, R., Charlier, A., and McRae, E. Uniaxial-stress effects on the electronic properties of carbon nanotubes. *Phys Rev B* **55**, 6820–6824 (1997).

- [47] Yang, L., Anantram, M., Han, J., and Lu, J. Band-gap change of carbon nanotubes: Effect of small uniaxial and torsional strain. *Phys Rev B* **60**, 13874–13878 (1999).
- [48] Yang, L. and Han, J. Electronic structure of deformed carbon nanotubes. *Phys Rev Lett* **85**, 154–157 (2000).
- [49] Rubio, A., Corkill, J. L., and Cohen, M. L. Theory of graphitic boron-nitride nanotubes. *Phys Rev B* **49**, 5081–5084 (1994).
- [50] Chopra, N. G., Luyken, R. J., Cherrey, K., Crespi, V. H., Cohen, M. L., Louie, S. G., and Zettl, A. Boron-nitride nanotubes. *Science* **269**, 966–967 (1995).
- [51] Monthieux, M. and Flahaut, E. Meta- and hybrid-cnts: A clue for the future development of carbon nanotubes. *Mat. Sci. Eng. C* **27**, 1096–1101 (2007).
- [52] Derycke, V., Martel, R., Radosvljevic, M., Ross, F., and Avouris, P. Catalyst-free growth of ordered single-walled carbon nanotube networks. *Nano Lett.* **2**, 1043–1046 (2002).
- [53] Ishigami, M., Chen, J. H., Cullen, W. G., Fuhrer, M. S., and Williams, E. D. Atomic structure of graphene on sio<sub>2</sub>. *Nano Lett* **7**, 1643–1648 (2007).
- [54] DeGraef, M., editor. *Introduction to Conventional Transmission Electron Microscopy*. Cambridge University Press, Cambridge, (2003).
- [55] Williams, D. B. and Carter, C. B., editors. *Transmission Electron Microscopy: A Textbook for Materials Science*. Springer, Berlin, (1996).
- [56] Lucas, A., Bruyninckx, V., Lambin, P., and Bernaerts, D. Electron diffraction by carbon nanotubes. *Scanning Microsc* **12**, 415–436 (1998).
- [57] Meyer, J., Paillet, M., Duesberg, G., and Roth, S. Electron diffraction analysis of individual single-walled carbon nanotubes. *Ultramicroscopy* **106**, 176–190 (2006).
- [58] Hawkes, P. W. and Kasper, E., editors. *Principles of Electron Optics*. Academic Press, (1996).
- [59] Molhave, K., Gudnason, S. B., Pedersen, A. T., Clausen, C. H., Horsewell, A., and Boggild, P. Electron irradiation-induced destruction of carbon nanotubes in electron microscopes. *Ultramicroscopy* **108**, 52–57 (2007).

- [60] W, S. B., M, M., and E, L. D. Encapsulated c60 in carbon nanotubes. *Nature* **396**, 323–324 (1998).
- [61] Lichte, H. and Lehmann, M. Electron holography: basics and applications. *Rep Prog Phys* **71**, 016102 (2007).
- [62] Lichte, H., Formanek, P., Lenk, A., Linck, M., and Matzeck, C. Electron holography: Applications to materials questions. *Annu Rev Mater Res* **37**, 539–588 (2007).
- [63] Gabor, D. Microscopy by reconstructed wave-fronts. *P Roy Soc A-Math Phy* **197**, 454–487 (1949).
- [64] Merli, P. G., Missiroli, G. F., and Pozzi, G. Statistical aspect of electron interference phenomena. *Am J Phys* **44**, 306–307 (1976).
- [65] Volkl, E., Allard, L., and Joy, D., editors. *Introduction to electron holography*. Springer Verlag, New York, (1999).
- [66] Lehmann, M. and Lichte, H. Tutorial on off-axis electron holography. *Microsc Microanal* **8**, 447–466 (2002).
- [67] Matteucci, G., Missiroli, G., Nichelatti, E., Migliori, A., Vanzi, M., and Pozzi, G. Electron holography of long-range electric and magnetic fields. *J Appl Phys* **69**, 1835–1842 (1991).
- [68] O’Keeffe, M. and Spence, J. On the average coulomb potential ( $\sigma_0$ ) and constraints on the electron density in crystals. *Acta Crystallogr A* **50**, 33–45 (1994).
- [69] Lin, X. and Dravid, V. Mapping the potential of graphite nanotubes with electron holography. *Appl Phys Lett* **69**, 1014–1016 (1996).
- [70] Dumitrică, T., Landis, C., and Yakobson, B. Curvature-induced polarization in carbon nanoshells. *Chem Phys Lett* **360**, 182–188 (2002).
- [71] Kirkland, E. J. *Advanced Computing in Electron Microscopy*. Plenum Press, New York, (1998).
- [72] Katsnelson, M. I. and Geim, A. K. Electron scattering on microscopic corrugations in graphene. *Philos T R Soc Lon A* **366**, 195–204 (2008).

- [73] Midgley, P., Weyland, M., Yates, T., Tong, J., and Dunin-Borkowsky, R. Stem electron tomography for nanoscale materials science. *Microsc Microanal* **10**, 148–149 (2004).
- [74] Hytch, M., Snoeck, E., and Kilaas, R. Quantitative measurement of displacement and strain fields from hrem micrographs. *Ultramicroscopy* **74**, 131–146 (1998).
- [75] Hytch, M. and Plamann, T. Imaging conditions for reliable measurement of displacement and strain in high-resolution electron microscopy. *Ultramicroscopy* **87**, 199–212 (2001).
- [76] Bunch, J. S., Verbridge, S. S., Alden, J. S., van der Zande, A. M., Parpia, J. M., Craighead, H. G., and McEuen, P. L. Impermeable atomic membranes from graphene sheets. *Nano Lett* **8**(8), 2458–2462 (2008).
- [77] Hytch, M. Analysis of variations in structure from high resolution electron microscope images by combining real space and fourier space information. *Microsc Microanal M* **8**, 41–57 (1997).
- [78] Snoeck, E., Warot, B., Arduin, H., Rocher, A., Casanove, M., Kilaas, R., and Hytch, M. Quantitative analysis of strain field in thin films from hrtem micrographs. *Thin Solid Films* **319**, 157–162 (1998).
- [79] Hytch, M. and Stobbs, W. Quantitative criteria for the matching of simulations with experimental hrem images. *Microsc Microanal M* **5**, 133–151 (1994).
- [80] Li, L., Reich, S., and Robertson, J. Modelling the nucleation and chirality selection of carbon nanotubes. *J Nanosci Nanotech* **6**, 1290–1297 (2006).
- [81] Lolli, G., Zhang, L., Balzano, L., Sakulchaicharoen, N., Tan, Y., and Resasco, D. Tailoring (n,m) structure of single-walled carbon nanotubes by modifying reaction conditions and the nature of the support of como catalysts. *J Phys Chem B* **110**, 2108–2115 (2006).
- [82] Chen, Y., Wei, L., Wang, B., Lim, S., Ciuparu, D., Zheng, M., Chen, J., Zoican, C., Yang, Y., Haller, G. L., and Pfefferle, L. D. Low-defect, purified, narrowly (n, m)-dispersed single-walled carbon nanotubes grown from cobalt-incorporated mcm-41. *Acs Nano* **1**, 327–336 (2007).
- [83] Sato, Y., Yanagi, K., Miyata, Y., Suenaga, K., Kataura, H., and Lijima, S. Chiral-angle distribution for separated single-walled carbon nanotubes. *Nano Lett* **8**, 3151–3154 (2008).

- [84] Ju, S.-Y., Doll, J., Sharma, I., and Papadimitrakopoulos, F. Selection of carbon nanotubes with specific chiralities using helical assemblies of flavin mononucleotide. *Nature Nanotech* **3**, 356–362 (2008).
- [85] Yanagi, H., Sawada, E., Manivannan, A., and Nagahara, L. Self-orientation of short single-walled carbon nanotubes deposited on graphite. *Appl Phys Lett* **78**, 1355–1357 (2001).
- [86] Rettig, C., Bodecker, M., and Hovel, H. Carbon-nanotubes on graphite: alignment of lattice structure. *J Phys D Appl Phys* **36**, 818–822 (2003).
- [87] Buldum, A. and Lu, J. Atomic scale sliding and rolling of carbon nanotubes. *Phys Rev Lett* **83**, 5050–5053 (1999).

## List of publications

### Peer-reviewed journal

1. Cristina Vallés, Carlos Drummond, Hassan Saadaoui, Clascidia A. Furtado, Maoshuai He, Olivier Roubeau, Luca Ortolani, Marc Monthieux & Alain Pénicaud, Solutions of Negatively Charged Graphene Sheets and Ribbons, *J. Am. Chem. Soc.* **130**, 15802-15804 (2008)
2. V.D. Cammilleri, V. Yam, F. Fossard, C. Renard, D. Bouchier, P.F. Fazzini, L. Ortolani, F. Houdellier & M. Hÿtch, Lateral epitaxial growth of germanium on silicon oxide, *Appl. Phys. Lett.* **93**, 043110 (2008).
3. L. Ortolani, E. Comini, P.F. Fazzini, M. Ferroni, V. Guidi, P.G. Merli, V. Morandi, G. Pozzi, G. Sberveglieri & A. Vomiero, Electrical and holographic characterization of gold catalyzed titania-based layers, *J. Eur. Ceram. Soc.* **27**, 4131-4134 (2007).
4. P.F. Fazzini, L. Ortolani, G. Pozzi & Filippo Ubaldi, Interference electron microscopy of one-dimensional electron-optical phase objects, *Ultramicroscopy* **106**, 620-629 (2006).

### Conference proceedings

1. L. Ortolani, F. Houdellier, M. Monthieux & V. Morandi, *3D reconstruction at the nanoscale: mapping graphene waviness*, **oral** at MRS Spring Meeting 2009, San Francisco (CA), USA, 13-17 April 2009.
2. L. Ortolani, F. Houdellier, M. Monthieux & V. Morandi, *3D reconstruction of graphene waviness*, **poster** at Carbon 2009, Biarritz, France, 14-19 June 2009.
3. L. Ortolani, M. Monthieux & V. Morandi, *Graphene as nanoscopic tangential sieve for selecting achiral SWCNTs*, **oral** at Carbon 2009, Biarritz, France, 14-19 June 2009.
4. L. Ortolani, F. Houdellier & M. Monthieux, *Discrete Atom Imaging in Carbon Nanotubes and Peapods Using Cs-Corrected TEM Operated at 100 keV*, **poster** at 14th European Microscopy Congress, Aachen, Germany, 1-5 September 2008.

5. L. Ortolani, P.F. Fazzini, V. Morandi & M. Ferroni, *Surface phase effect in gold nanoparticles investigated by transmission electron holography*, **poster** at 14th European Microscopy Congress, Aachen, Germany, 1-5 September 2008.
6. Ferroni M., Baratto C., Comini E., Faglia G., Ortolani L., Merli P. G., Morandi V., S. Todros, Vomiero A. & Sberveglieri G., *Nanowires of semiconducting metal-oxides and their functional properties*, **poster** at 14th European Microscopy Congress, Aachen, Germany, 1-5 September 2008.
7. L. Ortolani, P. F. Fazzini & M. Ferroni, *A new set of software tools for holographic reconstruction and analysis with fast automatic phase unwrapping*, **oral** at 8th Multinational Congress on Microscopy, Prague, Czech Republic, 17-21 June, 2007.
8. L. Ortolani, E. Comini, P. F. Fazzini, M. Ferroni, V. Guidi, P. G. Merli, V. Morandi, G. Pozzi & G. Sberveglieri, *Electrical and holographic characterization of gold catalyzed titania based layers*, *oral* at *Electroceramics X*, Toledo, Spain, 18-22 June 2006.
9. P.F. Fazzini, L. Ortolani & G. Pozzi, *Characterization of the Catalytic Behavior of Gold Nano-particles with Electron Holography*, **poster** at 16th International Microscopy Congress, Sapporo, Japan, 3-8 September 2006

## Acknowledgments

My acknowledgments are dedicated to all the people that contributed directly or indirectly to it. Above all, I must express my gratitude to Dr. Pier Giorgio Merli and Dr. Vittorio Morandi, as they have been my guidance and reference during all these years, and this work could not be possible without their continuous support. Pier Giorgio's sudden loss left an immense void, and I thank Dr. Giorgio Lulli for accepting to drive me to the end of this project. His advices and the fruitful discussions were really important. I thank Prof. Giulio Pozzi for introducing me to the fabulous world of electron interferometry, and for leading the beginning of my Ph.D. I am grateful to Prof. Giuseppe Morandi, who granted me the honour of being his last Ph.D. student! I am in debt to all the people of the IMM Bologna, for their teachings, their help, and the lively and cheerful working environment.

This work is the result of a wonderful journey to CEMES laboratory in Toulouse. I am indebted to Dr. Marc Monthieux, who received me in his group and he taught me a lot about the french way to honeycomb lattices. I want to thank him also for introducing me to Alain Pénicaud and all its group, that produced most of the graphene flakes used in the experiments. In France, my skills as a microscopist were forged by the hard teachings of Florent Houdellier and, really, all the beautiful images shown here would not be possible without its continuous support. I also want to thank Etienne Snoeck for the precious help in the holographic experiments over graphene and Martin Hÿtch for the fruitful discussion over GPA and 3D reconstruction. I really miss my *freaky family*. Teresa, Eeva, Pier Francesco, Nuria, all of you made my stay in Toulouse an unforgettable experience.

The most beautiful gift from France was Caterina. Her critical reading of the early versions of this manuscript were really helpful. Moreover, she resisted during all this hectic and stressing period, and she continuously encouraged and motivated me, even from a thousand kilometers.

Last, but not least, I want to thank mom and dad, because they are always there, ready to encourage and help me.